



Universitetet  
i Stavanger

**Faculty of Science and Technology**

## MASTER'S THESIS

Study program/Specialization: Petroleum Geosciences Engineering	Spring semester, 2019 Confidential (5 years)
Writer: Tien Hoang Nguyen	<hr/> (Writer's signature)
Faculty supervisor: Nestor Cardozo, University of Stavanger  External supervisor(s): Lothar Schulte, Schlumberger SIS	
Title of thesis:  Applying Geological Process Modeling to a turbidite system in the northern North Sea	
Credits (ECTS): 30	
Keywords: Turbidite system, Geological Process Modeling, Stratigraphy Forward Modeling, Northern North Sea	Pages: 85  Stavanger, 15 <sup>th</sup> June, 2019

Copyright  
by  
Tien Hoang Nguyen  
2019

**Applying Geological Process Modeling to a turbidite system in the  
northern North Sea**

**by**

**Tien Hoang Nguyen**

**Master thesis**

Presented to the Faculty of Science and Technology

The University of Stavanger

**The University of Stavanger**

**June 2019**

## **Acknowledgements**

This Master thesis is a cooperation between the University of Stavanger, SIS Schlumberger, and Neptune Energy AS.

Firstly, I would like to thank my parents for their love and continuous support. They are the motivation that keeps me trying everyday to overcome all challenges.

I want to express my gratitude to my supervisors, Lothar Schulte at SIS Schlumberger Norway and Nestor Cardozo at UiS. They gave me not only the chance to work with this interesting topic but also excellent guidance and encouraging feedback, which helped me to accomplish the Master thesis.

In addition, I am grateful to Neptune Energy AS for providing the dataset and sharing critical information that were used in this study. I also would like to thank Schlumberger, especially Per Salomonsen and Jan Tveiten, for providing me the software and giving me tremendous technical support.

Finally, I would like to appreciate my classmates, friends, and professors for their amity and assistance during the two great years that we have shared together at the University of Stavanger.

## **Abstract**

### **Applying Geological Process Modeling to a turbidite system in the northern North Sea**

Tien Hoang Nguyen  
The University of Stavanger, 2019

Supervisors: Nestor Cardozo and Lothar Schulte

In recent years, several mathematical methods, especially those based on geostatistics, have been used in reservoir characterization. The reliability of the static models derived from these techniques depends on available seismic data, well interpretation, and outcrop analogues. Although geostatistical methods have been efficiently applied in many cases, they have limitations in integrating the data of various disciplines into a consistent depositional model.

A relative new approach, named geological process modeling (GPM), or stratigraphic forward modeling (SFM) can help geologists to verify their concepts and build reliable geological models. This technique, which involves the time-reconstruction of geological configurations, applies numerical simulation to reflect the interaction between several physical processes including erosion, sediment transport and deposition, wave action, tectonic movement, compaction, and carbonate growth (Tetzlaff and Harbaugh, 1989). In this thesis, a turbidite reservoir will be analyzed and regenerated with GPM.

The study case is an Early Cretaceous turbiditic reservoir on the Måløy Slope, northern North Sea. No scientific work has been published for the data set provided for this thesis. This study tests different conceptual depositional models thru making use of the predictive power of GPM. The final model that is selected for reservoir modelling is based on parameter values lying within the range of published analogue data and is supported by the measured data of the study field.

## Table of Contents

<b>List of Tables</b> .....	viii
<b>List of Figures</b> .....	ix
1. Introduction .....	1
1.1 Objectives .....	1
1.2 Study area .....	2
2. Geological setting .....	2
2.1 Regional geology and structural evolution.....	2
2.2 Måløy slope .....	3
2.3 Cretaceous in the Northern North Sea.....	4
2.4 The Study Area.....	8
3. Theory.....	9
3.1 Sedimentology background .....	9
3.1.1 Deep-marine processes .....	10
3.1.2 Hybrid sediment gravity flow deposits .....	12
3.2 Stratigraphy Forward Modeling .....	14
3.2.1 Diffusion .....	14
3.2.2 Free surface flow modeling .....	15
3.2.3 Particle-based numerical methods .....	16
3.2.4 Sediment transport modeling .....	17
4. Data.....	19
5. Previous work .....	19
5.1 Seismic spectral decomposition.....	19
5.2 Structural reconstruction.....	20
5.3 Biostratigraphic framework.....	22
5.4 Chlorite provenance study .....	22
5.5 Sedimentology analysis .....	22
5.6 Conceptual model.....	28

6.	Methodology.....	30
6.1	Quality check of the input data.....	30
6.2	Testing numerical parameters.....	31
6.3	Setting up of the final model .....	34
6.3.1	Investigation of the influence of the base maps.....	35
6.3.2	Investigation of the influence of the interaction between 2 canyons...35	
6.4	Calibration of the final model.....	40
6.4.1	Calibrating the influence of the base maps .....	41
6.4.2	Calibration of the influence of the interaction between 2 canyons.....	41
7.	Observation.....	44
7.1	GPM output .....	44
7.1.1	Influence of the base maps on the turbidite geometry .....	44
7.1.2	Investigating the influence of the interaction between the 2 canyons .46	
7.2	Reservoir properties.....	53
7.2.1	Sections at well B and along the basin axis .....	53
7.2.2	Quantitative comparison between the model and well data.....	58
8.	Discussion.....	61
8.1	System evolution .....	62
8.2	Geometry distribution.....	62
8.3	Reservoir architecture.....	64
9.	Conclusion.....	66
	<b>Appendix.....</b>	<b>68</b>
	<b>Reference .....</b>	<b>70</b>

## List of Tables

<b>Table 1.</b> Criteria characterizing high-density turbidity currents and low-density turbidity currents (Shanmugam, 1996). .....	12
<b>Table 2.</b> Reconstructed seismic horizons used for analyzing and modeling the turbidite. ....	21
<b>Table 3.</b> Summary of chlorite provenance from a Neptune Energy study in the lower and upper reservoir .....	22
<b>Table 4.</b> Facies Associations summary by (Neptune Energy internal report).....	24
<b>Table 5.</b> Core images of facies associations at well B (Neptune Energy internal report) .....	25
<b>Table 6.</b> Spatial and temporal parameters of the numerical models. ....	31
<b>Table 7.</b> Values for numerical parameters controlling the unsteady flow .....	32
<b>Table 8.</b> The geological parameters that control each criteria .....	34
<b>Table 9.</b> Three main cases to investigate the impact of two sources coming from two different canyons.....	36
<b>Table 10.</b> Input parameters of clastic sediments. ....	36
<b>Table 11.</b> The water velocity and sediment accumulation rate at two sources related to the two canyons.....	37
<b>Table 12.</b> Cutoff values of sediment fractions for each facies in Case 1 and 3. ....	42
<b>Table 13.</b> Cutoff values of sediment fractions for each facies in Case 2. ....	42
<b>Table 14.</b> Vshale cutoff values for all sediment types. ....	43
<b>Table 15.</b> The Net-to-Gross cutoff values for all sediment types. ....	43
<b>Table 16.</b> Base maps selection criteria .....	46
<b>Table 17.</b> Matching level of facies models to the actual facies log in the three modelled cases .....	58
<b>Table 18.</b> Matching level of Vshale properties and well log in three cases.....	60
<b>Table 19.</b> Summary of qualitative criteria to choose the best case for investigating the canyons' interaction.....	61



## List of Figures

<b>Figure 1.</b> Simplified map of the main structural elements of the northern North Sea, edited after Færseth et al. (1997), and simplified map of the study area (Reeve et al., 2015). .....	2
<b>Figure 2.</b> Simplified regional cross-section A-A' (see figure 1) showing the generalised structure of the Viking Graben, Sogn Graben and Måløy Slope (Reeve et al., 2015)...3	3
<b>Figure 3.</b> Stratigraphic and sub-regional structural setting of the study area. (A) Simplified stratigraphic column through the study area;( B) Seismic section B-B', as shown in Figure 1 (Jackson et al., 2008). .....	4
<b>Figure 4.</b> Stratigraphy column of the Cretaceous in the northern North Sea (van Buchem et al., 2018). .....	5
<b>Figure 5.</b> Inferred sea level variation in Early Cretaceous (Haq, 2014). .....	8
<b>Figure 6.</b> The deep-water environment (Shanmugam, 2000). .....	9
<b>Figure 7.</b> Schematic diagram showing the deep-marine sedimentary environment with the different processes and their deposits. Water depth is > 200 m (shelf-slope break) (Shanmugam, 2018).....	10
<b>Figure 8.</b> Schematic diagram of four common types of gravity-driven downslope processes that transport sediments into the deep-marine environments, edited after (Shanmugam, 2018).....	11
<b>Figure 9.</b> Illustration of contrasting downstream evolution involving: (a) progressive dilution of a turbidity current and (b) transformation of a turbidity current to a hybrid flow. Edited after (Haughton et al., 2003, Haughton et al., 2009).....	13
<b>Figure 10.</b> Dependency of the sediment diffusion coefficient ( $k_d$ ) on the grain size used by the GPM model (Tetzlaff et al., 2007). .....	15
<b>Figure 11.</b> Diagram displaying the threshold of sediment movement based on the Shields' criterion (Tetzlaff et al., 2007, Shields, 1936). .....	17
<b>Figure 12.</b> Time slices of seismic spectral decomposition at different intervals within the reservoir: (A) Within the lower reservoir, (B) Base of the upper reservoir, (C) Within the upper reservoir (images from Neptune Energy). .....	19

<b>Figure 13.</b> Top Åsgard paleo-topographic map from the structural reconstruction of the area. This map was used as the initial base map of the turbidite model (image from Neptune Energy). .....	20
<b>Figure 14.</b> Dip angle attribute map of the Åsgard paleo-topography map (image from Neptune Energy). .....	21
<b>Figure 15.</b> Facies interpretation of well B (edited after (Clerc et al., 2018)). .....	23
<b>Figure 16.</b> Synthetic sequence of well B (from Neptune Energy). .....	27
<b>Figure 17.</b> Synthetic facies association distribution along the depositional fairway along wells A and B (from Neptune Energy). .....	27
<b>Figure 18.</b> Synthetic facies association distribution along the depositional fairway across well B (from Neptune Energy). .....	28
<b>Figure 19.</b> Reservoir thickness attribute displayed in the Åsgard paleo-topography map (Neptune Energy). .....	28
<b>Figure 20.</b> A 3D view of the conceptual model (Neptune Energy). .....	29
<b>Figure 21.</b> The workflow that was applied to deliver the possible outcomes from the input data. ....	30
<b>Figure 22.</b> Workflow to verify the general numerical parameters in the GPM model. ....	32
<b>Figure 23.</b> Spike cells as artifacts from the simulation. ....	33
<b>Figure 24.</b> The two base maps used to investigate the influence of the base map topography: (A) Base map 1 with high smoothness and low confinement, (B) Base map 2 with low smoothness and high confinement. ....	35
<b>Figure 25.</b> The variation of water velocity at canyon 1 (A) and canyon 3 (B) (case 1) .....	38
<b>Figure 26.</b> The variation of sediment rate modifier at canyon 1 (A) and canyon 3 (B) (case 1) .....	39
<b>Figure 27.</b> 2D view of the topography map with the navigation of several cross sections, which were used to control the outcome of the model. ....	40
<b>Figure 28.</b> Workflow to calibrate and adjust the geological parameters for each case to investigate the influence of canyons interaction. ....	41

**Figure 29.** Cross section A-A' at well B showing lithology mixture properties of two models using two base maps: (A) the result of the more opened base map 1 (figure 24A); (B) the result of the more confined base map 2 (figure 24B). Navigation of cross section A-A' displayed in figure 27.....44

**Figure 30.** Cross section A-A' at well B showing conglomerate fraction properties of two models using two base maps: (A) the result of the more opened base map 1 (figure 24A); (B) the result of the more confined base map 2 (figure 24B). Navigation of cross section A-A' displayed in figure 27.....45

**Figure 31.** The result of case 1 shown in the section crossing well B (line A-A' in Figure 27) with three properties: (A) the lithological mixture, (B) the proportion of conglomerate coming from canyon 1, (C) the proportion of conglomerate coming from canyon 3.....46

**Figure 32.** The result of case 1 shown in the section along the basin axis (line B-B' in Figure 27) with three properties: (A) the lithological mixture, (B) the proportion of conglomerate coming from canyon 1, (C) the proportion of conglomerate coming from canyon 3.....47

**Figure 33.** 3D view of lithology distribution of case 1: (A) the top of the lower reservoir, (B) the top of the upper reservoir .....48

**Figure 34.** The result of case 2 in the cross section at well B (A-A') with three properties: (A) the lithological mixture, (B) the proportion of conglomerate coming from canyon 1, (C) the proportion of conglomerate coming from canyon 3.....49

**Figure 35.** Result of case 2 in the cross section B-B' along the basin axis location with three properties: (A) the lithological mixture, (B) the proportion of conglomerate coming from canyon 1, (C) the proportion of conglomerate coming from canyon 3. Navigation of cross section B-B' displayed in figure 27.....50

**Figure 36.** 3D view of lithology distribution of case 2: (A) the top of lower reservoir, (B) the top of upper reservoir.....50

**Figure 37.** Result of case 3 in the cross section A-A' at well B location with three properties: (A) the lithological mixture, (B) the proportion of conglomerate coming from canyon 1, (C) the proportion of conglomerate coming from canyon 3. Navigation of cross section A-A' displayed in figure 27. ....51

**Figure 38.** The result of case 3 in the cross section along the basin axis (B-B') with three properties: (A) the lithological mixture, (B) the proportion of conglomerate coming from canyon 1, (C) the proportion of conglomerate coming from canyon 3..52

**Figure 39.** 3D view of lithology distribution of case 3: (A) the top of lower reservoir, (B) the top of upper reservoir.....52

**Figure 40.** The cross section at well B (A-A') showing the result of case 1: (A) the facies, (B) the Net-to-Gross, (C) the Vshale properties.....53

**Figure 41.** The section along the basin axis (B-B') showing the result of case 1: (A) the facies, (B) the Net-to-Gross, (C) the Vshale properties.....54

**Figure 42.** The cross section at well B (A-A') showing the result of case 2: (A) the facies, (B) the Net-to-Gross, (C) the Vshale properties.....55

**Figure 43.** The section along the basin axis (B-B') showing the result of case 2: (A) the facies, (B) the Net-to-Gross, (C) the Vshale properties.....56

**Figure 44.** The cross section at well B (A-A') showing the result of case 3: (A) the facies, (B) the Net-to-Gross, (C) the Vshale properties.....57

**Figure 45.** The section along the basin axis (B-B') showing the result of case 3: (A) the facies, (B) the Net-to-Gross, (C) the Vshale properties.....58

**Figure 46.** Three curves including the actual facies log (left), the facies log converted from the model (middle), and Boolean log (right) for each of the three simulated cases. ....59

**Figure 47.** Three curves including the actual Vshale log (left), the Vshale log converted from the model (middle), and the Boolean log (right) for each of the three simulated cases .....60

**Figure 48.** The thickness attribute of the reservoir units of case 1: (A) the thickness of the lower reservoir, (B) the thickness of the upper reservoir. The green polygon represents the reservoir boundary derived from seismic .....63

**Figure 49.** The facies map at different reservoir intervals: (A) the facies map at the top of the lower reservoir; (B) the facies map at the top of the upper reservoir. The green polygon represent the reservoir boundary derived from seismic.....64

**Figure 50.** Cross section C-C' at the canyon feet of case 1. Navigation of cross section C-C' displayed in figure 27.....64

**Figure 51.** Cross section D-D' thru the most distal area of the reservoir of case 1. Navigation of cross section D-D' displayed in figure 27. ....65

**Figure 52.** Section E-E' along the eastern flank with reservoir properties: (A) the facies property; (B) the Net-to-Gross property. Navigation of cross section E-E' displayed in figure 27. ....65

**Figure 53.** Section F-F' along the western flank with reservoir properties: (A) the facies property; (B) the Net-to-Gross property. Navigation of cross section F-F' displayed in figure 27. ....66

**Figure 54.** The variation of water velocity at canyon 1 (A) and canyon 3 (B) (Case 2). ....68

**Figure 55.** The variation of sediment rate modifier at canyon 1 (A) and canyon 3 (B) (Case 2). ....68

**Figure 56.** The variation of water velocity and sediment rate modifier at two canyons (Case 3). ....69

## **1. Introduction**

“Geological Process Modeling” (GPM) or “Stratigraphic Forward Modeling” (SFM) refers to a principle which quantifies and simulates the physical and biological processes, including sedimentation, compaction, and structural deformation, acting over geological times to reproduce the present-day geologic configurations (Burgess, 2012, Paola, 2000). This is a more rigorous approach than geostatistical methods, as algorithms based on physical laws are applied to generate a depositional system. In short, GPM provides geoscientists with a powerful tool to check the internal consistency of their geological model, observe the influence of factors above on the overall result, and verify the viability of different geological scenarios.

Turbidite systems or submarine fans are prolific clastic reservoirs in the deep marine environment. Due to the influence of both global and local factors on these deposits, the complexity of physical processes and interactions, as well as the varying scale, different classifications have been proposed, leading to different approaches for modelling (Shanmugam, 2000). Sandbox experiments have been the most common method for turbidite modelling. However, one major limitation of sandbox experiment is the scale. Because the models are miniaturized from the real system, they cannot capture the actual thickness or lithology distribution. Also, the grains’ sizes used in the sandbox experiment cannot be scaled up to the size of the real case and the span time of a turbidite complex in the sandbox experiment is much shorter than the true case (Lai et al., 2016).

With its properties, GPM is the ideal solution to address these problems. Based on physical laws, GPM retains the true behavior of a sandbox experiment. In addition, by applying numerical simulation, GPM does not have the time and space constraints of scaled physical models (Tetzlaff and Priddy, 2001). However, the information needed to build a complete GPM model is large to ensure a robust fit to the geological constraints. For these reasons, no case in the Northern North Sea describing the application of GPM to a turbidite system has yet been published.

### **1.1 Objectives**

This thesis analyzes a turbidite reservoir in the Måløy Slope, northern North Sea to understand the controlling factors and geological evolution of the system by implementing a stratigraphic forward modelling approach. In addition to enhance reservoir characterization and better assess uncertainties, this thesis can be a useful example of the application of GPM to similar situations.

The main objective of the thesis is to investigate the geometry, lithology and internal architecture of the reservoir. This goal is subdivided into smaller tasks: (1) investigate the influence of controlling factors including: paleo-bathymetry, sediment sources, diffusion coefficient, and flow velocity; (2) determine the reservoir architectures and properties; (3) identify alternative scenarios which can lead to similar lithology properties; (4) discuss the outcomes within the regional geological knowledge of the area.

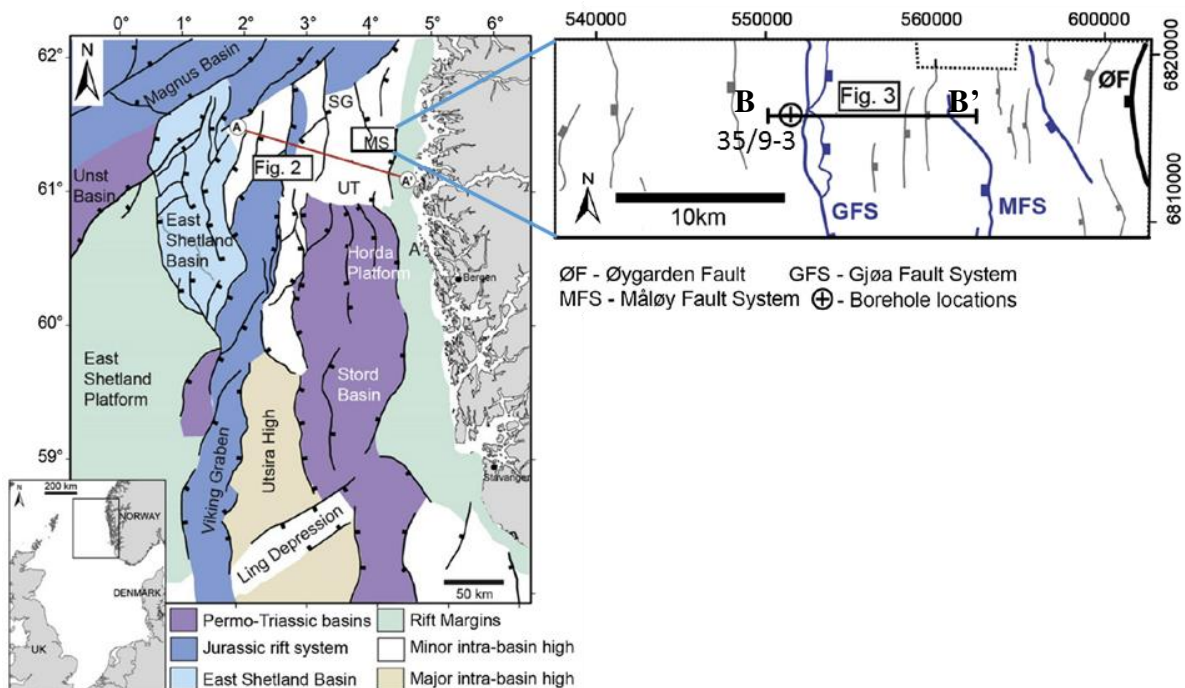
## 1.2 Study area

The study area is a new discovery located in the Måløy Slope, northern North Sea. The field has a reservoir containing oil and gas in good quality sandstone of Early Cretaceous age (Albian) associated to the Agat Formation. The sandstones are interpreted as the result of turbidite systems.

## 2. Geological setting

### 2.1 Regional geology and structural evolution

The North Sea has four main basins: Northern, Moray Firth, Central, and Southern Basin. Each basin has a different structural and stratigraphic development corresponding to a unique geologic history acting over 400 My. Considering the Northern North Sea, the paleo-rift system containing the Viking and Sogn Graben has approximately 150–200 km width of extended



**Figure 1.** Simplified map of the main structural elements of the northern North Sea, edited after Færseth et al. (1997), and simplified map of the study area (Reeve et al., 2015).

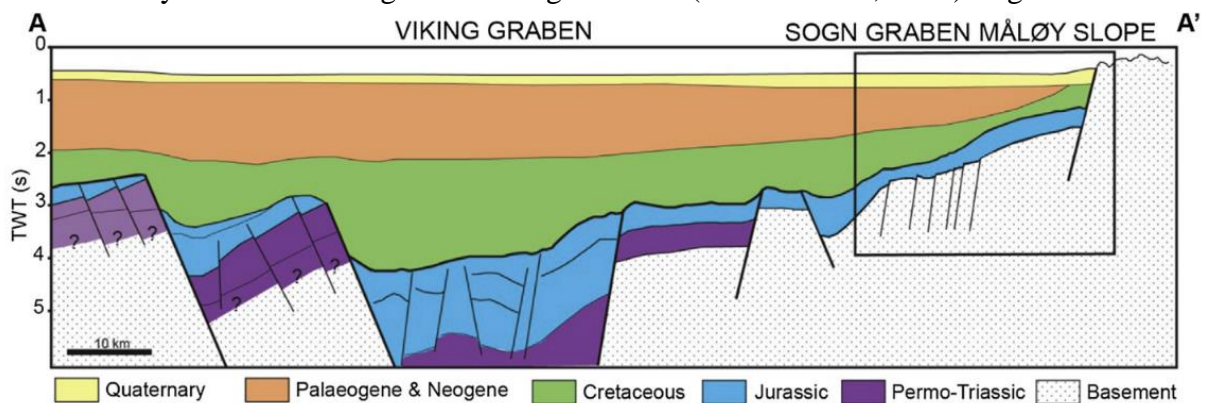
upper crust with pre-Triassic to Tertiary strata. It is bounded by the Norwegian coast to the East and by the Shetland Platform to the West (Nottvedt et al., 1995) (Figure 1).

The geological evolution of the North Sea consists of eight major events (Glennie, 2009):

1. Precambrian events – formation of highlands and basement elements.
2. The Caledonian plate cycle – corresponding to the Athollian and Caledonian orogenies.
3. The Variscan plate cycle – resulted in the Devonian-Carboniferous rifting, Variscan orogeny, and formation of the Pangaea supercontinent.
4. Permo-Triassic rifting and thermal subsidence – Late Permian subsidence of the Moray Firth and East-West trending Permian Basin.
5. Middle Jurassic domal uplift – development of transient mantle plume head leading to erosion of central North Sea, volcanism, and subsequent rift system.
6. Late Jurassic to earliest Cretaceous extension – which led to fault-block rotations and formation of major structural traps within and adjacent to the Viking and Central Grabens.
7. Development of the Iceland hot spot and North Atlantic rifting – created the regional tilt, especially in the Inner Moray Firth.
8. Tectonic Inversion of Mesozoic basin – the intraplate compression was induced by creation of the Atlantic Ocean which led to the tectonic inversion of sedimentary basins across north-west Europe.

## 2.2 Måløy slope

The Måløy slope is located in the eastern margin of the northern North Sea Basin (Figure 1). At present, this slope is bounded to the east by the west-dipping Øygarden Fault Complex, and to the west by the eastern margin of the Sogn Graben (Jackson et al., 2008). Figure 2 shows a

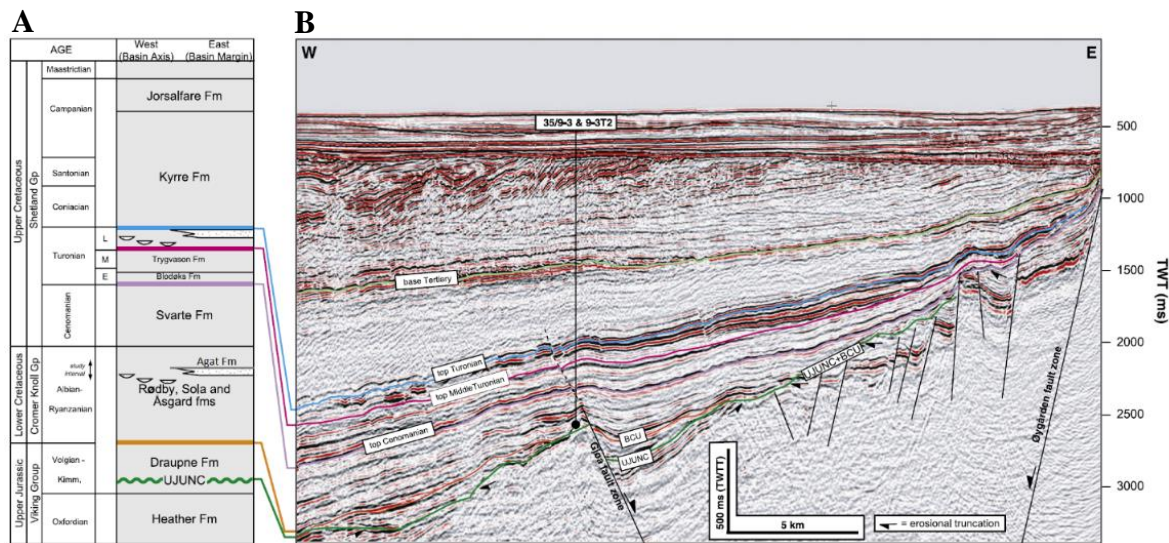


**Figure 2.** Simplified regional cross-section A-A' (see figure 1) showing the generalised structure of the Viking Graben, Sogn Graben and Måløy Slope (Reeve et al., 2015).



simplified structural cross section of the Northern North Sea area, and Figure 3B shows a seismic section across the Måløy slope structure.

A discontinuous BCU and westward thickening of the Jurassic sequence indicates tectonic activity from Late Jurassic to Early Cretaceous. During this period, a system of N–S or NNW–SSE normal faults and several half-grabens formed (Jackson et al., 2008). These structures compartmentalize the Måløy Slope.



**Figure 3.** Stratigraphic and sub-regional structural setting of the study area. (A) Simplified stratigraphic column through the study area; (B) Seismic section B-B', as shown in Figure 1 (Jackson et al., 2008).

### 2.3 Cretaceous in the Northern North Sea

The main Cretaceous formations are shown in the stratigraphic column of Figure 4. The depositional history of the Northern North Sea during the Cretaceous was influenced by the structural relief formed during the previous Late Jurassic rifting. In the early and middle Ryazanian, a combination of remnant relief and regional basin trends created a depositional environment characterized by structurally controlled, restricted basins with anoxic conditions, resulting in the deposition of the organic-rich Draupne Formation shale. During the late Ryazanian, the basin became less isolated and more oxygenated, with the corresponding deposition of the “Base Cretaceous” reflector (Bugge et al., 2001). In the following paragraphs, the Cretaceous formations in the study area are discussed in detail.

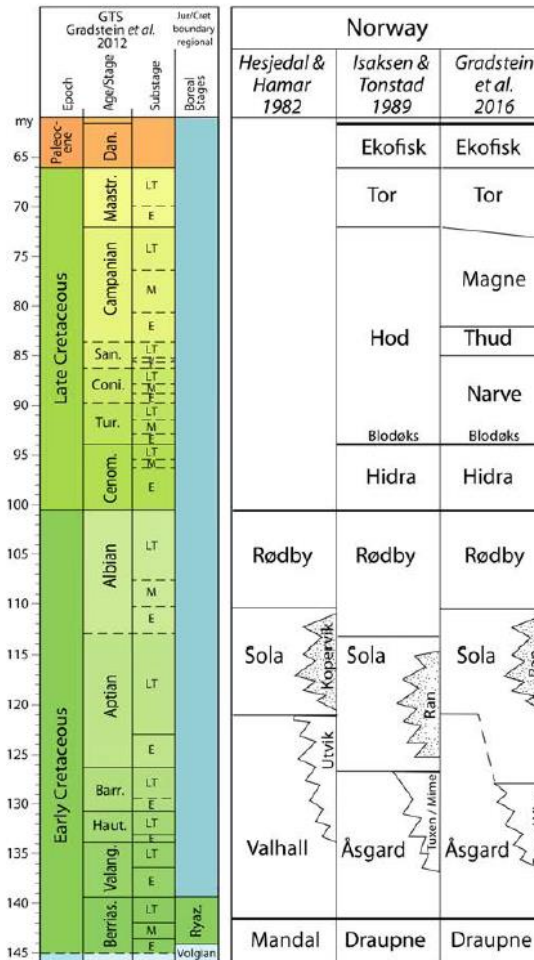


Figure 4. Stratigraphy column of the Cretaceous in the northern North Sea (van Buchem et al., 2018).

a. Åsgard Formation (late Ryazanian-Barremian)

The age of the Åsgard Formation ranges from Late Ryazanian to Late Hauterivian. In some parts where neither the Tuxen nor the Sola Formation are recognized, the Åsgard Formation represents the lateral equivalent of these formations and reach a Late Aptian to Early Albian age.

The lithology is dominated by light to dark grey, greenish and brownish, often calcareous claystones, which transition into light grey, light greenish-grey marlstones and stringers of limestone. Siltstone or fine sandstone laminae exist within the claystones. Micas, pyrite and glauconite are common.

This formation was deposited in an open marine, low-energy shelf environment with well-oxygenated bottom water (Bugge et al., 2001).

b. Sola Formation

In the northern North Sea, the Sola Formation has a Mid Aptian to Early Albian age. It consists of shales interbedded with stringers of marlstone and limestone. The shales are finely laminated, and are mainly black or dark gray, sometimes olive-gray brown or red (Isaksen and Tonstad, 1989).

The dark shales of the Sola Formation are characterized by high gamma radiation, which suggests deposition in a marine, anoxic depositional environment. The high gamma-ray level in the lower Aptian is interpreted to represent maximum flooding. This is one of the major transgressions in the Cretaceous (Bugge et al., 2001).

c. The Rødby and Agat Formations (Albian)

The Albian period was dominated by hemipelagic deposition of clay interrupted by the sandy product of gravity flow events. The claystone is assigned to the Rødby Formation, while the sandstone is associated to the Agat Formation (Bugge et al., 2001). The Albian is characterized by regressive stages within an overall transgressive period (figure 5).

The Rødby Formation is widely distributed in the North Sea. Its lithology consists of mainly red-brown, green and grey marlstones. Glauconite and pyrite may also be present. This formation was deposited in an open marine, oxygenated environment with limited clastic supply (Jackson et al., 2008).

The Agat Formation is locally recognized in the Måløy Fault Block (blocks 35/1 and 36/1 in the Norwegian Sector) and is thought to be encountered along the western boundary of the Fennoscandian Shield. It consists of white to light grey, fine- to medium-grain, moderately to well-sorted sandstones alternating with grey claystones. The sandstones are usually micaceous and glauconitic and sometimes contain small amounts of pyrite. The sandstones may also have carbonate- and silica-cemented zones. On the other hand, the dark grey claystones between the sandstones can be variable in thickness (0.5-5m) and may contain variable amounts of siltstones. The Agat Formation is interpreted as being deposited by gravity flows in a marine environment (Jackson et al., 2008).

d. The Svarte Formation (Cenomanian)

The Svarte Formation generally consists of mudstones interbedded with limestones, which were deposited in an open marine environment. The sandstones, which resulted from gravity mass flows, occur scatteredly. The Svarte Formation overlies the underlying Lower Cretaceous

sediments, suggesting a minor tectonic event with basin floor subsidence and flank uplift at this time (Bugge et al., 2001).

e. The Blodeks Formation (latest Cenomanian-early Turonian)

The Blodeks Formation is present throughout the North Sea, although it is lacking on local highs such as the Sørvestlandet, Utsira, Mandal, Jæren and Sele highs. This formation contains red, green, grey and black shales and mudstones, which are non-calcareous to moderately calcareous. This formation was deposited during a period characterized by anoxic bottom conditions (Isaksen and Tonstad, 1989).

f. The Tryggvason Formation (early-middle Turonian)

The Tryggvason Formation is identified in the Viking Graben and northern Tampen Spur area towards the Marulk Basin. It consists mainly of mudstones with interbedded limestones, corresponding to an open marine depositional environment. The mudstones are light to dark grey, often calcareous and occasionally micaceous, glauconitic and pyritic. The limestones are white to light grey or brownish grey and argillaceous. The sandstones are clear to light grey, very fine to fine grain and calcite cemented (Isaksen and Tonstad, 1989).

g. The Kyrre Formation (late Turonian-Campanian)

The Kyrre Formation is present in the Viking Graben on the Tampen Spur and the western margin of the Horda Platform. It consists mainly of mudstones with occasional limestones and sandstones. The mudstones are medium grey to grey, silty to calcareous, occasionally pyritic, glauconitic or micaceous. The sandstones are clear to white, and very fine to fine grain. The depositional environment of this unit is thought to be open marine (Isaksen and Tonstad, 1989).

h. The Jorsalfare Formation (Maastrichtian)

The Jorsalfare Formation consists of mudstones interbedded with thin limestone beds. This unit is distributed in the Viking Graben and on the Tampen Spur. It is time-equivalent with the Hardråde Formation on the Horda Platform and the Tor Formation on the Utsira High. The mudstones are light to medium grey, often calcareous, while the limestones are white to light grey, fine grain, occasionally sandy and dolomitic. These sediments were deposited in an open marine environment (Isaksen and Tonstad, 1989).

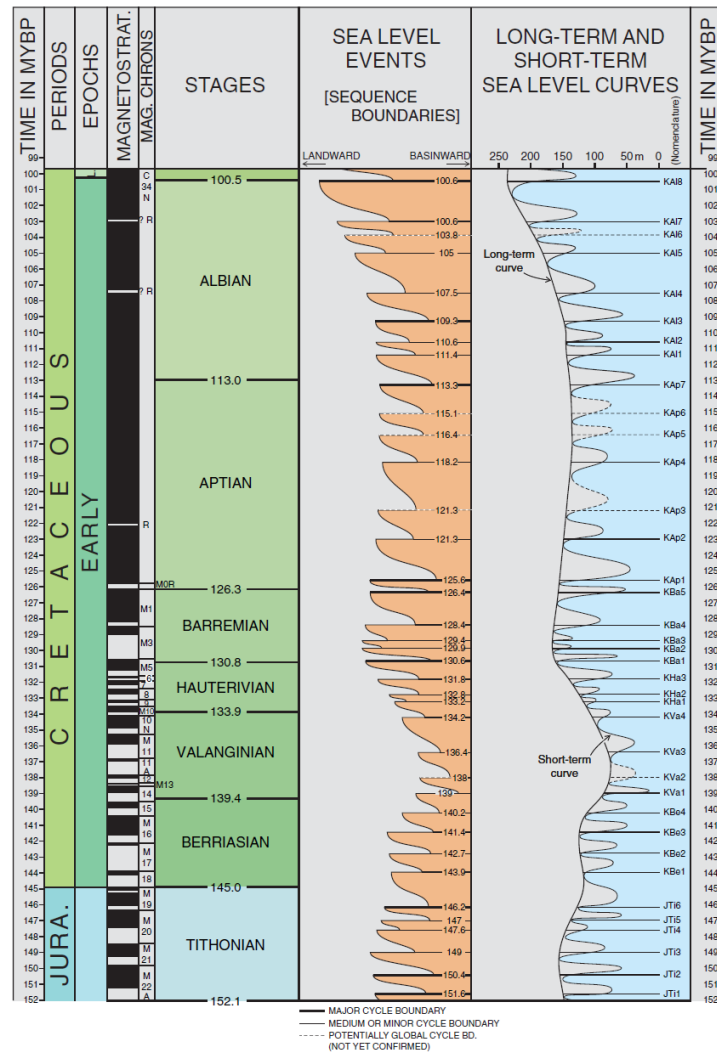


Figure 5. Inferred sea level variation in Early Cretaceous (Haq, 2014).

## 2.4 The Study Area

The study area is bounded by two main fault systems: the north-south trending Øygarden fault Complex to the east, and the parallel Gjøa fault in the west. A series of north-south trending fault blocks related to the Late Jurassic North Sea rifting dissect the block, offsetting the Middle Jurassic Brent Group to the lowest Cretaceous sediments. An Upper Jurassic unconformity can be mapped over the region. This unconformity marks the climax of Late Jurassic rifting, recognized as a series of east-west oriented canyons that were active from the Latest Jurassic

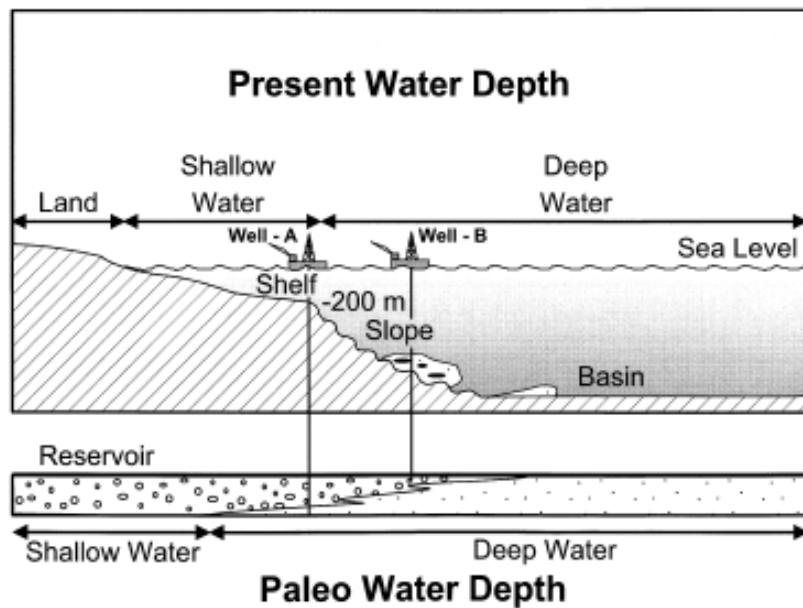
to the Early Cretaceous. These canyons are key features for the location of stratigraphic traps, of both Upper Jurassic and Lower Cretaceous age. Upper Jurassic shales and Lower Cretaceous sediments fill the rift-related topography, with thick Upper Cretaceous sediments completely infilling the basin.

As a result, the structural elements (faults) are predominantly oriented N-S (Figure 3), normal to the direction of extension during the major main rifting phase (Jurassic). In addition, a SE-NW structural fabric is also observed. This fabric may be related to basement structures linking the main rifting fault segments (Zanella and Coward, 2003).

### 3. Theory

#### 3.1 Sedimentology background

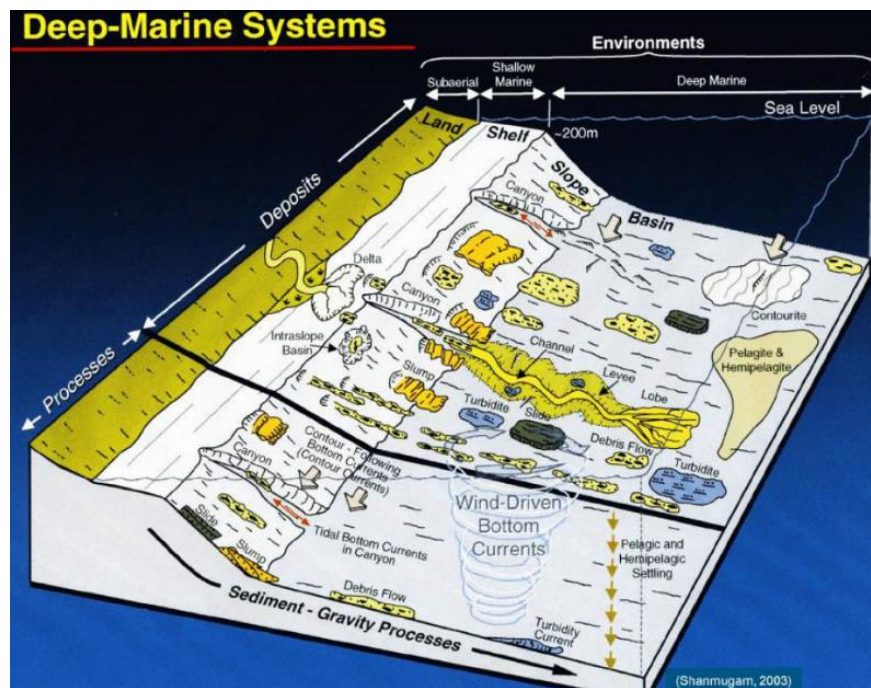
The term “deep water” refers to a water depth  $> 200$  m environment, where sediment-gravity processes such as slides, slumps, debris flows and turbidity currents, or bottom currents (contourites) dominate (Shanmugam, 2000). Geologists usually consider the term “deep water” to illustrate the depositional origin of the reservoir (Figure 6).



*Figure 6. The deep-water environment (Shanmugam, 2000).*

### 3.1.1 Deep-marine processes

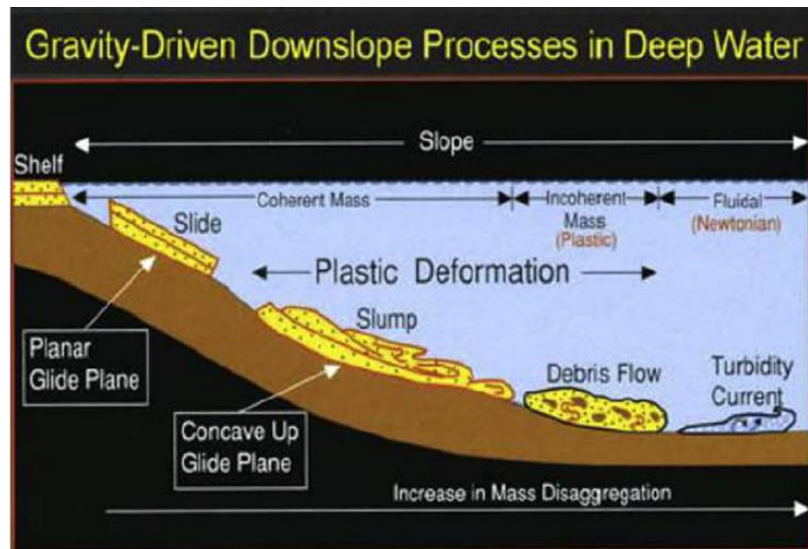
To understand the nature of sediment transport and deposition in the deep sea, it is important to classify and distinguish the mechanism of the processes acting in this setting. Figure 7 shows the marine sedimentary environment with acting processes, including mass transport (i.e. slices, slumps, and debris flow), turbidity currents, and bottom currents. The deposits associated to these processes are shown as well.



**Figure 7.** Schematic diagram showing the deep-marine sedimentary environment with the different processes and their deposits. Water depth is > 200 m (shelf-slope break) (Shanmugam, 2018).

Numerous schemes have been used to characterize sediment-gravity flows, such as rheology (Dott, 1963), sediment-support mechanisms (Middleton and Hampton, 1973), or both (Lowe, 1982, Lowe, 1979). Four common types of gravity-driven downslope processes that transport sediments into the deep marine basin floor are summarized in Figure 8 (Shanmugam, 2018):

- A *slice* represents a coherent translational mass transport of a block or strata on a planar glide plane (shear surface) without internal deformation.
- A *slump* represents a coherent rotational mass transport of a block or strata on a concave-up glide plane (shear surface) with internal deformation



Sediment concentration	Sediment concentration: 100% by volume	25-100%	1-23%
Mechanical behavior	Mass-transport processes Mechanical behavior: Elastic and plastic		Viscous fluid
Sand concentration	Sandy mass-transport deposits (SMTD): Sand concentration: > 20% by volume		Turbidite

**Figure 8.** Schematic diagram of four common types of gravity-driven downslope processes that transport sediments into the deep-marine environments, edited after (Shanmugam, 2018).

- With addition of fluid during downslope movement, slumped material may transform into a debris flow. A debris flow is a sediment flow with Bingham plastic rheology and laminar state, in which deposition occurs through “freezing en masse” (Nardin et al., 1979). Intergranular movement predominates over shear-surface movement in this flow.
- As fluid content increase, the flow evolves into a turbidity current, which has Newton rheology and turbulent state. The sediments are supported by turbulence and they get deposited by suspension. This flow can be divided into high-density turbidity currents and low-density turbidity currents, based on flow density or sediment concentration by flow volume. Shanmugam (1996) summarizes different criteria that characterize this flow (Table 1):



**Table 1.** Criteria characterizing high-density turbidity currents and low-density turbidity currents (Shanmugam, 1996).

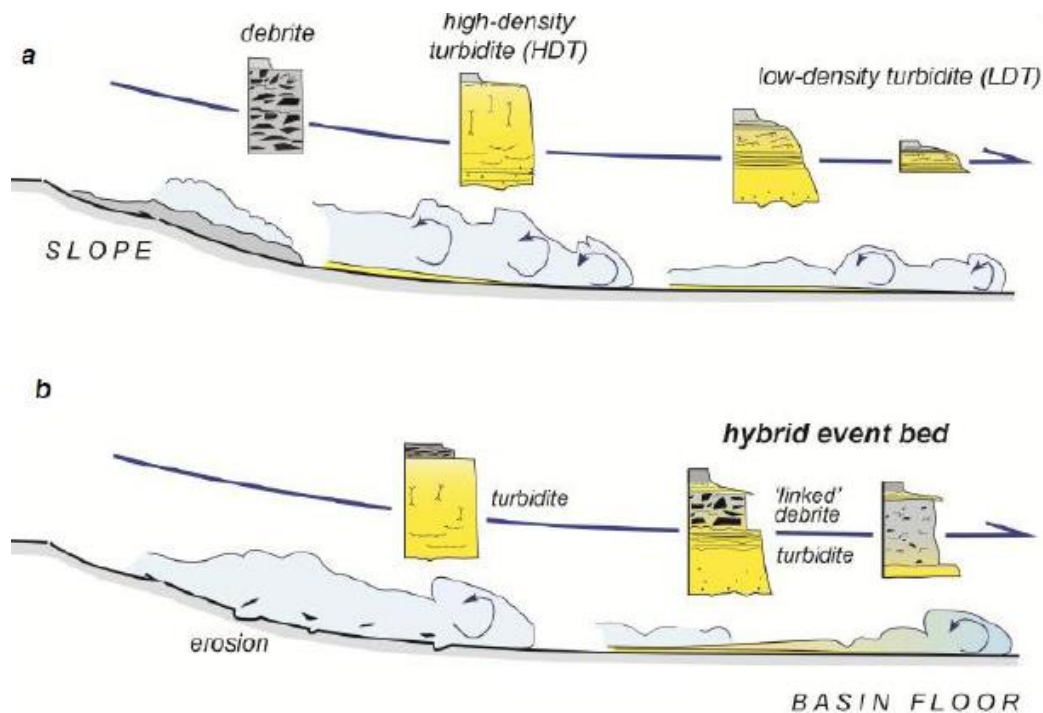
<p><b>Low-density turbidity currents</b></p> <ul style="list-style-type: none"><li>• &lt;1% sediment by weight (Middleton, 1993)</li><li>• &lt;6% solids by volume (Pickering et al., 1989) or &lt;1.1 g/cm<sup>3</sup> (Kuenen, 1966)</li><li>• 23% solids by volume (Middleton, 1967)</li></ul>
<p><b>High-density turbidity currents</b></p> <ul style="list-style-type: none"><li>• &gt;6% solids by volume (Pickering et al., 1989) or &gt;1.1 g/cm<sup>3</sup> (Kuenen, 1966)</li><li>• &gt;10% sediment by weight (Middleton, 1993)</li><li>• &gt;20-30% solids by volume (Lowe, 1982)</li><li>• 35-40% solids by volume (Postma et al., 1988)</li><li>• 44% solids by volume (Middleton, 1967)</li></ul>

### 3.1.2 Hybrid sediment gravity flow deposits

Various intermediate flow states might operate on submarine slopes, which lead to different vertical profiles of event beds. According to Haughton (Haughton et al., 2003, Haughton et al., 2009) and Talling (Talling, 2013), sand-bearing gravity currents can evolve with the run-out flow in two different ways:

- (1) The flow may remain largely turbulent (apart from high-concentration near bed layers) and become increasingly dilute as it deposits and mixes with the ambient water. This flow evolves from high-density turbidity currents proximally to low-density turbidity currents distally, which results in a conventionally graded and parallel or ripple-laminated deposit. Bed thickness and grain size decline systematically down dip (Figure 9a) (Haughton et al., 2009).
- (2) Alternatively, cohesive forces may have a big impact in decelerating the flow. This happens where a turbulent current initially carrying significant clay from the source, increases the amount of clay via erosion, or is able to isolate clay into the lateral or rearward parts of the flow. The clay can diminish turbulence and force parts of the flow to behave as transitional or laminar flow. This process leads to a *hybrid event bed* (Figure 9b), with parts dominated by a turbidity current, while other parts are deposited by sections of the flow with reduced turbulence. When the turbulence is completely

suppressed, a “*linked debrite*” will occur. This is a clast-bearing chaotic argillaceous sand, often with abundant mica and carbonaceous material, indicating that strong density and shape segregation has occurred within the original current to concentrate these components (Haughton et al., 2009).



**Figure 9.** Illustration of contrasting downstream evolution involving: (a) progressive dilution of a turbidity current and (b) transformation of a turbidity current to a hybrid flow. Edited after (Haughton et al., 2003, Haughton et al., 2009).

According to Haughton et al. (Haughton et al., 2009), sediment gravity flow deposits can be classified as:

- (1) Debrite: accumulated due to freezing of laminar or weakly turbulent cohesive flows.
- (2) Low-density turbidites: deposited by dilute and fully turbulent non-cohesive flows
- (3) High-density turbidites: settled by concentrated non-cohesive flows with suppressed near-bed turbulence and particle support.
- (4) Hybrid flow deposits: deposited by flows that transition or switch from non-cohesive to cohesive behavior during deposition.

## 3.2 Stratigraphy Forward Modeling

### 3.2.1 Diffusion

In the GPM software, sediment diffusion is used to model secondary transport mechanisms such as soil creep or minor slumps which occur at a small scale (smaller than a cell size). The simulation of diffusion assumes that sediment has a downslope movement rate that is proportional to the tangent of the slope angle and diffusion coefficient. This coefficient represents the physical characteristics of the sediment (Tetzlaff et al., 2007).

Consider that a sediment type accumulates on top of a topographic surface represented by a function  $z = f(x, y, t)$ , then the sediment flux  $\varphi$  caused by diffusion result in the function (1):

$$\varphi = -k\nabla z, \quad (1)$$

where  $\varphi$  = sediment flux ( $L^2T^{-1}$ ),  $k$  = diffusion coefficient ( $L^2T^{-1}$ ), and  $\nabla z$  = elevation gradient (unitless) (Tetzlaff et al., 2007).

Because of sediment continuity, the topographic elevation at a fixed point is altered over time as the divergence of the sediment flux:

$$\frac{\partial z}{\partial t} = \nabla \cdot \varphi, \quad (2)$$

Equation 1 and 2 result in:

$$\frac{\partial z}{\partial t} = -k\nabla^2 z, \quad (3)$$

which is a classical Laplacian diffusion equation for a single sediment type with constant diffusion coefficient (Tetzlaff et al., 2007).

Additionally, GPM defines a property called the equivalent particle diameter, which characterizes the sediment ability to be moved. Equation 4 describing the relationship between the diffusion coefficient and the equivalent particle diameter is illustrated in Figure 10.

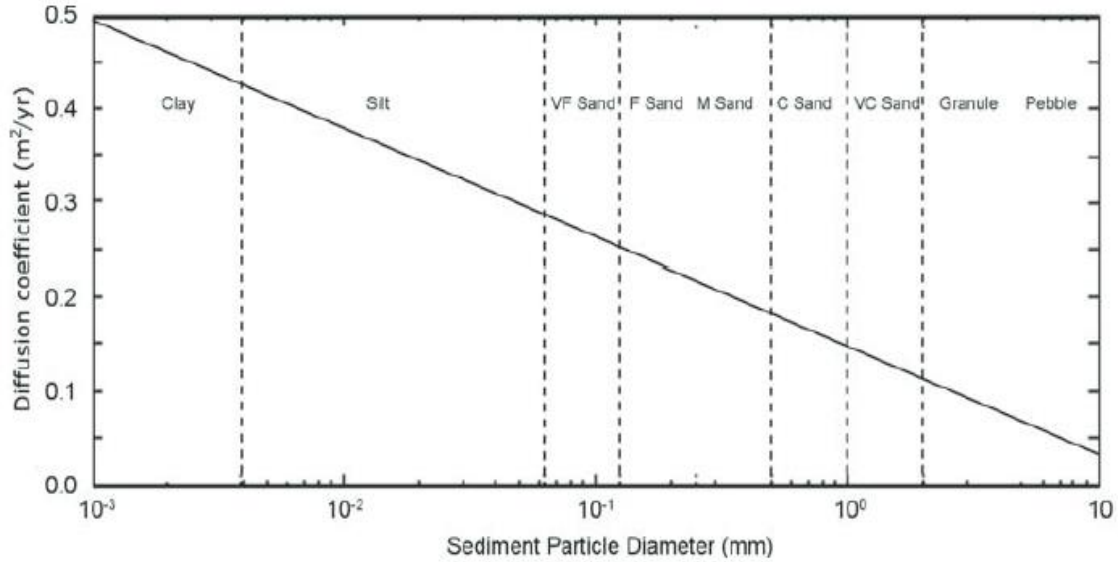
$$k_d = \frac{\ln(d)}{20} + 0.15, \quad (4)$$

where  $k_d$  = diffusion coefficient in  $m^2/yr$ ,  $d$  = diameter in mm, and  $\ln$  = natural logarithm.

The total diffusion coefficient for a specific sediment type at one point is given by the Equation 5 (Tetzlaff et al., 2007):

$$k_T = k_d(k_z + k_x), \quad (5)$$

Where  $k_T$  = total diffusion coefficient (L<sup>2</sup>T<sup>-1</sup>),  $k_d$  = diameter dependent coefficient (given by equation 4) (L<sup>2</sup>T<sup>-1</sup>),  $k_z$  = depth and elevation-dependent term (unitless), and  $k_x$  = external diffusion term (including wave-dependent diffusion).



**Figure 10.** Dependency of the sediment diffusion coefficient ( $k_d$ ) on the grain size used by the GPM model (Tetzlaff et al., 2007).

### 3.2.2 Free surface flow modeling

GPM applies free-surface flow modeling to simulate the flow in different forms such as shallow water currents, turbidity flows, or rivers. The behavior of the flow is based on two equations: the continuity equation and the momentum equation (Tetzlaff et al., 2007). The two-dimensional continuity equation can be written in the following form:

$$\frac{\partial h}{\partial t} = -\nabla \cdot (h\vec{Q}), \quad (6)$$

where  $h$  = flow depth (L),  $t$  = time (T),  $\nabla$  = two-dimensional divergence, i.e., if  $\vec{V} = (u, v)$ , then  $\nabla \cdot \vec{V} = \left(\frac{\partial u}{\partial x} + \frac{\partial v}{\partial y}\right)$ , and  $\vec{Q}$  = horizontal flow-velocity vector (LT<sup>-1</sup>). Equation 6 shows that if the flow diverges, its depth will decrease and vice versa.

The effect of forces on the flow is described by the momentum equation (Equation 7):

$$\frac{D\vec{Q}}{Dt} = -g\nabla H + \frac{c_2}{\rho}\nabla^2\vec{Q} - \frac{c_1\vec{Q}|\vec{Q}|}{h} + a_x, \quad (7)$$

where  $\frac{D\vec{Q}}{Dt}$  = Lagrangian derivative of horizontal flow-velocity vector with respect to time ( $LT^{-1}$ );  $g$  = gravitational acceleration ( $LT^{-2}$ );  $\nabla H$  = gradient of the water surface elevation (unitless);  $c_2$  = fluid friction coefficient ( $ML^{-1}T^{-1}$ );  $\rho$  = fluid density ( $ML^{-3}$ ); and  $\nabla^2$  = two-dimensional vector second derivative, i.e., if  $\vec{V} = (u, v)$ , then  $\nabla^2\vec{V} = \left(\frac{\partial^2 u}{\partial x^2} + \frac{\partial^2 u}{\partial y^2}, \frac{\partial^2 v}{\partial x^2} + \frac{\partial^2 v}{\partial y^2}\right)$ ;  $c_1$  = bottom friction coefficient (unitless); and  $a_x$  = acceleration due to external forces (including wave-induced acceleration) ( $LT^{-2}$ ).

Equation 7 expresses that the flow acceleration is controlled by:

- (1) The elevation of the water surface and the gravity (i.e., acceleration of downslope movement).
- (2) Friction within the fluid (between portions of the fluid against each other) (i.e., macroscopic viscosity).
- (3) Friction between the fluid and the bottom surface.
- (4) Acceleration due to external forces, such as wave action.

The combination of equations 6 and 7 sets the initial boundary conditions of the flow simulation in GPM.

The GPM model implements the flow using two different methods (Tetzlaff and Harbaugh, 1989, Tetzlaff et al., 2007): (1) A Lagrangian particle-in-cell method, which is suitable for unsteady flow (i.e., turbidites), (2) A finite difference method, which is appropriate for steady or quasi-steady flow (i.e., a river flow at normal stage or longshore currents).

### 3.2.3 Particle-based numerical methods

This method is based on the momentum and continuity equations and it captures the movement of a small elemental column of water, which contains a number of fluid elements over a fixed rectangular grid. This process is controlled by: (1) the slope and gravity, (2) the friction of fluid particles against the surface, and (3) the friction between fluid particles with each other. The method can monitor the position, velocity, and depth of each water column. Furthermore, the method uses all the elements contained in a cell of the grid, hence it is called “particle-in-cell” method. This allows the calculation of the average properties of the flow, such as flow depth and velocity (Tetzlaff and Harbaugh, 1989).

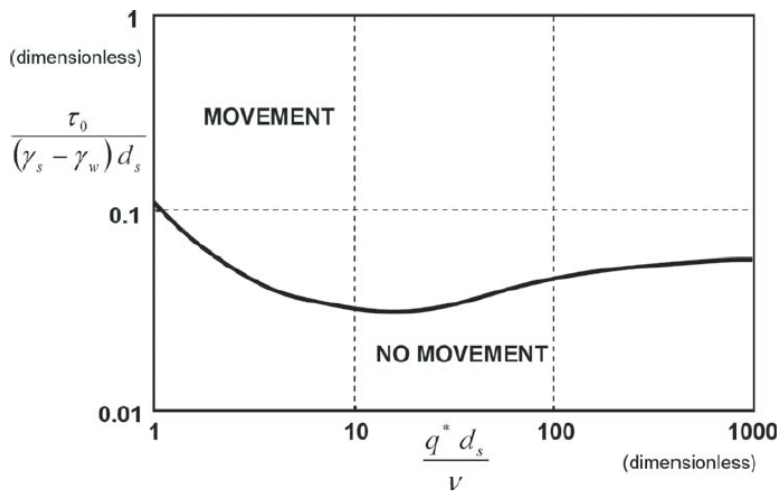
### 3.2.4 Sediment transport modeling

The same particles that simulate the flow can be used to track the sediments. Each particle can be associated with a certain amount of each type of sediment. The model contains two main sediment-transport criteria that control the amount of sediments to be eroded, transported in the flow, and eventually deposited:

1. Shields' criterion (Shields et al., 1936), which expresses that the flow velocity at the water sediment interface must surpass the shear stress defined by the sediment grain properties (Figure 11) to be able to lift the sediment. The flow velocity used by the Shield's criterion is predicted by the flow model (Equations 6 and 7)
2. A transport capacity criterion (derived from the flow conditions), which specifies the amount of sediment of each grain size that can be carried by the flow (this is explained later in Equations 8, 9, and 10). (Tetzlaff et al., 2007)

Figure 11 illustrates the threshold of sediment movement based on the Shield criterion (Tetzlaff et al., 2007), where:

- $q^*$  = shear velocity ( $LT^{-1}$ ) =  $\sqrt{\frac{\tau_0}{\rho_w}}$ , where  $\rho_w$  = water density ( $ML^{-3}$ );
- $d_s$  = sediment particle diameter (L);  $\nu$  = water kinematic ( $L^2T^{-1}$ )
- $\gamma_s$  = sediment particle specific gravity ( $LT^{-2}$ )
- $\gamma_w$  = water specific gravity ( $ML^{-2}T^{-2}$ )
- $\tau_0$  = bottom shear stress ( $ML^{-1}T^{-2}$ )



**Figure 11.** Diagram displaying the threshold of sediment movement based on the Shields' criterion (Tetzlaff et al., 2007, Shields, 1936).

The transport capacity specifies the sediment carried by the flow if there is enough sediment at the base and the Shields' criterion is satisfied (Tetzlaff et al., 2007). It is written as follows:

$$T_c = c_t \frac{|Q|^2}{h}, \quad (8)$$

where  $T_c$  = transport capacity ( $L^2T^{-1}$ ),  $c_t$  = transport coefficient (LT), a constant estimated from field transport data,  $Q$  = flow velocity ( $LT^{-1}$ ), and  $h$  = flow depth (L).

The effective sediment flow is a term which is used to normalize the mixtures of sediments in the flow. It represents the flow containing one hypothetical sediment type that could be transported as easy as the actual mixture of several grain sizes (Tetzlaff et al., 2007). Each sediment type contributes to the effective flow  $F_e$  in inverse proportion to its "transportability", as follows:

$$F_e = \sum_{i=1}^N \frac{f_i}{r_i}, \quad (9)$$

where  $F_e$  = effective flow ( $L^2T^{-1}$ ),  $N$  = number of sediment types,  $f_i$  = actual flow of each sediment type ( $L^2T^{-1}$ ), and  $r_i$  = transportability of each sediment type, which in turn is a function of its equivalent particle diameter (unitless). (Tetzlaff et al., 2007).

The flow of sediment transferred between the water and the underlying bed is then defined by:

$$F_t = F_e - T_c, \quad (10)$$

where  $F_t$  = sediment flow transferred between water and bed ( $L^2T^{-1}$ ) (positive when deposition occurs),  $F_e$  = effective flow (Equation 9) ( $L^2T^{-1}$ ), and  $T_c$  = transport capacity (Equation 8) ( $L^2T^{-1}$ ) (Tetzlaff et al., 2007).

Erosion can occur if the shear stress surpasses the Shields' threshold for the coarsest grain at the bottom, and the flow's transport capacity exceeds the effective sediment load currently carried by the flow. Erosion leads to the decrease of the topography elevation at the particle's location, and adds the equivalent amount of sediment to the moving particles (Tetzlaff et al., 2007)

Deposition can occur if the equivalent sediment load exceeds the transport capacity (in this case, shear stress has no impact on deposition). Additional rules are used to manipulate multiple sediment sizes: If erosion occurs, the bulk mixture at the bottom is picked up. If deposition happens, the coarsest fraction is deposited first (Tetzlaff et al., 2007).

## 4. Data

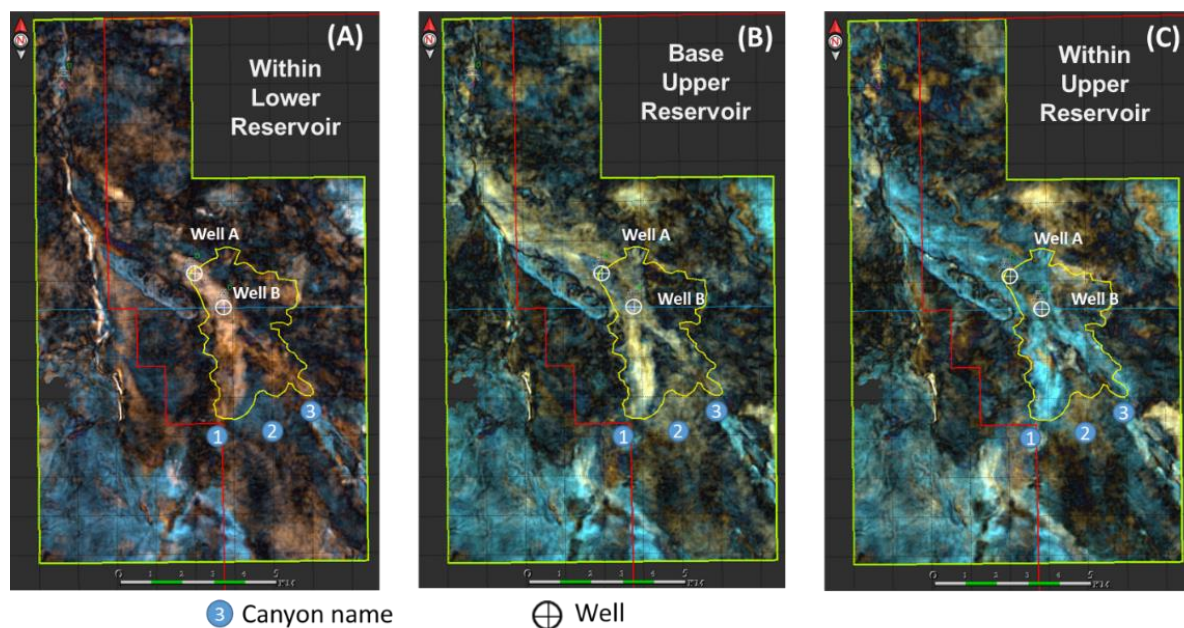
The available data set consists of two wells and seismic spectral decomposition time slices of the lower and upper reservoir (Figure 12). Due to the confidential nature of these data, the two wells were renamed as Well A and Well B. The seismic horizons of the top and base reservoir were given in depth domain together with the reconstructed paleo bathymetry maps (Figure 13). In addition, an internal sedimentology report provided the complete core description and presented the conceptual depositional model.

## 5. Previous work

### 5.1 Seismic spectral decomposition

From discussions with Neptune Energy, the reservoir sandstones could be recognized as bright streaks in the time slices of seismic spectral decomposition (Figure 12). These bright streaks (orange in figure 12A, yellow in figure 12B, and blue in figure 12C) have one branch from the south, another branch from the southeast, and head to the northwest.

It could be inferred that the turbidite sandstones in the reservoir can come from two sources: the first source from the south direction, which corresponds to canyon 1 (Figure 13), while the second source from southeast direction, which corresponds to canyon 3 (Figure 13). The lower reservoir sandstones were laterally narrow, stretched up to well A and did not extend farther than the Gjoa fault (Figure 13). The upper reservoir was less constrained and spread much farther away from well A in northwest direction.



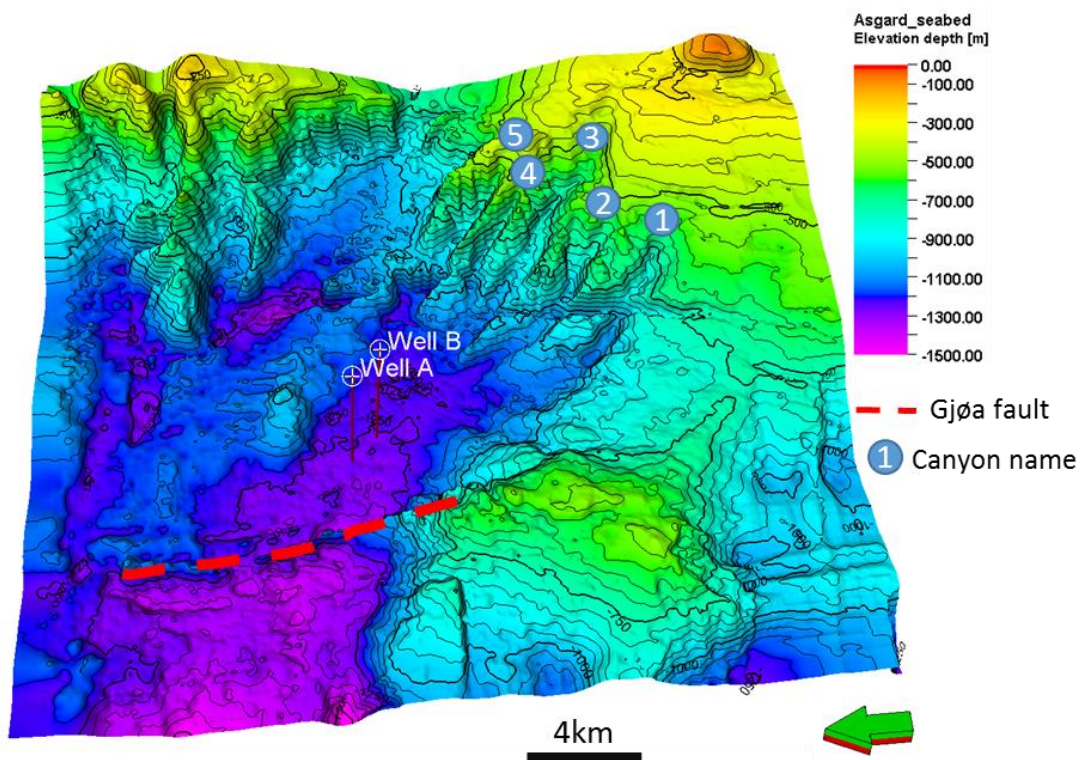
**Figure 12.** Time slices of seismic spectral decomposition at different intervals within the reservoir: (A) Within the lower reservoir, (B) Base of the upper reservoir, (C) Within the upper reservoir (images from Neptune Energy).



## 5.2 Structural reconstruction

A detail structural restoration of the Gjøa area (3D-backstripping) was conducted based on nine seismic horizons from Top Brent to Quaternary plus the seabed and a regional restoration study (Roberts et al., 2019). The stratigraphic interval of interest is between the Top Åsgard and the Top Rødby formations. Both the BCU and the Top Svarte Formation also provide a good understanding of the evolution of the depositional framework during the Jurassic-Cretaceous period. A summary of the four horizons and their age is included in Table 2.

The Åsgard paleo-topography map (Figure 13) was used as the base map of the model. The actual base reservoir is the Top Sola Formation. However, this surface has large uncertainty in the interpretation process due to low seismic resolution. Therefore, the paleo-topography map of the Åsgard Formation, which was deposited before the Sola Formation and is quite conformable to Top Sola map, was chosen as the base reservoir in the model. However, from the above assumption, the Åsgard paleo-topography map contains large uncertainties which will be addressed in section 6.1.



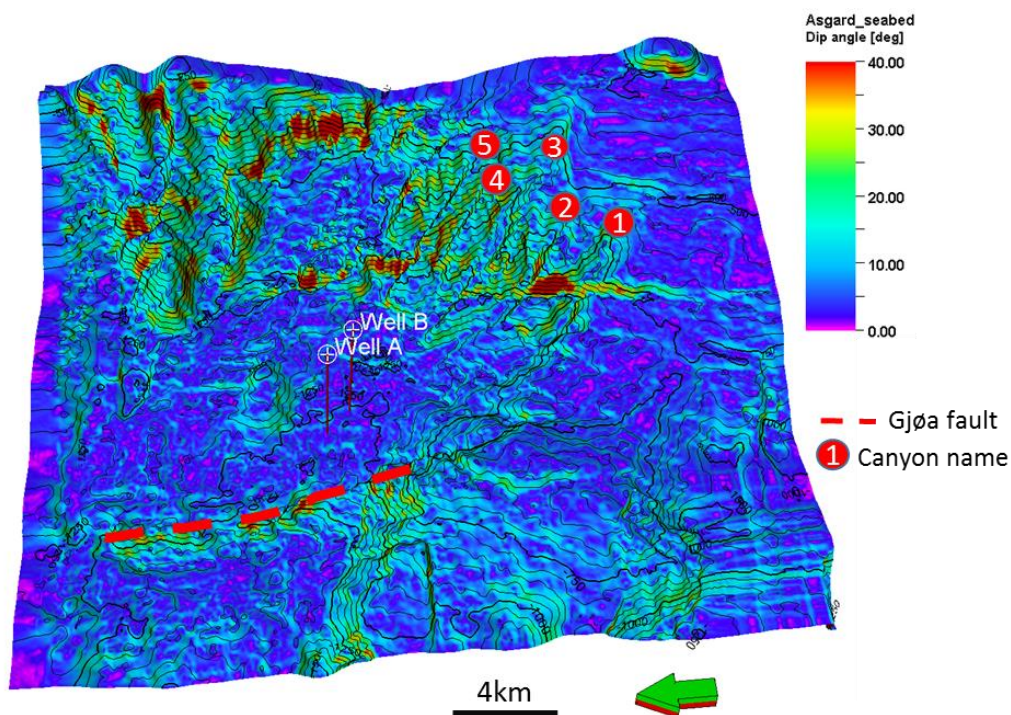
**Figure 13.** Top Åsgard paleo-topographic map from the structural reconstruction of the area. This map was used as the initial base map of the turbidite model (image from Neptune Energy).

The Åsgard paleo-topography map (Figure 13) suggests that five canyons (1 to 5) brought the turbidite sediments from the sources to the basin.

**Table 2.** Reconstructed seismic horizons used for analyzing and modeling the turbidite.

Number	Seismic horizon	Age (Million years)
1	Top Svarte	94
2	Top Rødby	100
3	Top Åsgard	126
4	Base Cretaceous Unconformity	140

A dip angle attribute of the Åsgard paleo-topography map (Figure 14) was made to highlight the slopes. This map shows that the topography at the well locations is quite gentle (dip angle  $\approx 0$  degree), and the slopes at the five canyons are quite steep (dip angle  $\approx 15$ -30 degree). Additionally, in figure 14, the Gjølfa fault can be distinguished by high linear relief (marked in dash line). This fault could have influenced the reservoir lateral extension (see section 5.4).



**Figure 14.** Dip angle attribute map of the Åsgard paleo-topography map (image from Neptune Energy).

### 5.3 Biostratigraphic framework

A biostratigraphic analysis by Neptune Energy of wells A and B (Clerc et al., 2018) gives the following information:

- The turbiditic sands exclusively are Late Albian in age.
- The Middle Albian is eroded at well B, but partly preserved at well A

### 5.4 Chlorite provenance study

According to a study by Neptune Energy of chlorite provenance in the core data from well B, there is a difference in chlorite coating between the lower and upper reservoir, which might be related to the depositional environments. The main conclusions of this study are summarized in Table 3:

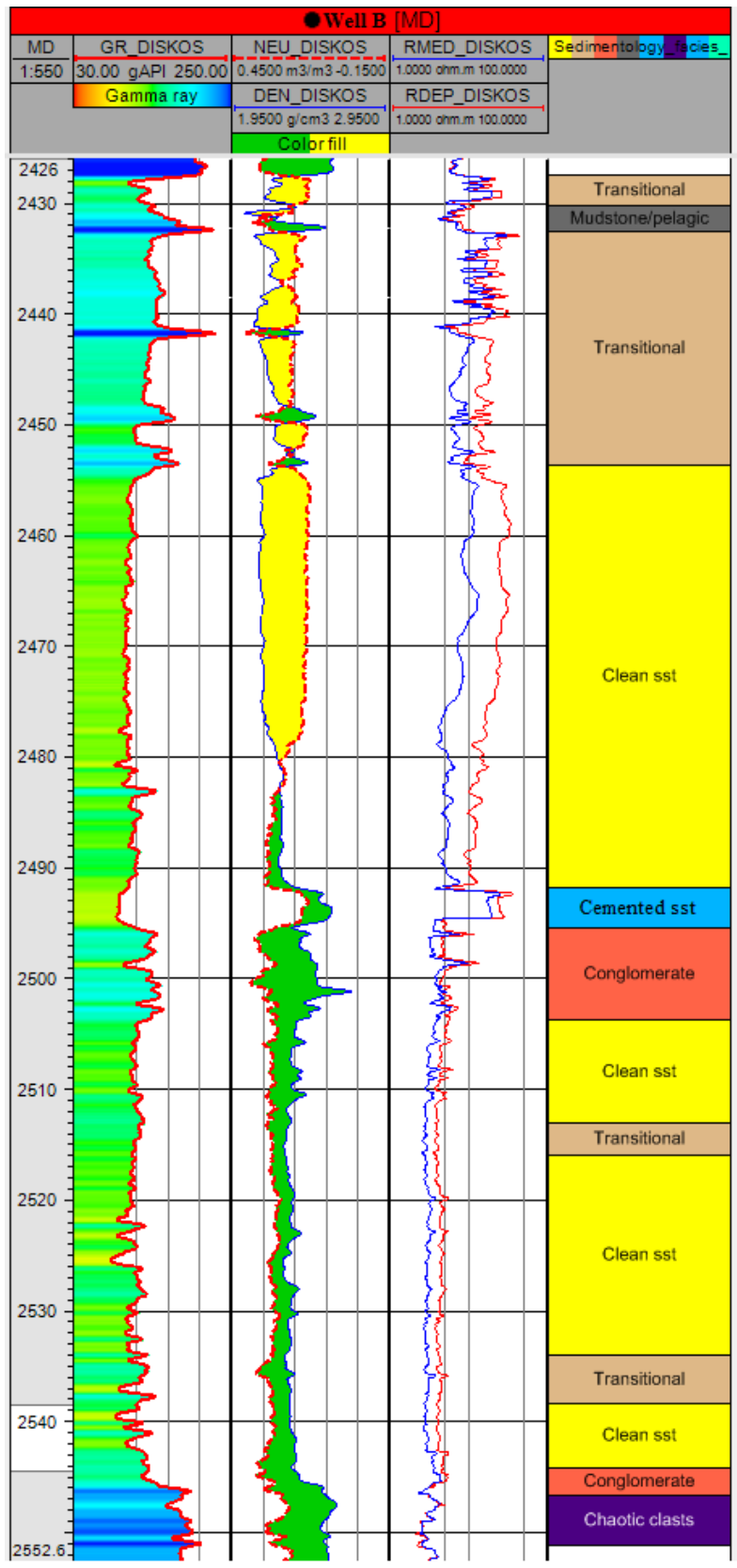
*Table 3. Summary of chlorite provenance from a Neptune Energy study in the lower and upper reservoir*

	<b>The lower reservoir</b>	<b>The upper reservoir</b>
Chlorite coating	High Chlorite and thick coating	Low Chlorite
Relative position in the system	More distal part of sediment feeder system	More proximal part of the delta system
Depositional environment	Subtidal part of delta front or prodelta	Upper delta front or lower delta plain

In short, the sandstones from the lower and upper reservoir have different origins and can be distinguished by chlorite properties. This is the essential information, because the simulation results should clearly separate these two different origins.






### 5.5 Sedimentology analysis

Based on the core and log data, a facies log was created by Neptune Energy for well B, with five facies associations (Figure 15). The description of the facies associations is shown in Table 4, and the core images for each facies association are shown in Table 5.

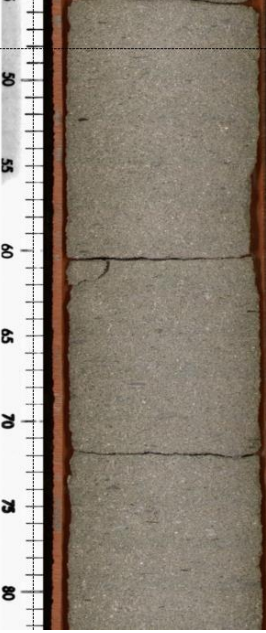



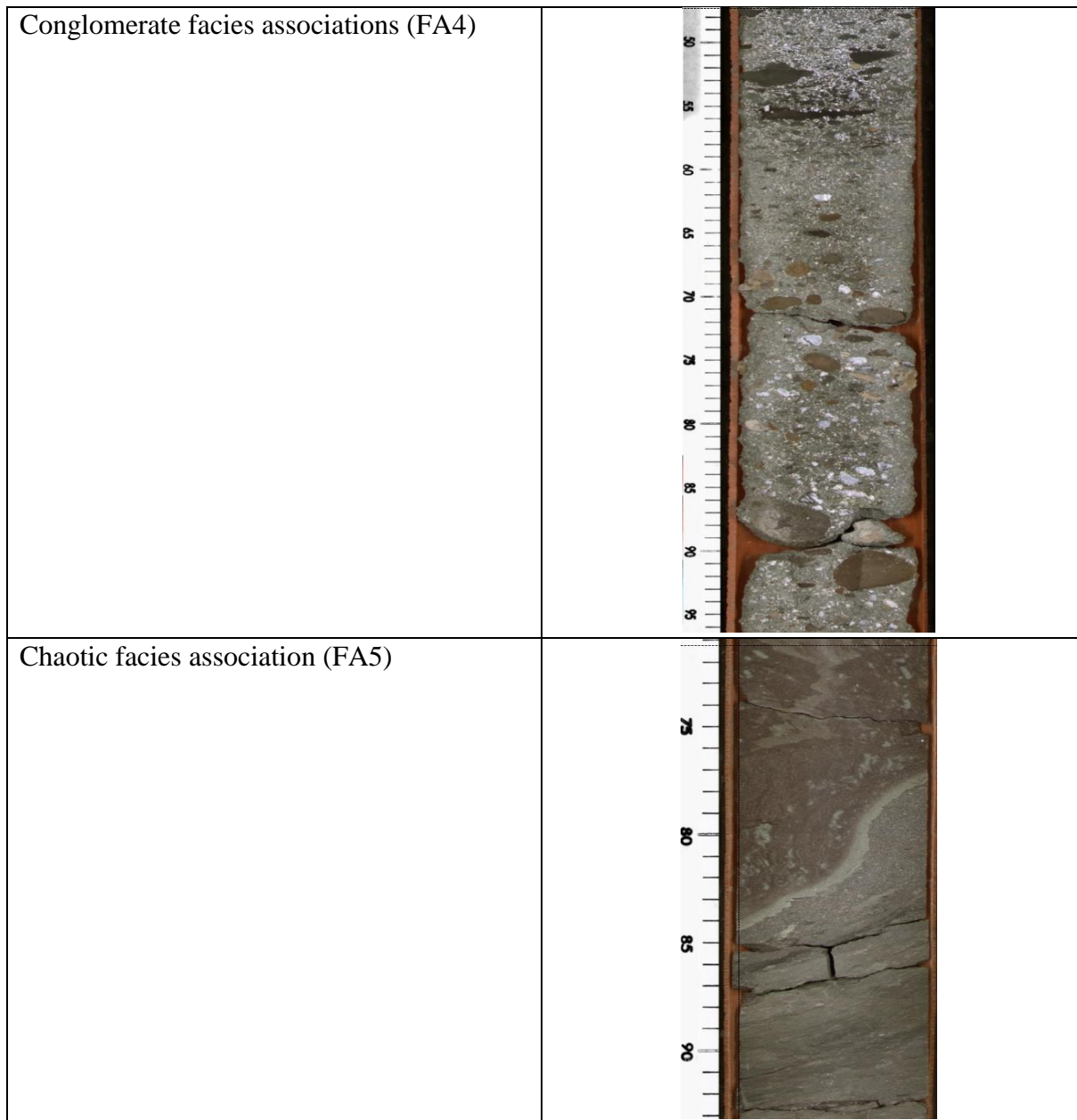
*Figure 15. Facies interpretation of well B (edited after (Clerc et al., 2018)).*

**Table 4.** Facies Associations summary by (Neptune Energy internal report)

<b>Name</b>	<b>Symbol</b>	<b>Color</b>	<b>Description</b>	<b>Interpretation</b>
Clean Sandstones facies association	FA1		Massive fine to very coarse sandstones, displaying a fining-upward trend They are sometimes carbonate cemented. They have sharp or erosive bases. Sand-on-sand amalgamation is frequent in turbidite beds (meters)	Deposited by high to low density turbidity currents axis
Transitional Sandstones facies association	FA2		Clean, moderately to well sorted, lower medium grained to upper fine grained sandstones.	Deposited by transitional flow, alternating between cohesive and turbulent conditions
Mudstone/siltstone facies associations	FA3		Dark grey, micaceous, swelling siltstones	Deposited by hemipelagic suspension or dilute waning gravity flow
Conglomerate facies associations	FA4		Granular and pebble conglomerate, moderately to poorly sorted Medium to coarse grained sandstone, containing large clasts of dark grey mudstone, Clasts are typically horizontally aligned. Visual porosity is very low in the sandstone matrix, due to compaction	Deposited by high density turbidity currents, associated to bypass zone
Chaotic facies association	FA5		Matrix supported siltstone to fine sandstones, mm to dm scale. Chaotically distributed clasts. Presence of deformation, shear, contortion and injectites, suggesting an unstable environment	Deposited by cohesive muddy or sandy debris flow, from slope collapses

**Table 5.** Core images of facies associations at well B (Neptune Energy internal report)

Facies Associations	Core pictures (Well B)
Clean Sandstones facies association (FA1)	
Transitional Sandstones facies association (FA2)	
Mudstone/siltstone facies associations (FA3)	No image

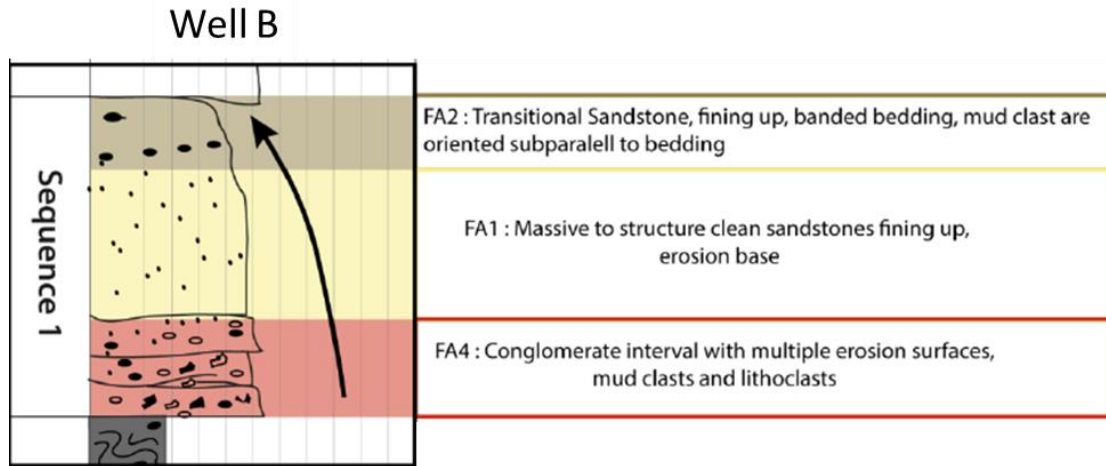


Based on the well data, the structural setting, and the general understanding of the regional geology, Neptune Energy arrived to the following depositional model (Clerc et al., 2018):

- (1) A basal unit shows a mass transport deposit, characterized by a chaotic facies association (FA5) (Tables 4 and 5).
- (2) A middle unit (the lower reservoir) displays 3 sequences following a stacking pattern (conglomerate (FA4) to clean sandstones (FA1) to transitional sandstone (FA2)) at a small scale (meters) (Figure 16). The thick sandstone beds might be deposited from high density turbidity currents and reworking of sediments caused by high-energy

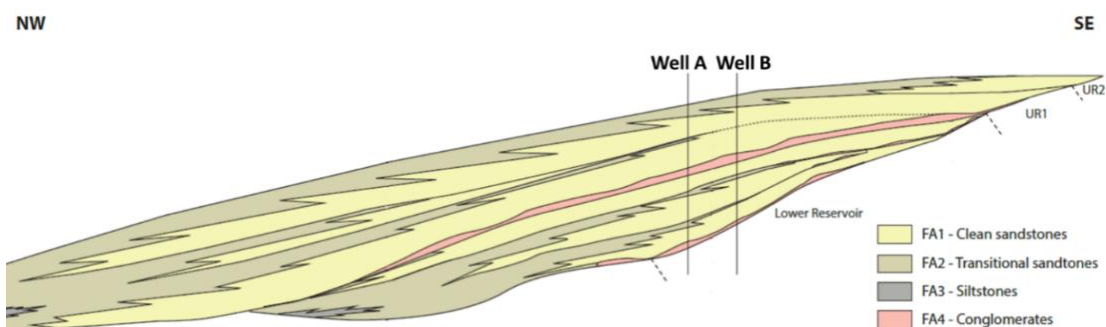
turbulent gravity flows. The transitional sandstones which are related to proximal hybrid beds are restricted to a few samples.

- (3) An upper unit (covering the conglomerate zone and the upper reservoir) illustrates the same general stacking pattern at larger scale (tens of meters) (figure 16).



**Figure 16.** Synthetic sequence of well B (from Neptune Energy).

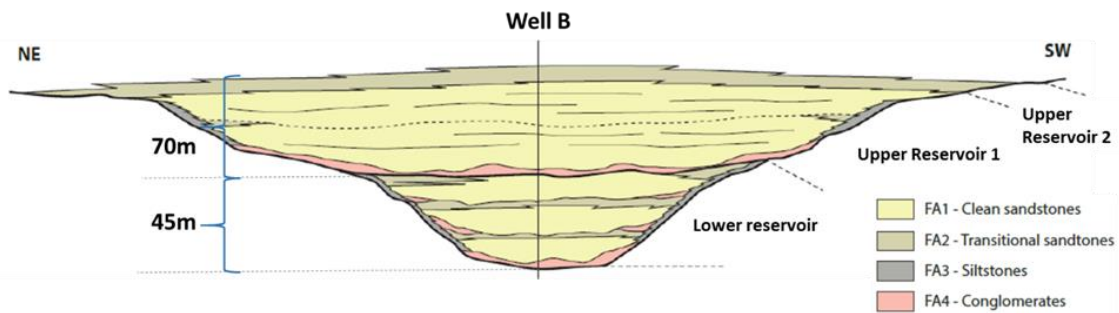
- The conglomeratic interval contains a mixture of heterolithic and carbonaceous clasts, which are interpreted as locally eroded sediments from within and near the canyons head.
- The massive coarse-sand unit probably corresponds to the amalgamation of several turbiditic sequences, which cannot be individually distinguished.
- The transitional sandstones unit: can be interpreted as the result of the backstepping of the system, which might be associated with the overall sea-level rise in the Late Albian. This interval can be considered as hybrid beds recorded by the presence of large reworked clasts (FA2)



**Figure 17.** Synthetic facies association distribution along the depositional fairway along wells A and B (from Neptune Energy).



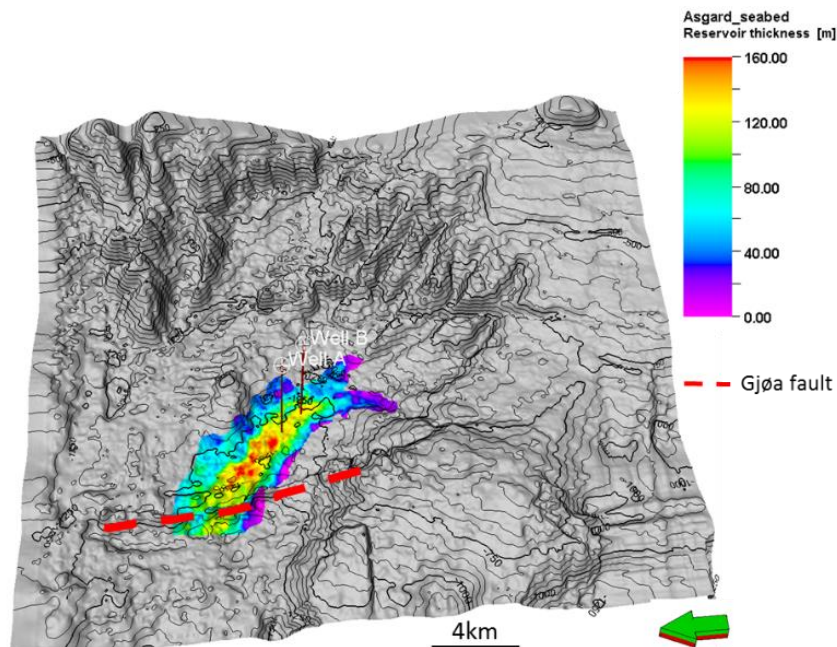
Based on the facies log of well B (figure 15) and the sedimentological background, two synthetic facies association sections, one along the depositional fairway and an other across well B, were sketched to predict the spatial lithology distribution of the reservoir (Figure 17 and 18)



**Figure 18.** Synthetic facies association distribution along the depositional fairway across well B (from Neptune Energy).

### 5.6 Conceptual model

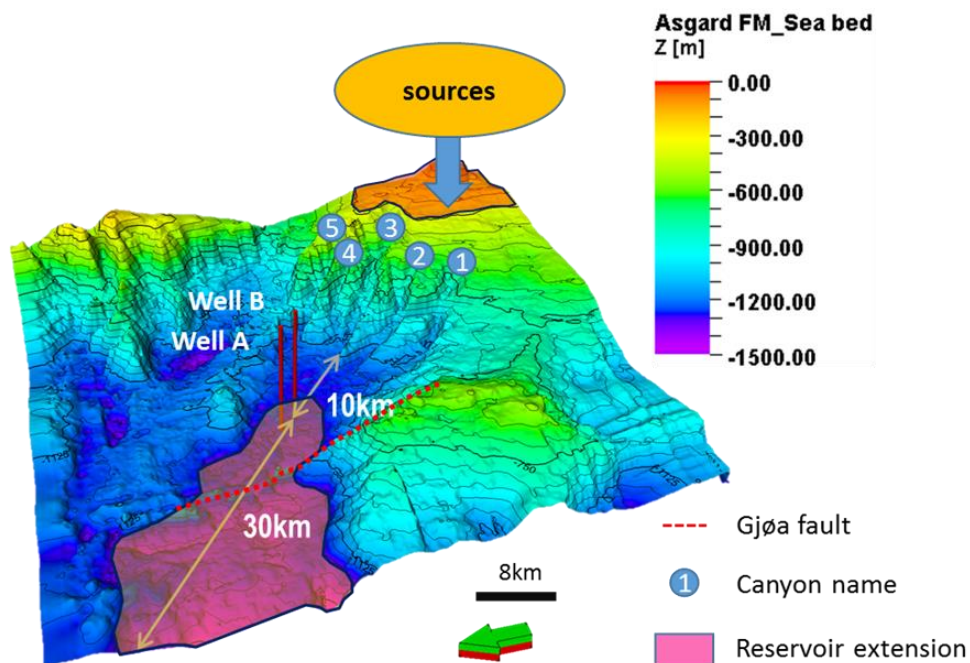
The reservoir thickness attribute was generated from the present-day top and base reservoir map. This attribute was then plotted on the top Åsgard paleo-topography map (Figure 19). This allows viewing the spatial distribution of the reservoir thickness, especially the relative position of the reservoir with respect to the wells. This attribute shows that well A and B are located at the deepest part of the reservoir, which corresponds to the axis zone of the turbidite system.



**Figure 19.** Reservoir thickness attribute displayed in the Åsgard paleo-topography map (Neptune Energy).

Combining the information from seismic spectral decomposition and sedimentological analysis, a conceptual model is summarized by the following key points:

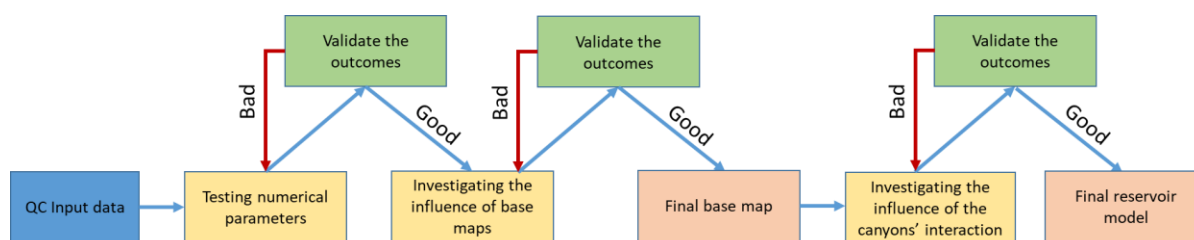
- a. The turbidity flows were generated from canyons 1 and 3 shown in the base topography map (Figure 20).
- b. The well B is 10 km away from canyon 3. Based on the seismic spectral decomposition images (Figure 12), the lower reservoir is constrained by the Gjøa fault in the northwest, while the upper reservoir might extend farther in the NW direction, up to 30 km from the canyon feet (Figure 20)
- c. The reservoir contains two main units:
  - The lower reservoir deposited within a confined area.
  - The upper reservoir deposited in less-confined space and with a sheet-like shape.
  - At well B, the lower reservoir has 45 m thickness, and the upper reservoir has 70 m thickness (Figure 16).
- d. The conglomerate interval marks the boundary between the lower and upper reservoirs. However, this interval is regarded as the transition zone, which is the result of the interaction between two sources originated from canyons 1 and 3.



*Figure 20. A 3D view of the conceptual model (Neptune Energy).*

## 6. Methodology

In general, the modeling procedure consists of four main steps described in Figure 21:



*Figure 21. The workflow that was applied to deliver the possible outcomes from the input data.*

### 6.1 Quality check of the input data

An important input of the model is the Åsgard paleo-topography map (Figure 13). A dip angle attribute of this map (Figure 14) illustrates that the topography at the well locations is quite flat. However, using the top Åsgard palaeobathymetry directly as some limitations:

- The stratigraphic succession in the area indicates that the Sola formation is deposited after the Åsgard Fm and before the Agat Fm. Therefore the topography of the Åsgard Fm does not reflect the exact topography at the time of deposition of the Agat Fm. However, the palaeobathymetry reconstruction could not be performed directly on the top Sola Fm (the seismic horizon was not continuous enough to be implemented in the model). The top Åsgard is the closest approximation that could be assumed.
- The biostratigraphic analysis in the Well A and B also revealed that a significant hiatus is recorded below the Agat reservoir, resulting from the erosion generated by the turbiditic flow. The previous work provided by Neptune has confirmed that the conceptual model where the lower reservoir deposited in a confined basin (see section 5.5). This confinement directly results from the erosion created by the turbiditic flow.

Therefore, the original Åsgard paleo-topography was adjusted before using it as the base of the model. Firstly, the uplift related to the Gjøa fault was removed to create an open basin. Later, the reservoir thickness attribute (Figure 19) was subtracted from the paleo-topography map (Figure 20). This step aimed to create a confined accommodation space in the base map for the lower reservoir, honoring the present-day reservoir thickness and lateral geometry.

Obviously, the manual editing of the base map is subject to uncertainty. Also, the morphology of the base map has a large influence on the distribution of the turbidite system. Hence, two base maps with different degree of smoothness and confinement were created. Using GPM, the

base map that provided the best match of the simulated turbidite geometry with the seismically interpreted turbidite was selected for the subsequent investigation (see section 6.3.1 for a detailed discussion).

## 6.2 Testing numerical parameters

The three processes diffusion, unsteady flows and sediment accumulation, were applied to model the turbidite system in this study. The performance of each process was studied separately before being incorporated into the generic model.

All parameters in these processes can be categorized as either numerical or geological parameters. Numerical parameters allow controlling the model to work stable and deliver meaningful results without artifacts. Some important numerical parameters are cell size, time increment, or fluid element depth.

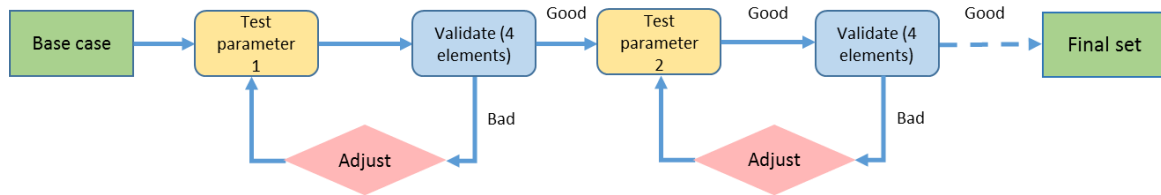
The numerical parameters were selected after several trial – error runs. The final solution was made based on balancing four elements: (1) the running time, (2) the detail of the outcome, (3) the model size and (4) the display performance. The final values used for each parameter, as well as their meaning and constrained factors are listed in the Table 6.

*Table 6. Spatial and temporal parameters of the numerical models.*

<b>Parameters</b>	<b>Meaning</b>	<b>Unit</b>	<b>Values</b>	<b>Constrained by</b>
Cell size	Size of 1 cell	m	200*200	Runtime + model size
Area of simulation	Area of the base map	km	19.6*43.1	Paleo-topography + model size
Time increment	Time step for other processes (except unsteady flow)	year	0.5	Runtime + interaction between processes
Display interval	Time step to display results	year	200	Runtime + display performance

With the parameter values above, the model took 1 hour and deliver 3 GB for one run. Because the display interval was 200 years, GPM summarized the result of all processes happening in

200 years in one layer. Hence, if the system lasted 3000 years, it contained 15 layers in total. However, the simulation performance did not only depend on the numerical parameters, but also relied on the duration time of the processes and the hardware capacity. Figure 22 summarized how the general numerical parameters were chosen. The first parameter was set to a fixed value after being validated for the four elements mentioned above, before moving to the second one and continued until the last parameter.



**Figure 22.** Workflow to verify the general numerical parameters in the GPM model.

The numerical parameters controlling the unsteady flow (turbidity flow) simulation were also determined through trial and error. The purpose of this is to assess the influence of the variation of sediment supply and water velocity over time on the overall outcome. Table 7 lists the values of each parameter and the constraints.

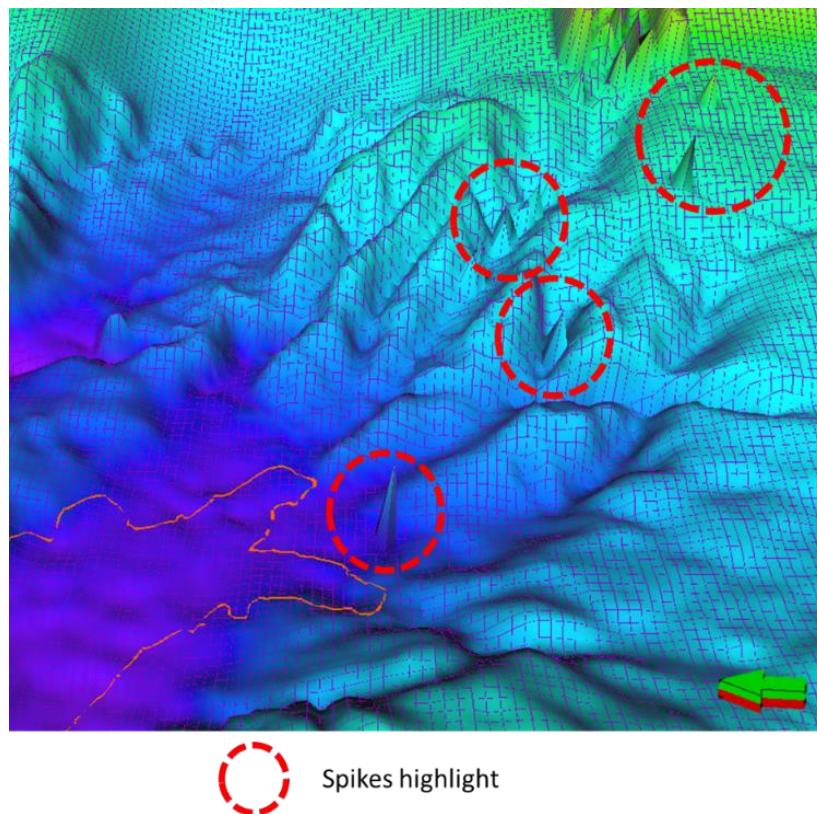
**Table 7.** Values for numerical parameters controlling the unsteady flow

Parameters	Meaning	Unit	Values	Constrained by
Turbiditic event interval	Time between each event	year	20	Number of events + reservoir thickness
Fluid element depth	Control number of particles in the flow	m	0.5	Running time + model accuracy
Duration time	The duration of 1 event	hour	12	Runtime length + interaction between processes
Display time	Display interval of turbidite event	hour	12	Model accuracy

Delta time element	Running time of one turbidite simulation	second	1	Model accuracy + running time
Transport coefficient	Multiplier for sediment transport	none	0.01	Model accuracy

The result of each run was validated based on three conditions:

- No artifact (spikes cells) (Figure 23) which indicate an unstable simulation.
- Total thickness of sediment accumulation at well B is equaled to log data.
- Thin transition sandstones layers in the facies log can be verified in the models.



**Figure 23.** Spike cells as artifacts from the simulation.

The process to verify numerical parameters for the unsteady flow also follows the workflow in Figure 23. It started with the default value for all parameters. Later, each parameter was investigated by changing the value and validated with the three conditions listed above. When one parameter delivered a satisfied outcome, its value was fixed, and another parameter was investigated.

The geological parameters are based on physical laws and determine the performance of the simulation. In this model, these parameters consist of particle sizes, sediment transportability, water velocity, turbidite event interval and sediment accumulation rate at the source. They define the development, implementation and result of geological features. The geological parameters are either taken from other publications or verified via testing to fit the known geometry of the model. The final values of these parameters are discussed in section 6.3.2. The procedure to validate the final input value for geological parameters contains three criteria:

- The conglomerate appears as thin layers at the well B location
- Coarse sand dominates the lower and upper reservoir
- There are transitional sandstone (siltier) layers marking the transgression period which appear in the vertical lithology succession at well B.

The parameters affecting each of these criteria are listed in Table 8:

**Table 8.** *The geological parameters that control each criteria*

Geological criteria	Geological parameters controlling the criteria
The conglomerate appearing as thin layers at the well B location	<ul style="list-style-type: none"> <li>- Conglomerate particle diameter and transportability</li> <li>- Water velocity</li> </ul>
Coarse sand dominating the lower and upper reservoir	<ul style="list-style-type: none"> <li>- Coarse sand accumulation rate</li> <li>- Water velocity</li> </ul>
Transitional sandstone (siltier) layers marking the transgression period appearing in vertical lithology succession at well B	<ul style="list-style-type: none"> <li>- Coarse sand accumulation rate</li> <li>- Silt accumulation rate and silt transportability</li> <li>- Water velocity</li> </ul>

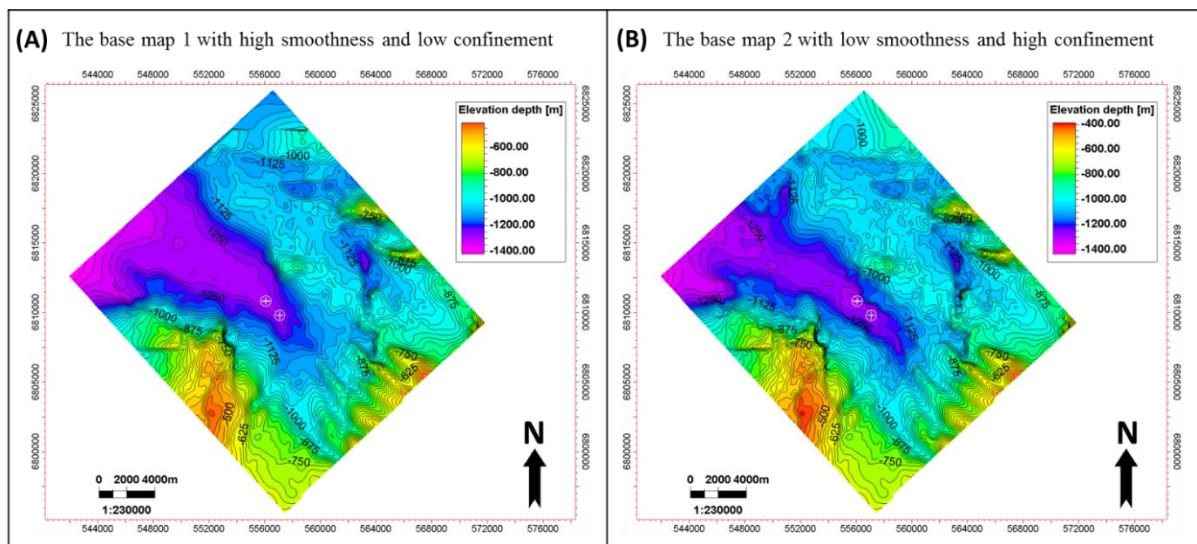
### 6.3 Setting up of the final model

The complete model is a combination of the three processes diffusion, sediment accumulation, and unsteady flow. The thesis focuses on two main questions:

- (1). How does the uncertainty of the base topography affect the outcome of the turbidite system?
- (2). How does the interaction between the two canyons through time influence the lithological distribution and reservoir characteristics?

### 6.3.1 Investigation of the influence of the base maps

To answer the first question, two base maps with different levels of smoothness and confinement were used for the simulation. These maps differ in the reservoir area, where the base map 1 (Figure 24A) is smoother and less confined, compared to the base map 2 (Figure 24B). All other parameters were kept the same for both scenarios. The method to select the final base map is described in section 6.4.1.



**Figure 24.** The two base maps used to investigate the influence of the base map topography: (A) Base map 1 with high smoothness and low confinement, (B) Base map 2 with low smoothness and high confinement.

### 6.3.2 Investigation of the influence of the interaction between 2 canyons

To answer the second question, three main cases were studied with the details discussed below, and summarized in Table 9:

1. Canyon 1 (Figure 20) supplies sediments to the lower reservoir. Canyon 1 gradually reduces the flow and finally stops feeding the reservoir (corresponding to the conglomerate interval at well B). Later, canyon 3 (figure 20) delivers the sediments to the upper reservoir.



2. Canyon 3 (Figure 20) supplied sediments to the lower reservoir. Canyon 3 gradually reduces the flow and stops feeding the reservoir (corresponding to the conglomerate interval at well B). Later, canyon 1 (figure 20) delivers the sediments to the upper reservoir.
3. Both canyons 1 and 3 are active throughout the depositional history of the reservoir.

**Table 9.** Three main cases to investigate the impact of two sources coming from two different canyons

Cases	Description
1	<ul style="list-style-type: none"> <li>• Canyon 1 fed the lower reservoir (early time)</li> <li>• Canyon 3 fed the upper reservoir (later time)</li> </ul>
2	<ul style="list-style-type: none"> <li>• Canyon 3 fed the lower reservoir (early time)</li> <li>• Canyon 1 fed the upper reservoir (later time)</li> </ul>
3	<ul style="list-style-type: none"> <li>• Canyon 1 and 3 were active at the same time and fed both the lower and upper reservoir units</li> </ul>

a. Sediment grain parameters

To clearly observe the interaction of two different sources of sediment, six clastic sediment types with different attributes were assigned to the two canyons, together with the continuous sedimentation of pelagic shale characterizing the deep-water environment. The input settings for all sediments are listed in Table 10, based on the core sample images and parameter testing. The results of test runs were verified by multiple steps, which will be discussed in the calibration section (section 6.4).

**Table 10.** Input parameters of clastic sediments.

Name	Sediment types	Diameter (mm)	Density (g/cm <sup>3</sup> )	Transportability	Erodibility coefficient	Initial porosity (m <sup>3</sup> /m <sup>3</sup> )
Conglo_C3	Conglomerate from canyon 3	21	2.7	0.8	1	0.3

Conglo_C1	Conglomerate from canyon 1	20	2.7	0.82	1	0.3
Sand (coarse)_C3	Coarse sand from canyon 3	1	2.7	3.01	1	0.34
Sand (coarse)_C1	Coarse sand from canyon 1	1.1	2.7	3	1	0.34
Silt_C3	Silt from canyon 3	0.01	2.7	3.2	1	0.4
Silt_C1	Silt from canyon 1	0.015	2.7	3.1	1	0.4
Pelagic Clay	Pelagic Clay	0.0012	2.7	7.6	1	0.55

The parameters related to water velocity and sediment sources are given in Table 11. They are derived from the model based on trial and error. The workflow defining the parameter values will be described in section 6.4.2. These final parameter values were set consistently for all the explored cases.

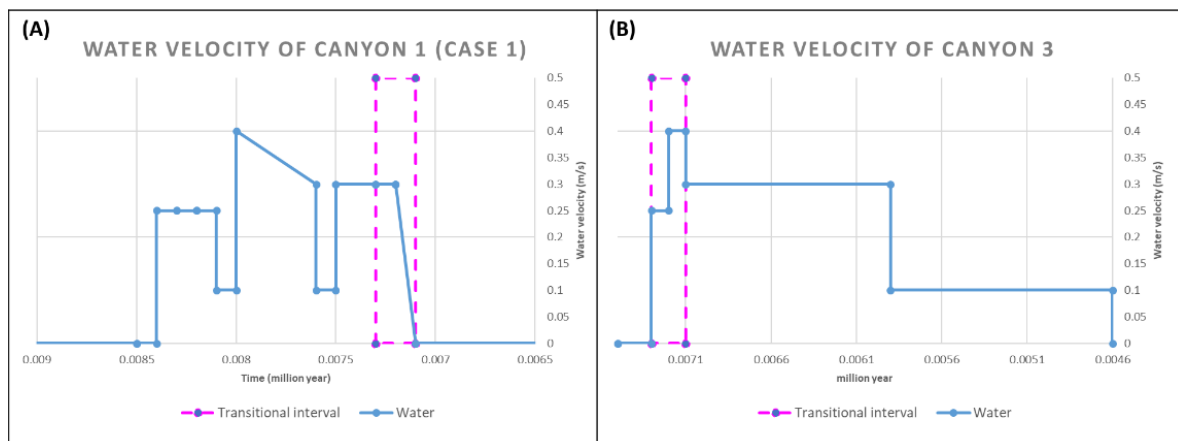
**Table 11.** The water velocity and sediment accumulation rate at two sources related to the two canyons

Sediment types	Canyon 1			Canyon 3			Pelagic shale
	Conglo C1	Coarse sand C1	Silt C1	Conglo C3	Coarse sand C3	Silt C3	
Accumulation rate (m <sup>3</sup> /y)	1.8E+05	5.6E+05	5.6E+05	1.0E+05	8.1E+05	6.9E+05	2.9E+05
Source area (m <sup>2</sup> )	8.7E+06	1.5E+07	1.5E+07	6.7E+06	2.2E+07	1.8E+07	8.6E+08
Sediment rate at 1 cell (mm/y)	20.08	36.60	36.60	15.39	36.17	37.90	0.34
Water supply area (m <sup>2</sup> )	1.0E+07			2.3E+07			

From the core images at well B (Table 4), the conglomerate interval consists of a mixture of pebbles (diameter  $\approx 10$  mm), large shale clasts (diameter  $\approx 50$  mm), coarse sands (diameter  $\approx 1$  mm), and silt (diameter  $\approx 0.01$  mm). The transitional intervals are mixtures between coarse sands (diameter  $\approx 1$  mm) and silt (diameter  $\approx 0.01$  mm). In the clean sandstone interval, the coarse sand (diameter  $\approx 1$  mm) dominates. The cutoff value for each facies is specified in Tables 12 and 13. They were applied later to convert the GPM outcomes into facies properties, and then used as one condition in the calibration step (see section 6.4).

b. Water velocity at the sources

Regarding the water source, the water supply area is multiplied by the water velocity at each cell of the supply area to give the total amount of water introduced into the model per second. For example, if the water supply area of canyon 1 is  $1.0E+07$  m<sup>2</sup>, and the water velocity at one supply cell is 0.8 m/s, the model will receive  $8E+06$  m<sup>3</sup> of water per second.



**Figure 25.** The variation of water velocity at canyon 1 (A) and canyon 3 (B) (case 1)

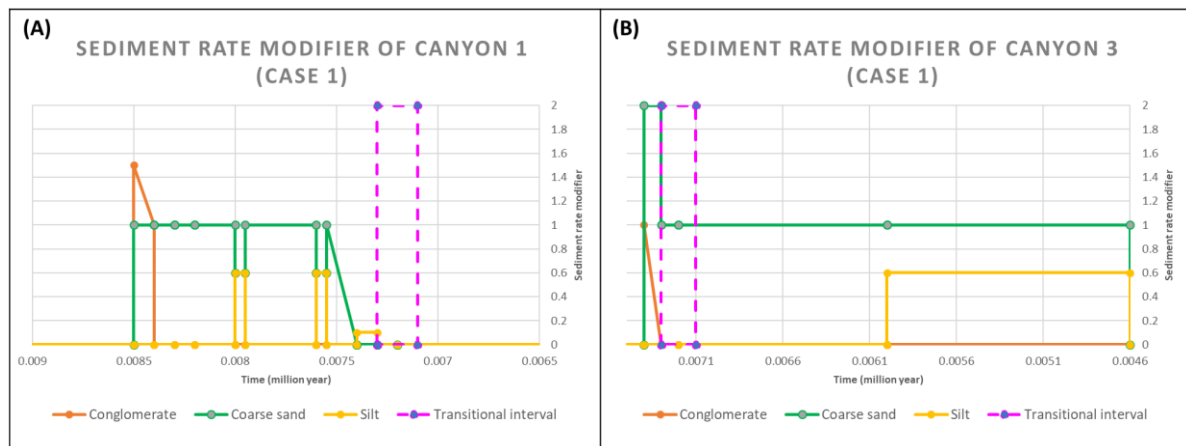
In case 1, the canyon 1 fed the lower reservoir, while the upper reservoir was filled by sediments from canyon 3 (Table 9). Therefore, the water was set to start from canyon 1 first, then gradually reduced to 0 m/s in the transition interval (Figure 25A), while the water from canyon 3 started flowing at the transition interval and continued until the end of the simulation (figure 25B). In canyon 1, the high water velocity (0.25 – 0.4 m/s) corresponds to the coarse sand intervals and the low water velocity (0.1 m/s) corresponds to the transition sandstone layers (Figure 25A). Similarly, the water at canyon 3 started with 0.3 m/s and reach 0.4 m/s, matching the conglomerate intervals, then it was reduced to 0.3 m/s corresponding to the coarse

sand intervals and finally decreased to 0.1 m/s in agreement with the transitional sandstones (Figure 25B).

The water velocity graphs of case 2 and 3 are displayed in the Appendix.

c. Sediment accumulation rate at the sources

For the sediment input, the sediment rate at one cell is adjusted by the “sediment rate modifier” parameter, which varies with time. This parameter defines how fast one type of sediment can accumulate at one cell. Regarding one cell, this value is multiplied with the cell area (m<sup>2</sup>) and the sediment accumulation rate (mm/year) to deliver the total volume of sediment accumulation at that cell per year.



**Figure 26.** The variation of sediment rate modifier at canyon 1 (A) and canyon 3 (B) (case 1)

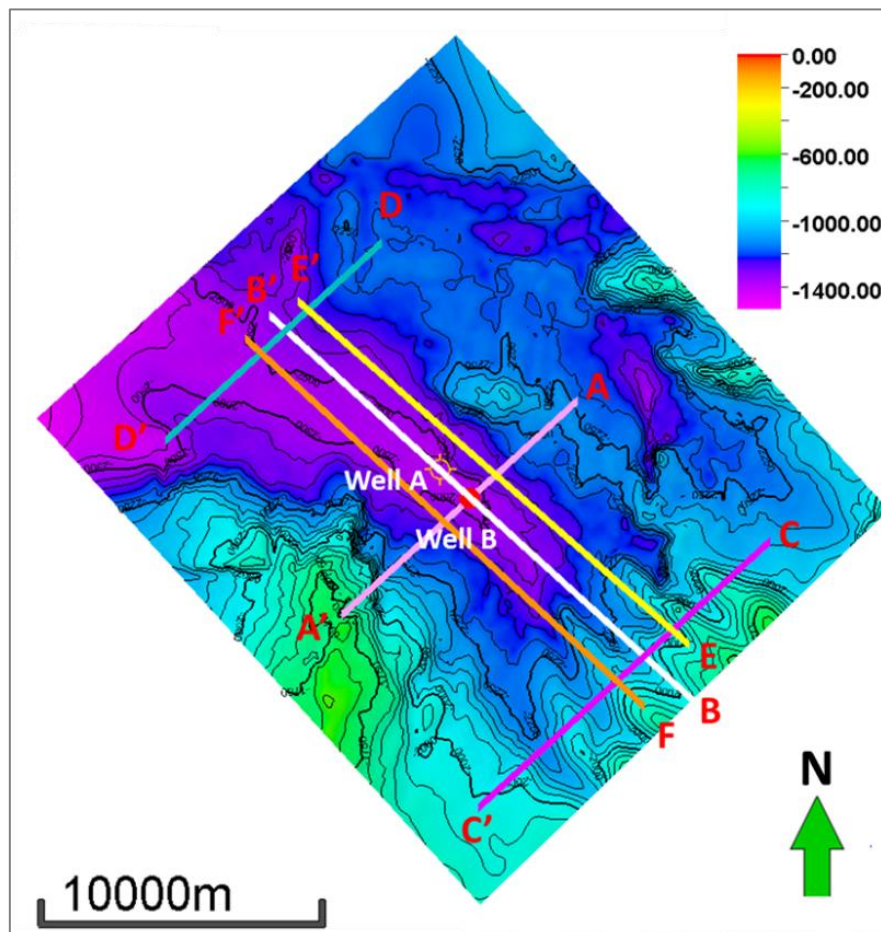
However, this does not mean that all the accumulated sediments will join the turbidite. The amount of sediment particles involved in the flow depends on the erosion process, which is controlled by the water volume, water velocity at the source, sediment erodibility, sediment transportability and grain sizes.

The variation of sediment rate modifier of case 1 is shown in Figure 26 and the graphs related to the other two cases are shown in the Appendix. In case 1, the canyon 1 fed the lower reservoir, while the upper reservoir was filled by sediments from canyon 3 (Table 8). Therefore, the sediment rate modifier was set to start from canyon 1 first, then reduced to 0 m/s in the transition interval (figure 26A), while the sediments at canyon 3 started accumulating before the water flowed in the transitional interval and continued until the end (Figure 26B). In canyon 1, the conglomerate was set to start growing fast (1.4) at the beginning of the system and stopped quickly within 5 events (100 years), creating enough volume within the canyon area to fit the scenario of local source. The coarse sand rate was set as constant value (1) to fit the

coarse sand intervals and it was reduced to 0.6 corresponding to transitional sandstones layers. The silt was set to 0 most of the time, except for two periods matching with transitional sandstones (0.6). In canyon 3, the conglomerate and coarse sand were set to accumulate in the source before the turbidity flows started. While the conglomerate stopped growing after 100 years, the coarse sand kept a constant rate (1) until the end of the simulation. The silt started accumulating 1000 years after the simulation started, corresponding to the transitional sandstone in the top reservoir.

#### 6.4 Calibration of the final model

Since well A does not have core data and the distance from well A to well B is close (1.5 km) in comparison to the reservoir extension (30 km), and since both wells are located in the axis of the basin, well B was chosen as the reference to control the outputs of the simulations.



**Figure 27.** 2D view of the topography map with the navigation of several cross sections, which were used to control the outcome of the model.

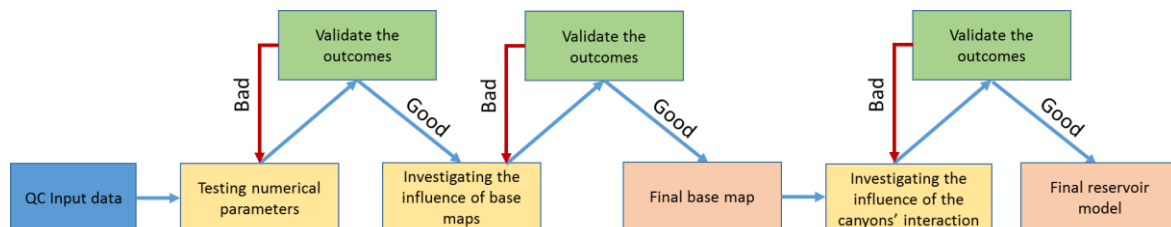
#### 6.4.1 Calibrating the influence of the base maps

The sections crossing well B (A-A' and B-B') (Figure 27) showing the vertical distribution of lithology mixture and the conglomerate fraction were used to compare the outcome of each base map.

Based on these sections, the final base map was chosen using three criteria: (1) there are thin conglomerate layers in the lithology succession of well B; (2) the fraction of conglomerate grains in conglomerate units was limited to 20%; (3) the thickness of sediment layers in the basin flanks was lower than the vertical seismic resolution.

#### 6.4.2 Calibration of the influence of the interaction between 2 canyons

Qualitatively, two sections crossing the position of well B (A-A') and along the axis of the basin (B-B') (Figure 27) were used to show the vertical distribution of the lithology mixture as well as the conglomerate fraction. Moreover, 3D map views of two intervals (top of the lower reservoir and top of the upper reservoir) were utilized to illustrate the lateral lithology distribution at two different stages for the three cases. The workflow in Figure 28 was applied to calibrate each run and deliver the outcome of each case.



**Figure 28.** Workflow to calibrate and adjust the geological parameters for each case to investigate the influence of canyons interaction.

The key idea is adjusting the timing and values of water velocity and sediment accumulation rates to fit the vertical succession at well B. The procedure started with the lower reservoir. Firstly, the output must match the thin conglomerate layers at the bottom of the reservoir. Then, it must fit the two transitional sandstone intervals in the lower reservoir. After that, it should stop depositing at the beginning of the conglomerate unit, which is the reference between the lower and upper reservoir. Besides this, the conglomerate fraction in the bottom of the lower reservoir should be around 15-20%, while the fraction of silt in transitional sandstones should

be around 15%. The time and geological parameter values were fixed for the lower reservoir, before adjusting these parameters for the upper reservoir.

Similarly, the upper reservoir started with matching the conglomerate interval at the bottom of the upper reservoir. Then, the transitional sandstones should match the facies log in the top of the upper reservoir. The conglomerate fraction in the layers had to be around 15-20%, while the fraction of silt in transitional sandstones should be around 15%. The whole system should stop before the hemi-pelagic unit deposited (corresponding to the hemi-pelagic shale interval in well B).

To compare the three cases, the GPM models were converted to 3D grid properties containing the fraction properties for each sediment type. Later, the facies properties were created using the combination of cutoff values of all sediment proportions from the GPM model. The cutoff values are described in Table 12 (case 1 and 3) and Table 13 (case 2). The sediment types columns shaded in green belong to canyon 1, while those shaded in red belong to canyon 3.

**Table 12.** Cutoff values of sediment fractions for each facies in Case 1 and 3.

3D grid properties			Sediment types in GPM model						
Code	Facies name	Color	Conglo C1	Coarse sand C1	Silt C1	Conglo C3	Coarse sand C3	Silt C3	Pelagic clay
0	Background		Cells that don't satisfy the category below						
1	Clean sst C3					<0.1	>0.65	<0.15	
2	Transitional C3					<0.1	<0.65	>0.15	
3	Conglomerate		>0.1			>0.1			
4	Mudstone/pelagic								>0.8
5	Clean sst C1		<0.1	>0.65	<0.15				
6	Transitional sst C1		<0.1	<0.65	>0.15				

**Table 13.** Cutoff values of sediment fractions for each facies in Case 2.

3D grid properties			Sediment types in GPM model						
Code	Name	Color	Conglo C1	Coarse sand C1	Silt C1	Conglo C3	Coarse sand C3	Silt C3	Pelagic clay
0	Background		Cells that don't satisfy the category below						
1	Clean sst C1		<0.1	>0.65	<0.15				
2	Transitional C1		<0.1	<0.65	>0.15				
3	Conglomerate		>0.1			>0.1			
4	Mudstone/pelagic								>0.8
5	Clean sst C3					<0.1	>0.65	<0.15	
6	Transitional sst C3					<0.1	<0.65	>0.15	

Additionally, the Vshale and Net-to-Gross properties were generated from the fraction of sediments with the cutoff values in Table 14 (for Vshale) and Table 15 (for Net-to-Gross).

**Table 14.** Vshale cutoff values for all sediment types.

Sediment names	Sediment types	Vshale cutoff values
Conglo_C1	Conglomerates from canyon 1	1
Coarse sand_C1	Coarse sands from canyon 1	0
Silt_C1	Silts from canyon 1	0.5
Conglo_C3	Conglomerates from canyon 3	1
Coarse sand_C3	Coarse sands from canyon 3	0
Silt_C3	Silts from canyon 3	0.5
Pelagic clay	Pelagic shale	1

**Table 15.** The Net-to-Gross cutoff values for all sediment types.

Sediment names	Sediment types	Net-to-Gross cutoff values
Conglo_C1	Conglomerates from canyon 1	0
Coarse sand_C1	Coarse sands from canyon 1	1
Silt_C1	Silts from canyon 1	0.3
Conglo_C3	Conglomerates from canyon 3	0
Coarse sand_C3	Coarse sands from canyon 3	1
Silt_C3	Silts from canyon 3	0.3
Pelagic clay	Pelagic shale	0

To compare the three cases, the facies and synthetic shale volume properties were applied to quantitatively measure the matching level between the GPM outcomes and well data. Firstly, the facies and Vshale logs were created from these properties of the 3D grid, with a sampling rate of 0.5 m. Later, the simulated facies log was compared with the actual facies log by setting up a Boolean log. If the simulated facies log matched the actual facies log, the Boolean was set as “True” (value =1). If the simulated facies log did not match the original log, the Boolean was set to “False” (value =0). This comparison was applied for all facies codes, except the conglomerate. Wherever the actual log was conglomerate, the Boolean log was set as “True” (value=1).



Regarding the shale volume, the absolute difference between the actual Vshale log and the simulated Vshale log from the 3D grid was generated. Later, this value was compared with the actual Vshale log. If the difference was equal or larger than 100% of the actual Vshale, the Boolean log was set to False (0). If the difference was less than 100% of the actual Vshale, the Boolean log was set to True (1). At the end, the number of “True” samples in the two Boolean logs were counted to give the matching level between the model and well logs.

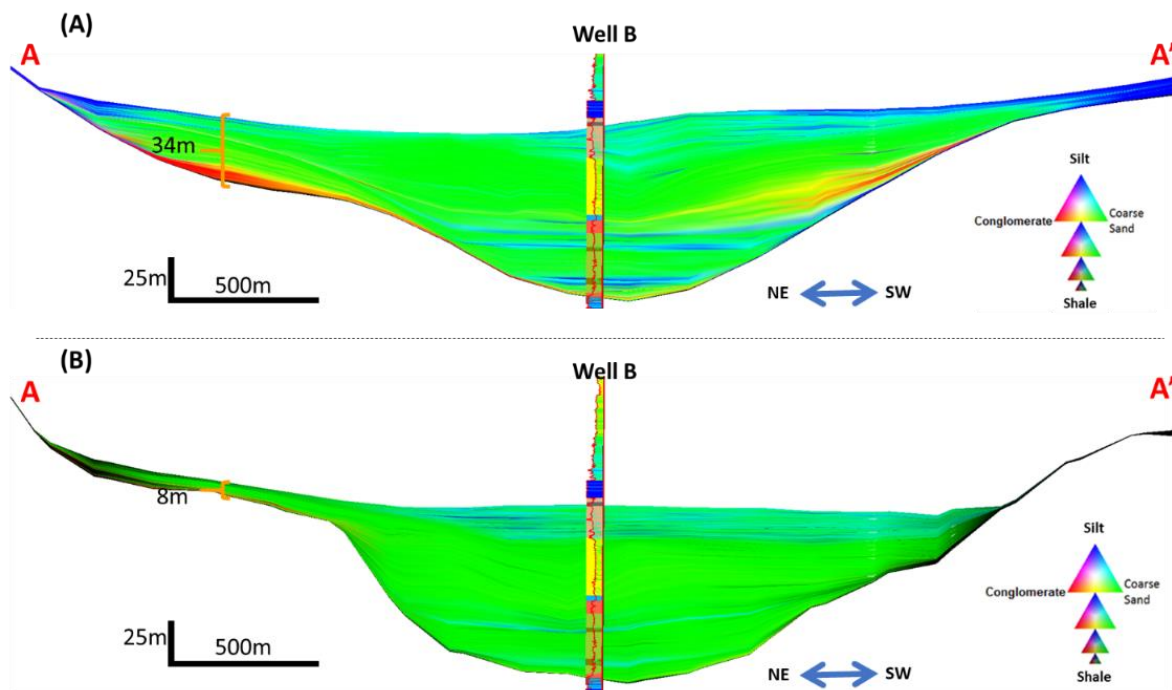
## 7. Observation

### 7.1 GPM output

#### 7.1.1 Influence of the base maps on the turbidite geometry

The results of the two models using the two base maps shown in Figure 24A and 24B are evaluated via the cross-section A-A’ passing well B (Figure 27), displaying the lithology mixture (Figure 29) and conglomerate fraction (Figure 30).

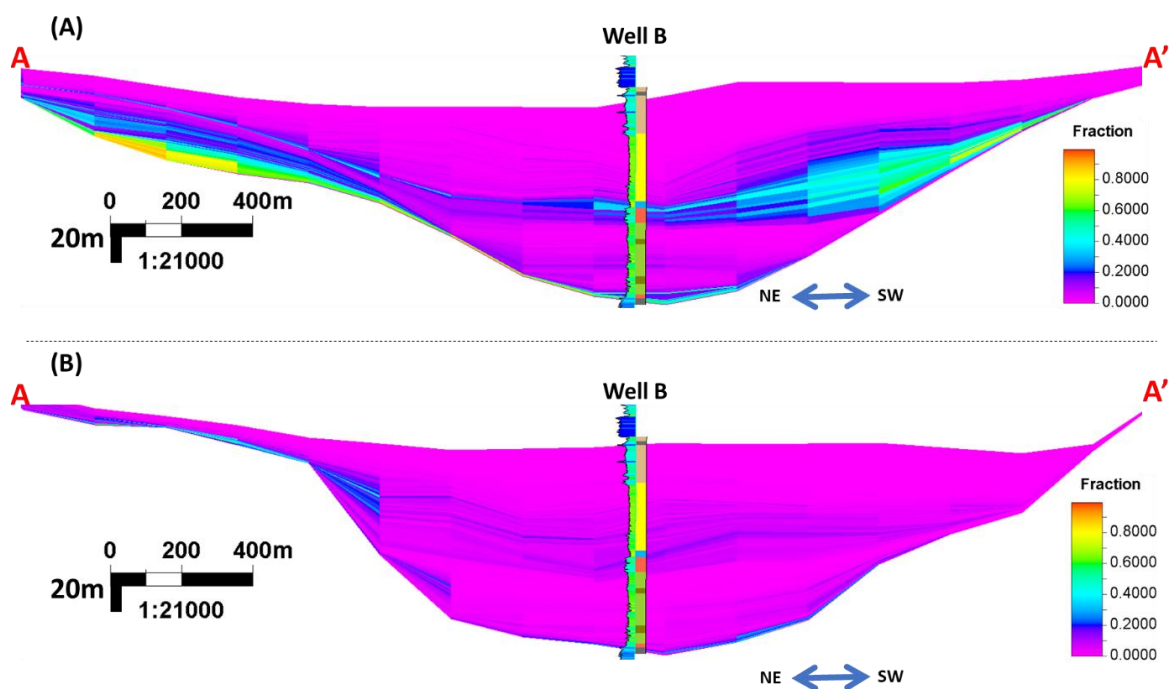
Figure 29A and 30A display the products of the more open base map 1 (Figure 24A). They show quite thick sediment layers deposited at the eastern flank of the basin, with a thickness up to 35 m. Also, the conglomerates are displayed as red layers at the base of the model in Figure 29A and as a high fraction of conglomerates at the base of the model in Figure 30A. The material on the eastern flank corresponds to a thickness above seismic resolution, and



**Figure 29.** Cross section A-A’ at well B showing lithology mixture properties of two models using two base maps: (A) the result of the more opened base map 1 (figure 24A); (B) the result of the more confined base map 2 (figure 24B). Navigation of cross section A-A’ displayed in figure 27.

should be revealed in seismic observations. However, the seismic picking of the reservoir extent does not reflect such the same thickness.

Figure 29B and 30B show the outcome based on the confined base map (figure 24B). The sediment layers are thinner at the eastern flank (8 m), while the proportion of conglomerate grains in conglomerate units is around 15-20 percent (figure 30B) and difficult to observe in Figure 29B due to the dominant green color from the coarse sand. The low conglomerate fraction is compatible with the observations in the core data. Also, the thickness of layers in the eastern flank (8 m) is lower than seismic resolution and matches with seismic observation.



**Figure 30.** Cross section A-A' at well B showing conglomerate fraction properties of two models using two base maps: (A) the result of the more opened base map 1 (figure 24A); (B) the result of the more confined base map 2 (figure 24B). Navigation of cross section A-A' displayed in figure 27.

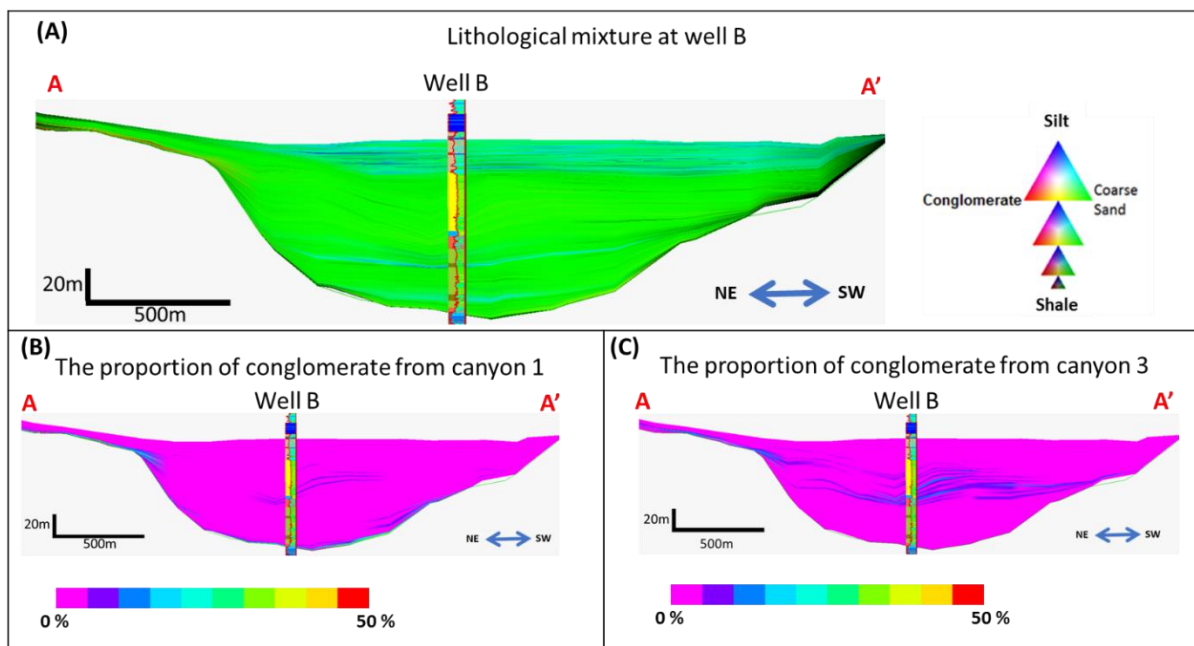
The base map selected for the study is based on the comparison of the simulated turbidite, its geometry and sediment fractions with the core data and seismic interpretation, which is summarized in Table 16. Using these criteria, the confined basemap (Figure 24B) was chosen as input for the next simulations to investigate the impact of the interaction between the two canyons. The confined topography is the only model in which both geometry of the reservoir and the lithology at well location can be respected.

**Table 16.** Base maps selection criteria

Criteria	Open base map 1	Confined base map 2
Thin layer at the eastern flank (lower than seismic resolution)	Do not match	Match
Thin conglomerate layers in well B	Do not match	Match
Low number of conglomerates in the conglomerate units	Do not match	Match

### 7.1.2 Investigating the influence of the interaction between the 2 canyons

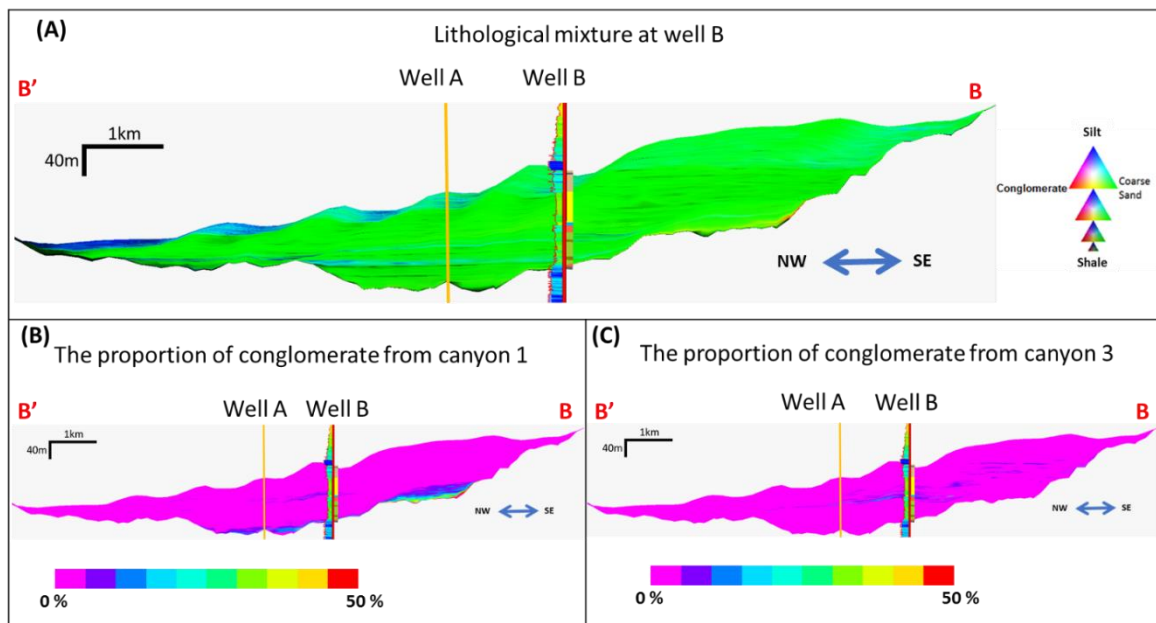
- a. **Case 1:** the lower reservoir was fed by canyon 1, the upper reservoir was fed by canyon 3, and both canyons were active during a short transition time.



**Figure 31.** The result of case 1 shown in the section crossing well B (line A-A' in Figure 27) with three properties: (A) the lithological mixture, (B) the proportion of conglomerate coming from canyon 1, (C) the proportion of conglomerate coming from canyon 3

From the cross-section at well B (A-A') (Figure 31A), coarse sands dominate most of the reservoir (green color). In the transitional sandstone intervals, there is a more balanced combination of coarse sand (green) and silt (dark blue), characterized by light blue layers (figure 31A). Conglomerates from canyon 1 settled mainly at the bottom of the model (Figure 31B), while the distribution of the conglomerates from canyon 3 matches the conglomerate

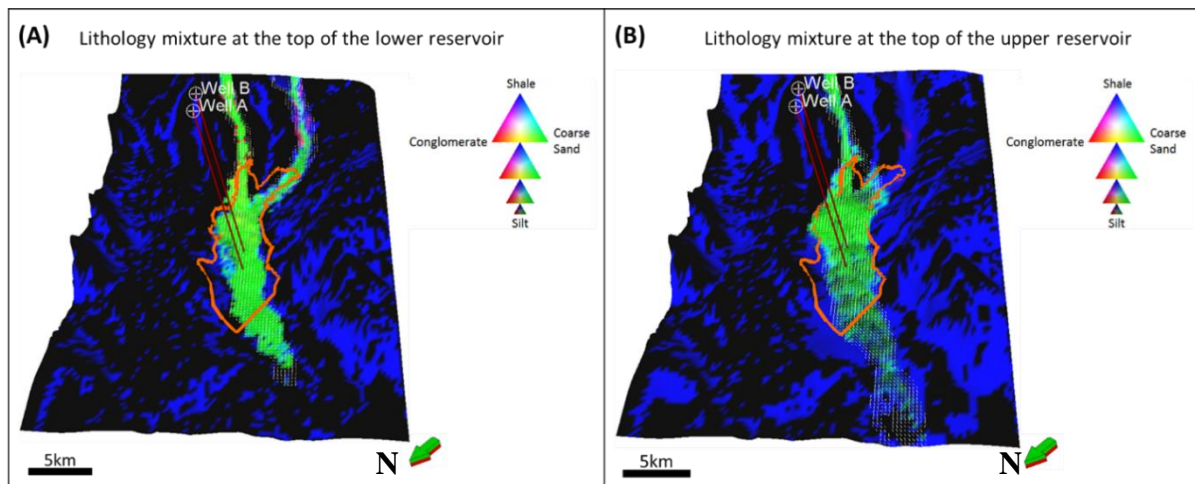
unit at the well B facies log (Figure 31C). However, since the fraction of conglomerates are much less than those of the other sediment types (maximum 20% in one cell), it is difficult to observe these layers from the lithology mixture (Figure 31A) although they can be identified clearly in the proportion of conglomerate attributes (Figure 31B and 31C). The conglomerates of this unit mainly came from canyon 3 and were distributed sparsely. The conglomerates from canyon 1 are also present in a few thin layers. However, they are much less than the amount coming from canyon 3.



**Figure 32.** The result of case 1 shown in the section along the basin axis (line B-B' in Figure 27) with three properties: (A) the lithological mixture, (B) the proportion of conglomerate coming from canyon 1, (C) the proportion of conglomerate coming from canyon 3

In the section along the basin axis, the reservoir becomes thinner away from the canyon (Figure 32). A transgression trend is observed in the lithology mixture attribute (Figure 32A) corresponding to the transitional sandstone interval of the top reservoir. In Figure 31B, the conglomerates from canyon 1 settle mainly at the bottom of the reservoir as a continuous layer. This layer gets thinner away from the canyons to the northwest, reducing the proportion of conglomerates, and finally stopping around 1 km NW of well A. Between the lower and upper reservoir, there are a few small, thin layers containing 10% localized conglomerates from canyon 1 (Figure 32B). These may suggest that these conglomerates came from the rework of the flank of the reservoir. In Figure 32C, the conglomerates from canyon 3 are dispersed in the upper reservoir, mainly in the transition interval between the two reservoir units.

The 3D map of the top of the lower reservoir (Figure 33A) reveals a mixture of coarse sands (green) coming from the two canyons. These sandstones are laterally constrained within the reservoir boundary interpreted from seismic (orange polygon in Figure 33A). In the northwest direction, the lower reservoir reaches a little further out of the boundary polygon (Figure 33A). However, the thickness of this part is too thin to be able to be identified in seismic (Figure 32A).



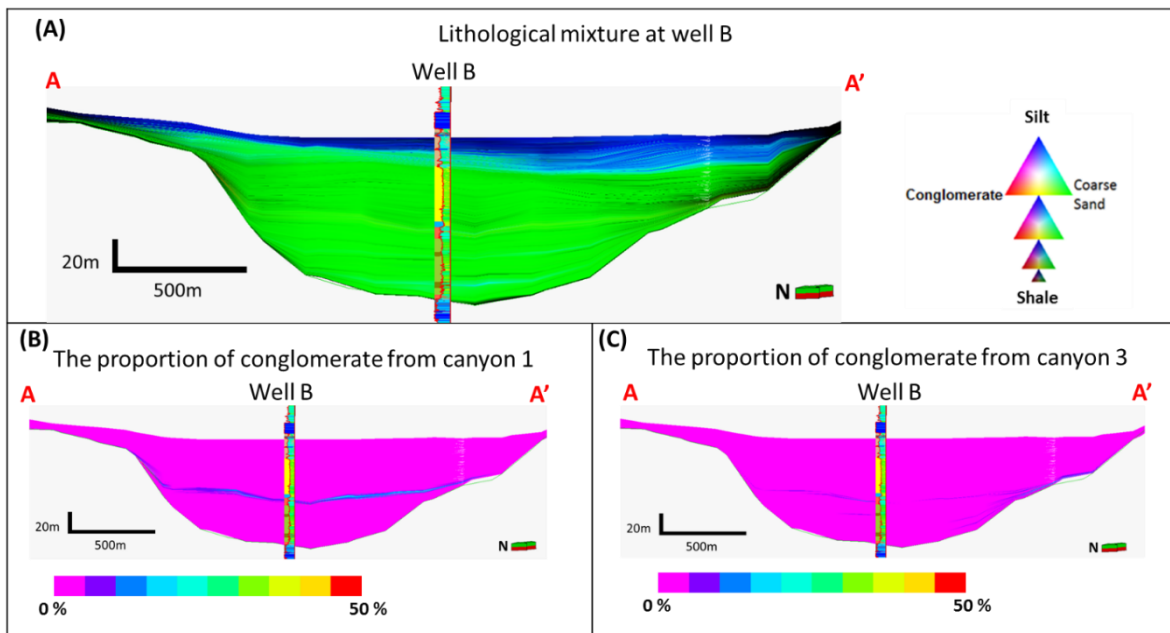
**Figure 33.** 3D view of lithology distribution of case 1: (A) the top of the lower reservoir, (B) the top of the upper reservoir

At the top of the upper reservoir, the silt proportion increases from proximal to distal, corresponding to a black color. The pelagic shale is set as blue color to highlight the topography. Considering the two flanks of the reservoir, the upper reservoir allotted within the reservoir boundary (Figure 33B) and were laterally more opened than the lower reservoir. The top of the upper reservoir reached further to the northwest than the lower reservoir, but that part contained much more silt.

- b. **Case 2:** the lower reservoir was fed by sediment from canyon 3, the upper reservoir was fed by canyon 1, and both canyons were active in a short transition time.

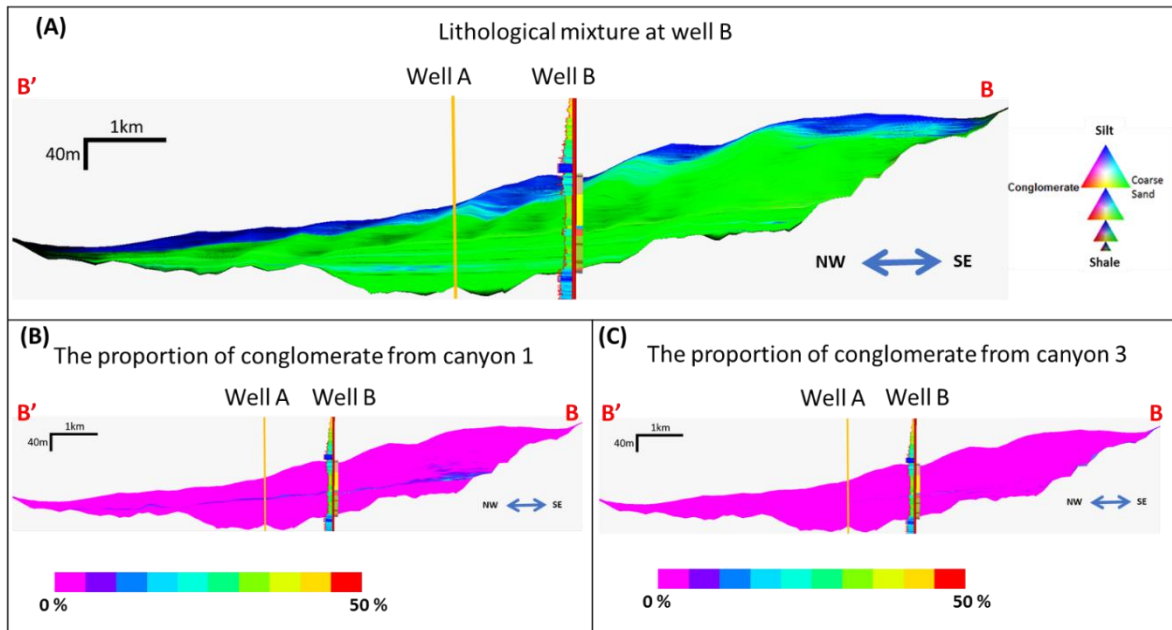
From the cross-section at well B (A-A'), coarse sands dominate most of the reservoir (green color) (Figure 34A). In the transitional sandstone intervals of the upper reservoir, the silts (dark blue) fraction increases (darker blue layers) (Figure 34A) compared to case 1 (light blue layers) (Figure 31A). Very thin layers containing 10% of conglomerate from canyon 3 allocated at the

bottom of the model (Figure 35C). Conglomerates from canyon 3 can also be seen in a few layers in the lower reservoir, but their proportion is low. The distribution of the conglomerates from canyon 1 matches the conglomerate unit at the well B facies log (Figure 34B). The conglomerates are deposited in a more homogenous manner than in case 1, and they laterally separate the reservoir into two different units (Figure 34B).



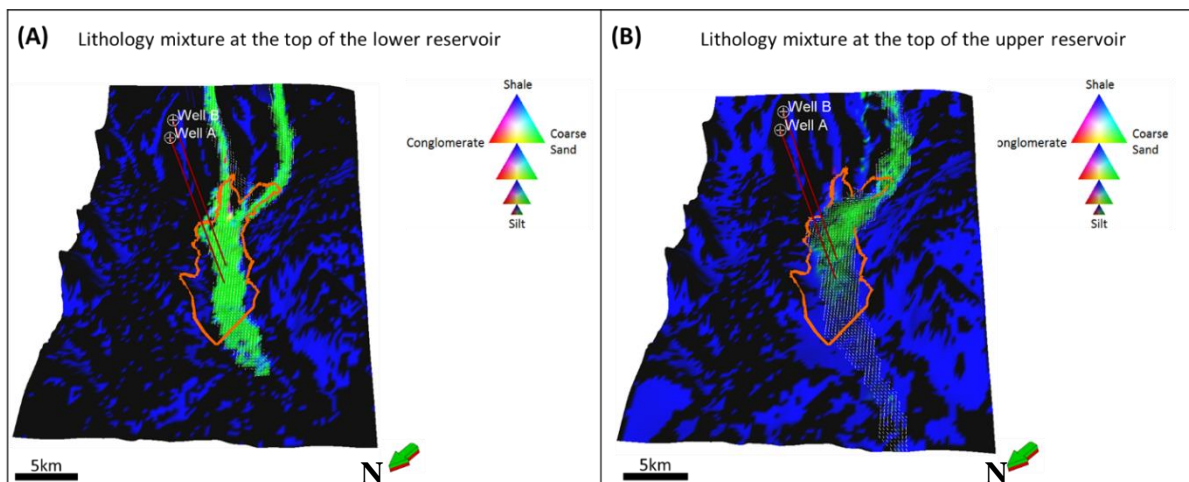
**Figure 34.** The result of case 2 in the cross section at well B (A-A') with three properties: (A) the lithological mixture, (B) the proportion of conglomerate coming from canyon 1, (C) the proportion of conglomerate coming from canyon 3

In section B-B' along the basin axis, the reservoir becomes thinner away from the canyon (Figure 35). There is a similar transgression trend observed in the lithology mixture attribute (Figure 35A) corresponding to the transitional sandstone interval of the top reservoir. However, the silt fraction in this interval is larger than in case 1 (darker blue) and is high even in the proximal part. In Figure 35B, the conglomerates from canyon 1 settled in a continuous layer in the middle of the reservoir (around 20% fraction), separating the whole field into two intervals. This layer of conglomerates gets thinner away from the canyons. In Figure 32C, the conglomerates from canyon 3 dispersed in the lower reservoir in extremely thin layers with less than 10% conglomerates proportion.



**Figure 35.** Result of case 2 in the cross section B-B' along the basin axis location with three properties: (A) the lithological mixture, (B) the proportion of conglomerate coming from canyon 1, (C) the proportion of conglomerate coming from canyon 3. Navigation of cross section B-B' displayed in figure 27.

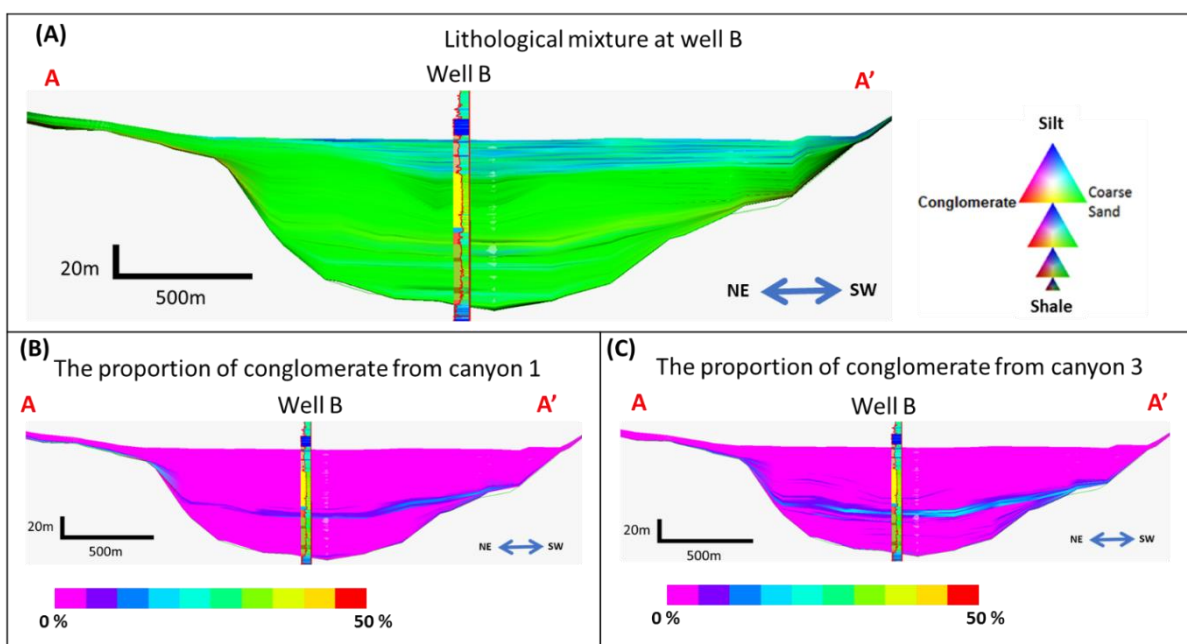
The 3D map of the top of the lower reservoir (Figure 36A) shows a similar outcome to case 1 at the end of the lower reservoir, where there is a mixture of coarse sands coming from the two canyons. These sandstones are laterally constrained within the reservoir boundary observed from seismic (orange polygon). In the northwest direction, the lower reservoir also develops out of the boundary polygon (Figure 36A). The thickness of this part is lower than seismic resolution (Figure 35A). Figure 36B shows that in case 2, silt (black) dominated the majority of the top of the upper reservoir compared to case 1 (Figure 33B).



**Figure 36.** 3D view of lithology distribution of case 2: (A) the top of lower reservoir, (B) the top of upper reservoir

c. **Case 3:** both canyons (1 and 3) were active throughout the whole simulation.

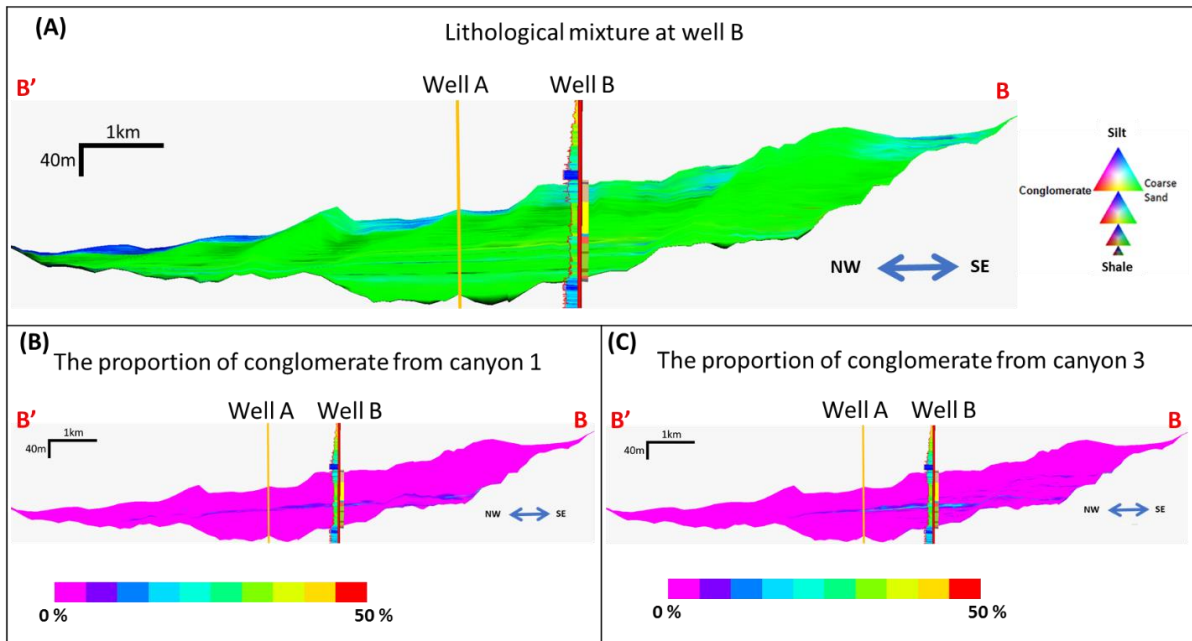
From the cross-section (A-A') at well B, coarse sands dominate most of the reservoir (green color) (Figure 37A). In the transitional sandstone intervals of the upper reservoir, the silts (blue) fraction balanced the coarse sands fraction, resulting in light blue layers (Figure 37A). Conglomerates from both canyon 1 and canyon 3 allocated similarly in the bottom of the lower reservoir and in the conglomerate interval between the lower and upper reservoirs. The conglomerates from canyon 1 formed a modest amount in the lower reservoir, and smaller proportion in the middle interval, compared to the conglomerate from canyon 3.



**Figure 37.** Result of case 3 in the cross section A-A' at well B location with three properties: (A) the lithological mixture, (B) the proportion of conglomerate coming from canyon 1, (C) the proportion of conglomerate coming from canyon 3. Navigation of cross section A-A' displayed in figure 27.

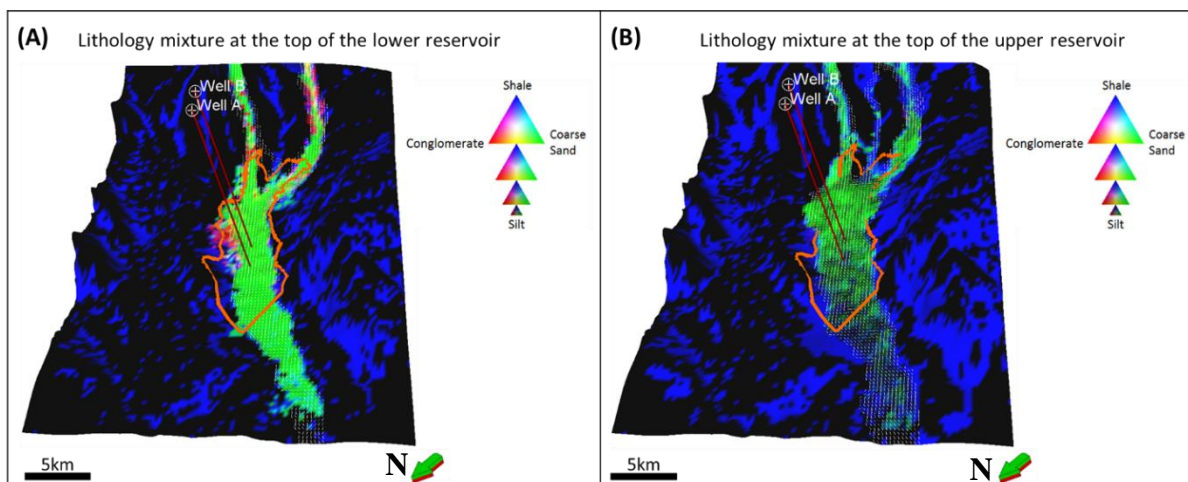
In the section B-B' along the basin axis, the reservoir becomes thinner away from the canyon (Figure 38). A transgression trend is observed in the lithology mixture attribute (Figure 38A) corresponding to the transitional sandstone interval (light blue) of the top reservoir. In case 3, the amount of coarse sands and conglomerates in distal parts are larger than in cases 1 and 2.





**Figure 38.** The result of case 3 in the cross section along the basin axis (B-B') with three properties: (A) the lithological mixture, (B) the proportion of conglomerate coming from canyon 1, (C) the proportion of conglomerate coming from canyon 3

The 3D map of the top of the lower reservoir (Figure 39A) shows that the lower reservoir is laterally constrained within the reservoir boundary observed from seismic (orange polygon), but it extends much further out of the boundary polygon in the northwest direction (figure 39A). The thickness of this part is also quite high, around 30-60 m (Figure 37A). In addition, Figure 39B shows that the upper reservoir also extends out of the reservoir boundary.

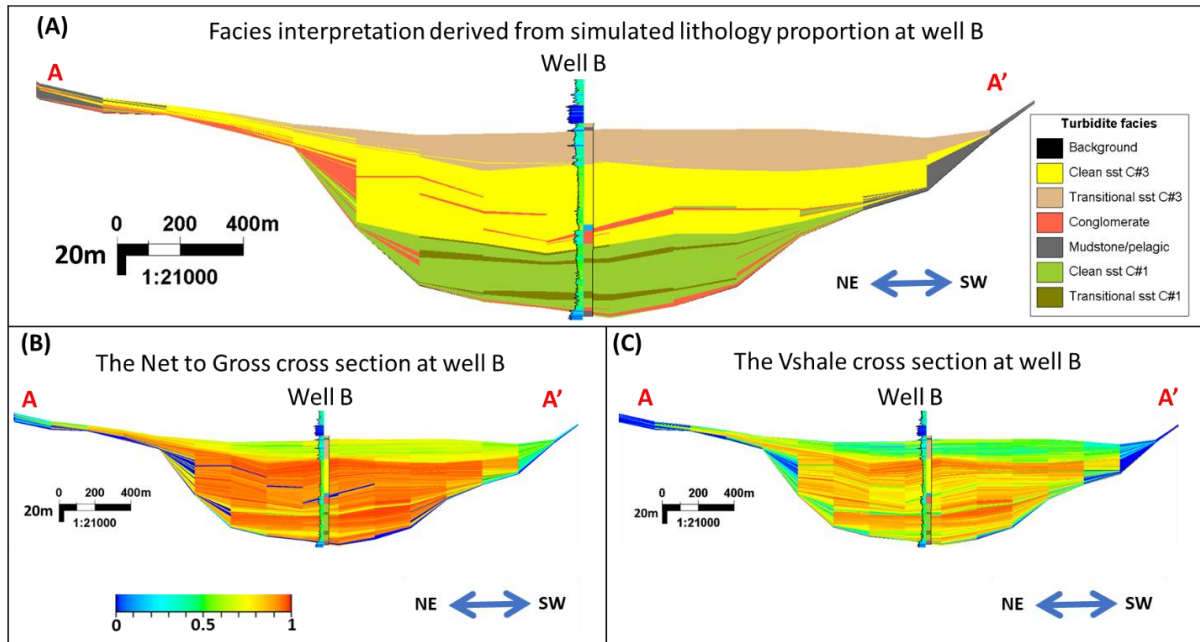


**Figure 39.** 3D view of lithology distribution of case 3: (A) the top of lower reservoir, (B) the top of upper reservoir

## 7.2 Reservoir properties

### 7.2.1 Sections at well B and along the basin axis

#### a. Case 1

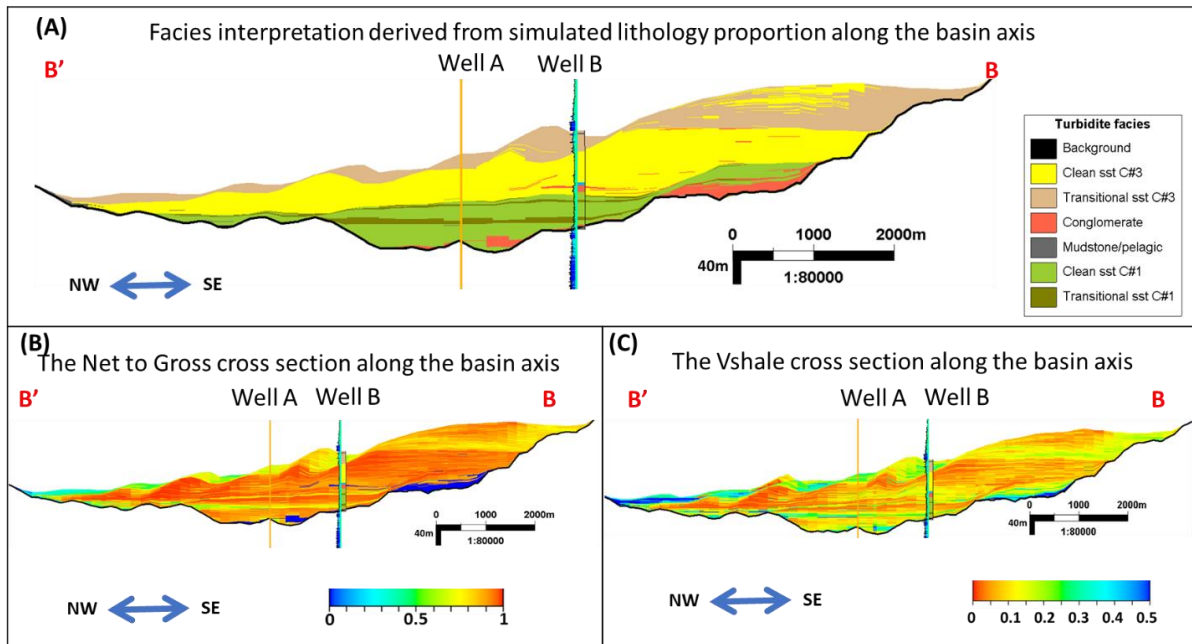


**Figure 40.** The cross section at well B (A-A') showing the result of case 1: (A) the facies, (B) the Net-to-Gross, (C) the Vshale properties

To differentiate the facies coming of canyons 1 and 3, different color codes were assigned for the clean sandstones and transitional sandstones for each of the canyons. In case 1, the clean sandstone of canyon 1 was set to be light green and the transitional sandstone from canyon 1 was set as dark green. On the other hand, the clean sandstone from canyon 3 was assigned as yellow, while the transitional sandstone from canyon 3 was light brown.

The cross section A-A' at the position of well B (Figure 40A) shows that the facies interpretation from the model fits the facies log (conglomerate intervals, transitional sandstones and clean sandstones from the two canyons). The number of conglomerates distributed quite sporadically, is compatible with the facies log, and accumulated at the bottom of the two edges of the reservoir. Pelagic shale also appears in thin layers at the flanks as a result of diffusion from slope sediments.

This distribution leads to a similar trend in Net-to-Gross (Figure 40B) and Vshale (Figure 40C) properties. The reservoir has high Net-to-Gross (around 1) and low Vshale (around 0) in the coarse sand units. In the transitional sandstone units, the reservoir has a Net-to-Gross of approximately 0.7, while the Vshale is about 0.3. In the conglomerate or pelagic shale intervals, the Net-to-Gross equals 0 and the Vshale is higher than 0.5.



**Figure 41.** The section along the basin axis (B-B') showing the result of case 1: (A) the facies, (B) the Net-to-Gross, (C) the Vshale properties

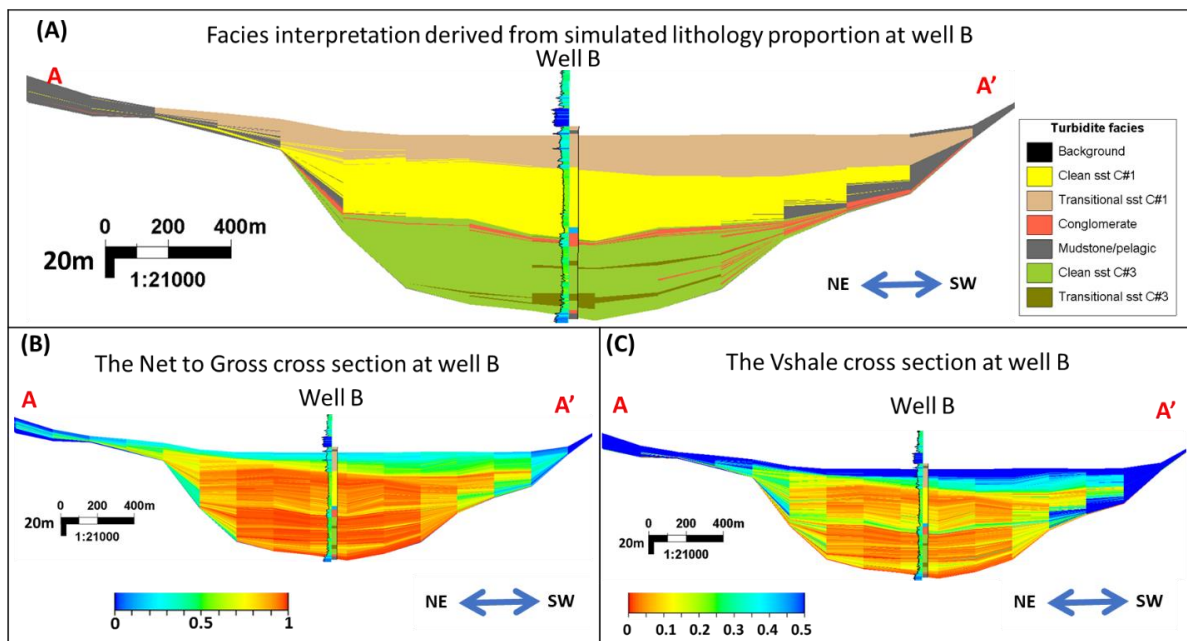
Figure 41A shows a clear division between sediments from canyon 1 and canyon 3 along the axis of the basin. The conglomerates are distributed quite discontinuously, mainly at the bottom of the reservoir, and gradually getting thinner away from the sources. In the upper reservoir, transitional sandstone overlaps the coarse sandstone, marking the regressive trend. However, in areas near the source, coarse sands still share a relatively large amount.

Figure 41B shows that the Net-to-Gross of the whole reservoir is quite high, about 0.8-1 in most of the reservoir, except in two thin layers of transitional sandstones in the lower reservoir and the transitional sandstones in the upper reservoir (NtG around 0.6-0.7). The presence of the coarse sand in the area near the source of the upper reservoir increased the NtG value of this area to 0.8-1.

Figure 41C displays a similar trend in  $V_{shale}$ . In the coarse sand units,  $V_{shale}$  is close to 0. This property increases to 0.3 in the conglomerates and transitional sandstone intervals, and above 0.5 in the distal part of the upper reservoir.

b. Case 2

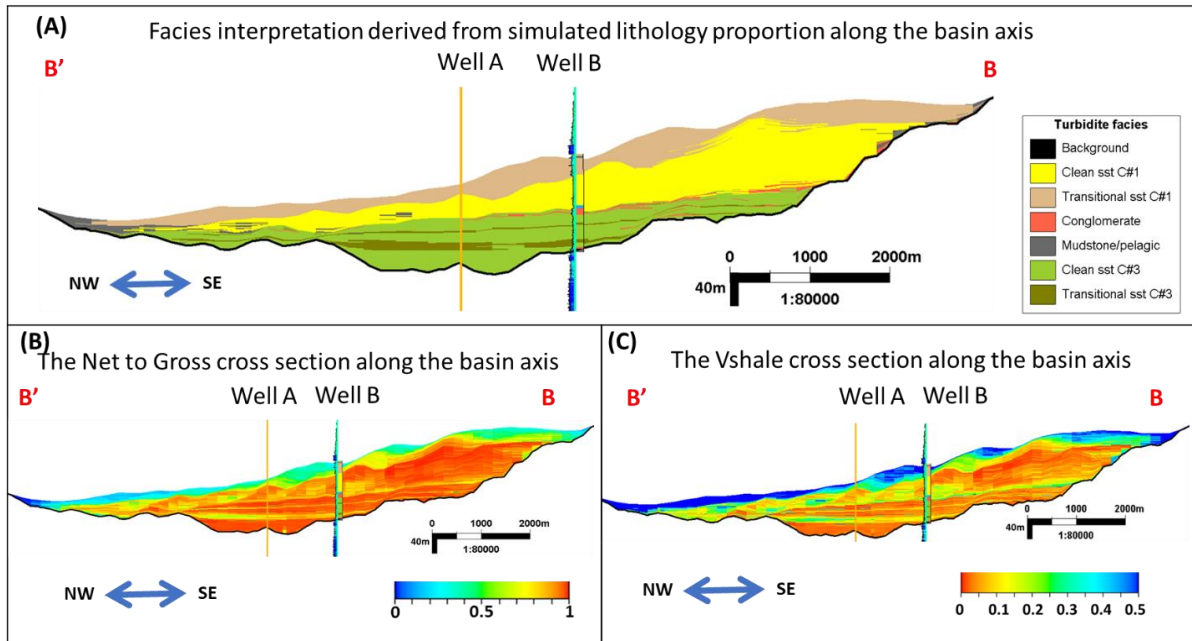
Since the active time of canyons 1 and 3 were switched in case 2 (canyon 3 started first and canyon 1 later), their color code for coarse sands and transitional sandstones were also switched, in order to better compare the final outcome with the facies log.



**Figure 42.** The cross section at well B (A-A') showing the result of case 2: (A) the facies, (B) the Net-to-Gross, (C) the  $V_{shale}$  properties

Figure 42A shows that the facies properties of case 2 also fits the facies log at well B. There is a clear boundary between the sediments from the two different origins. However, there is a slight difference between case 2 and case 1. In case 2, the number of conglomerates at the base of the top reservoir tends to be more continuous and formed a thin layer separating the two reservoirs. The fraction of conglomerate at the base is so small that it cannot be displayed in the cross section. Furthermore, the amount of pelagic shale on both sides of the basin is higher in case 2. It leads to high  $V_{shale}$  values at the flank in the SW and the top of the model (higher than 0.5) (figure 42C) and lower Net-to-Gross in these areas (around 0.2) (Figure 42B).

In Figure 43A, there is an obvious distinction between the sediments from canyon 1 and from canyon 3 along the basin axis. In case 2, the conglomerates in the lower reservoir are much less than in case 1 (Figure 41A). Additionally, in the proximal area of the upper reservoir, there is more homogeneous transitional sandstones compared with the distribution in case 1.



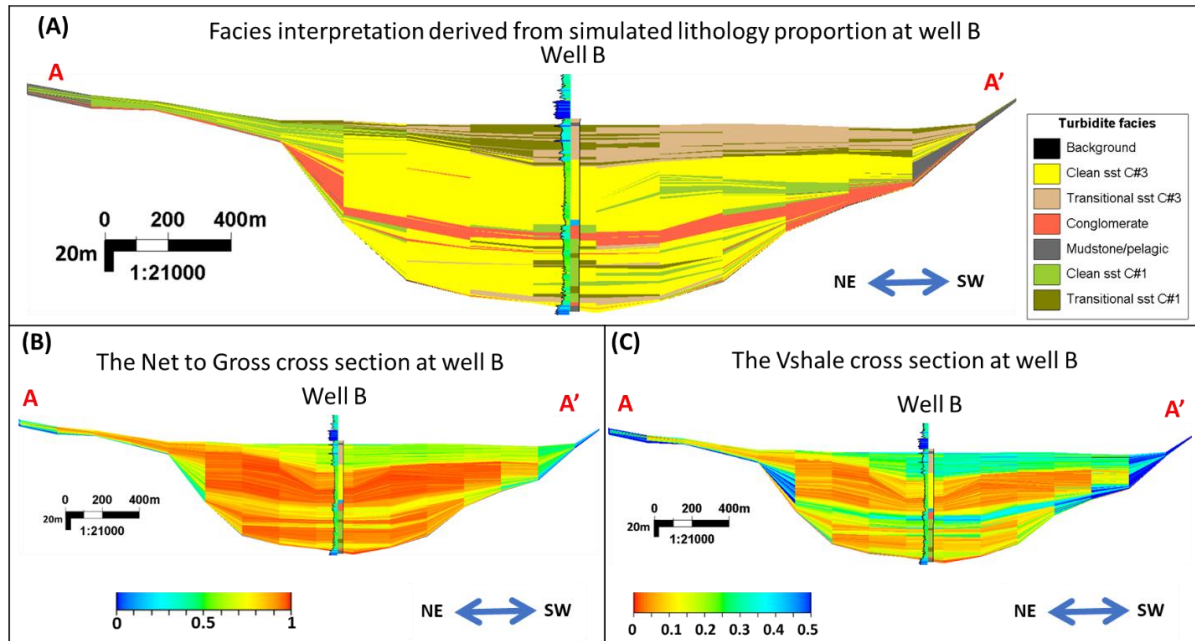
**Figure 43.** The section along the basin axis (B-B') showing the result of case 2: (A) the facies, (B) the Net-to-Gross, (C) the Vshale properties

As a result, the Net-to-Gross attribute has high value for the lower reservoir and the coarse sand in the upper reservoir (Figure 43B). In the top of the upper reservoir, the Net-to-Gross is lower (around 0.5) and more consistent in comparison to case 1 (Figure 41B). This is because the shale volume of this interval in case 2 (Figure 43C) is higher than the shale volume in case 1 (Figure 41C).

### c. Case 3

In case 3, considering the location of the conglomerates, the clean sandstones and the transitional sandstone interval, the cross-section at well B shows compatibility between the model and the well facies log. However, there is no boundary separating the sediments of the two different sources, as the clean sandstones from canyon 1 and canyon 3 were mixed in both, the lower and upper reservoir (Figure 44A). A similar phenomenon happened at the top of the upper reservoir, where the transitional sandstones from the two canyons interbedded with each

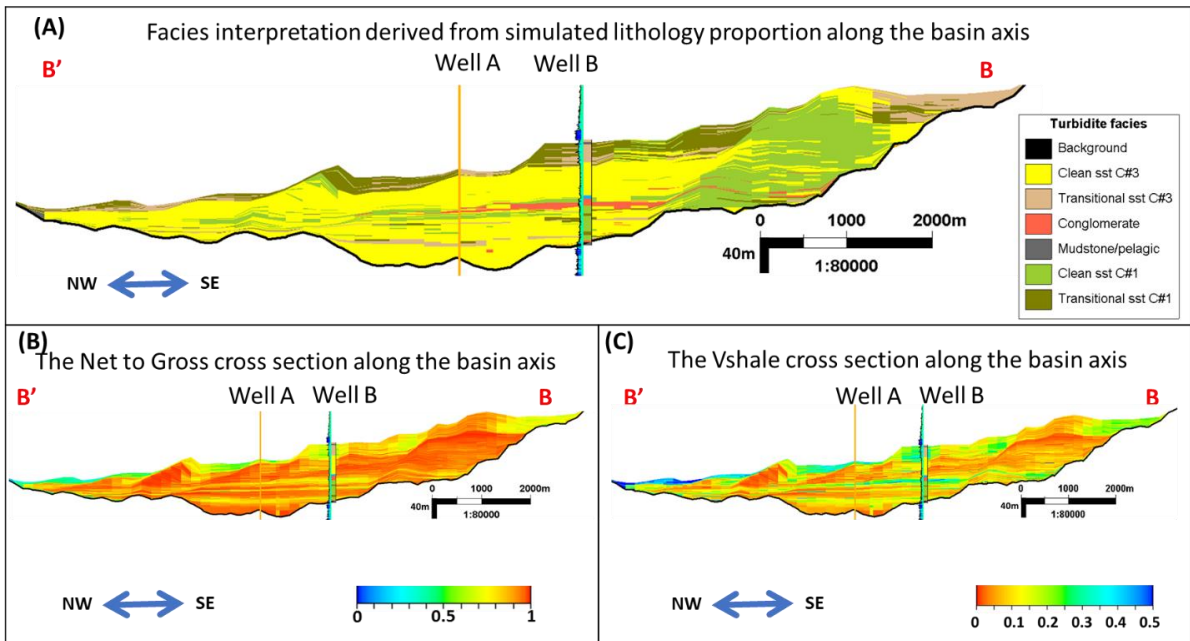
other. The conglomerates form a thick, continuous unit, isolating the lower reservoir from the upper reservoir (Figure 44A).



**Figure 44.** The cross section at well B (A-A') showing the result of case 3: (A) the facies, (B) the Net-to-Gross, (C) the Vshale properties

Figure 45A shows that the clean sands from canyon 3 dominate the lower part of the reservoir. Most clean sands from canyon 1 are limited to the proximal area, and only a small amount of them reaches well B and A. In the transitional sandstone intervals, there is a balanced mixture between the transitional sandstones from canyon 1 and canyon 3. The conglomerate layers are quite thick at well B, and getting thinner distally and disappear after well A.

Although there is blending of sediments from the two canyons, the Net-to-Gross (Figure 45B) and Vshale (Figure 45C) properties show a similar trend as in cases 1 and 2. In the lower reservoir and clean sandstone intervals, the Net-to-Gross is high (around 0.8 to 1) with low Vshale values (around 0 to 0.1). There is a transgression trend at the top of the upper reservoir, where the Vshale increases and Net-to-Gross decreases upward. The shale volume also increases from proximal to distal areas.



**Figure 45.** The section along the basin axis (B-B') showing the result of case 3: (A) the facies, (B) the Net-to-Gross, (C) the Vshale properties

## 7.2.2 Quantitative comparison between the model and well data

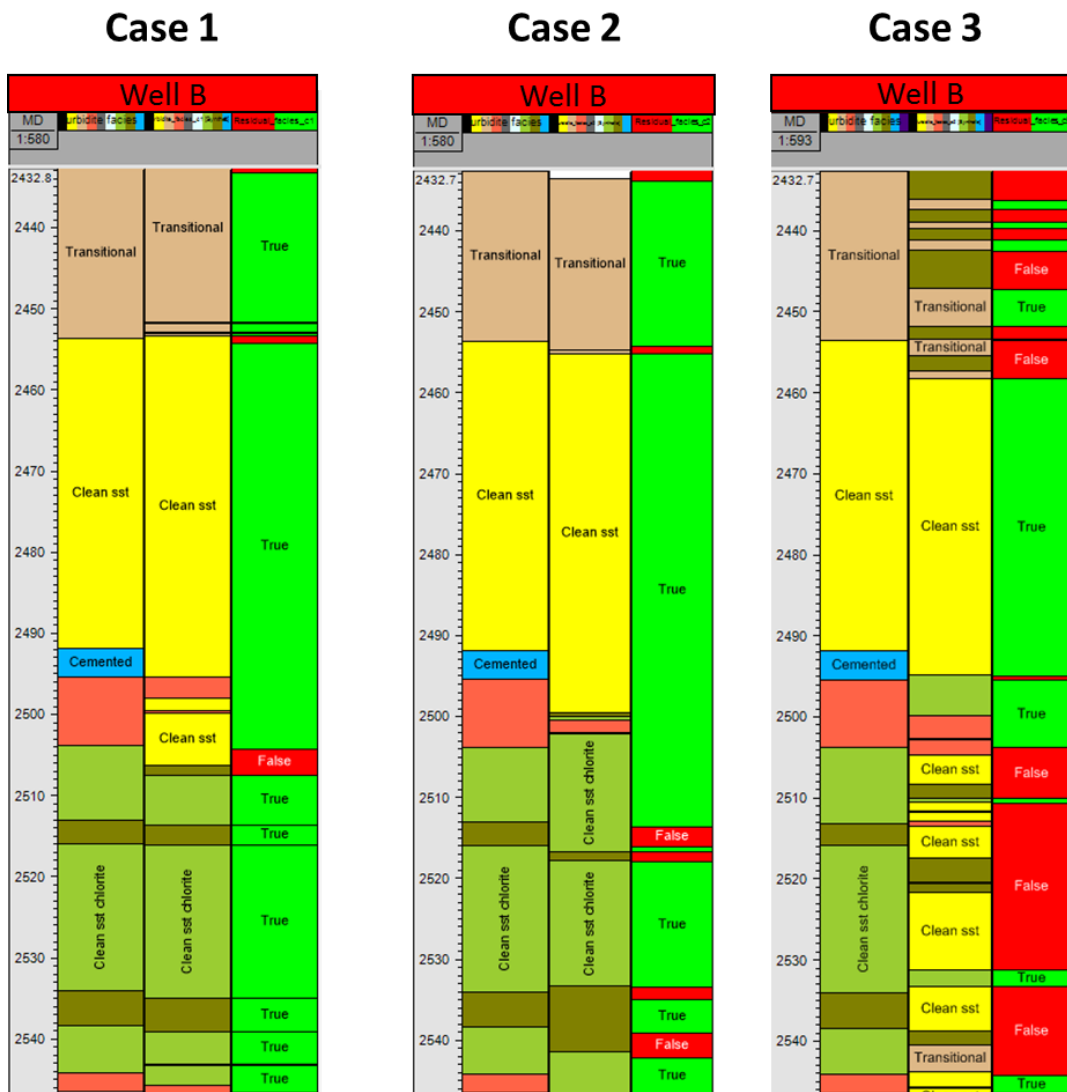
### a. Facies

Following the methodology mentioned in section 6.4.2, three curves including the actual facies log (left), the facies log converted from the model (middle), and the Boolean log (right) were displayed together to show the matching level of the facies model and the facies log at well B for all cases (Figure 46). The green intervals in the Boolean log illustrate the matching, while the red intervals represent mismatches

The quantitative comparison results were calculated based on the Boolean log and they are summarized in Table 17.

**Table 17.** Matching level of facies models to the actual facies log in the three modelled cases

	Case 1	Case 2	Case 3
Facies matching (%)	93.5	88.1	50.1



**Figure 46.** Three curves including the actual facies log (left), the facies log converted from the model (middle), and Boolean log (right) for each of the three simulated cases.

b. Vshale

Following the methodology mentioned in section 6.4.2, three curves including the actual Vshale log (left), the Vshale log converted from the model (middle), and the Boolean log (right) are displayed together to show the matching level of the facies model and the facies log at well B for each of the three modelled cases (Figure 47). The green intervals in the Boolean log illustrate the matching, while the red intervals represent mismatches.



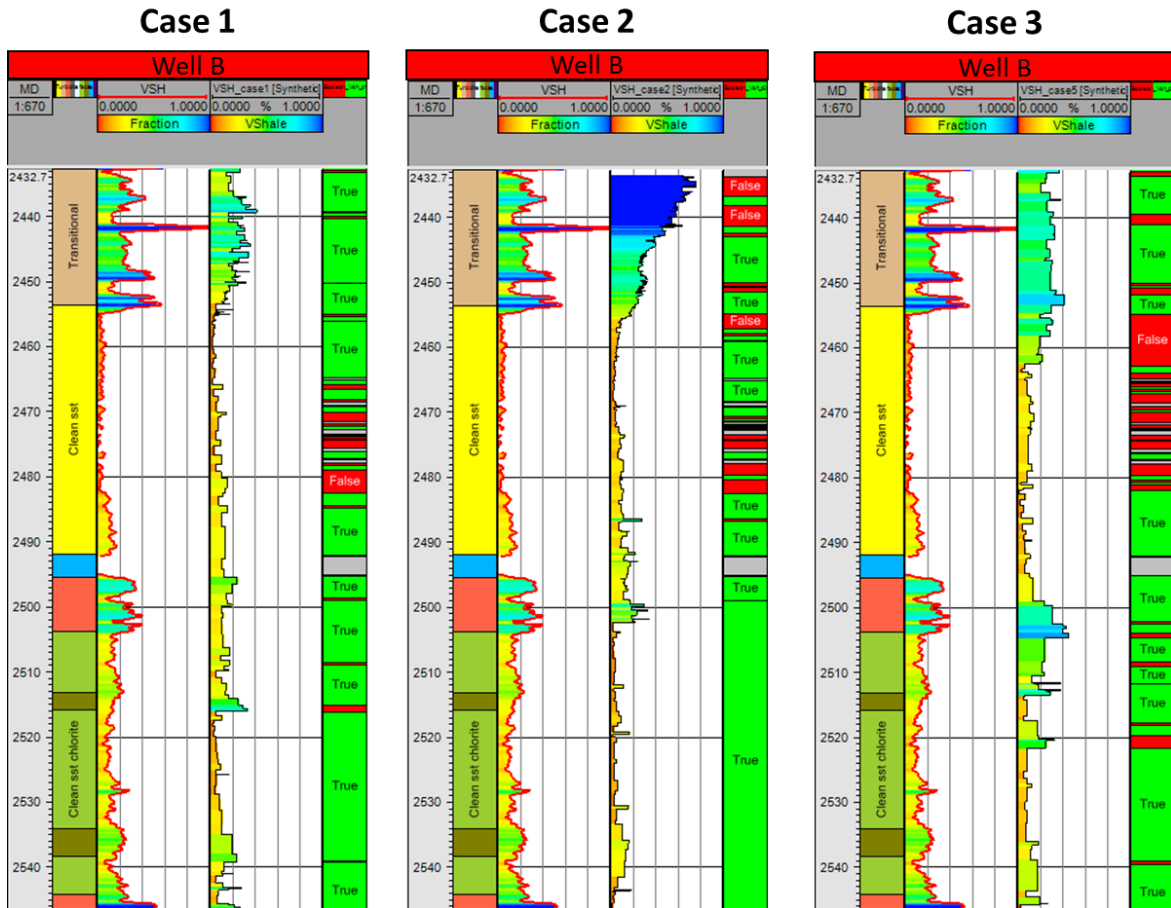


Figure 47. Three curves including the actual Vshale log (left), the Vshale log converted from the model (middle), and the Boolean log (right) for each of the three simulated cases

The quantitative comparison results were calculated based on the Boolean log and they are summarized in Table 18.

Table 18. Matching level of Vshale properties and well log in three cases

	Case 1	Case 2	Case 3
Vshale matching (%)	86.3	83.2	74.3

For the discussion, the best case was selected using qualitative and quantitative criteria. Table 19 summarizes the key qualitative criteria for the three cases.

**Table 19.** Summary of qualitative criteria to choose the best case for investigating the canyons' interaction

Criteria	Case 1	Case 2	Case 3
Conglomerate layers lied within conglomerate interval in the facies log	Match	Match	Match
Transgression trend in the upper reservoir, results in transitional sandstones	Match	Match	Match
Transitional sandstones intervals fit with facies log in the lower and upper reservoir	Match	Match	Unmatched
Clear boundary between sediments from 2 origins at well B	Match	Match	Unmatched
The reservoir extension is constrained by polygon observed from seismic data	Match	Match	Unmatched
The Net-to-Gross value is 1 for clean sandstones, and 0.7-0.8 for transitional sandstones	Match	Unmatched	Match
The conglomerates scattered in the upper reservoir	Match	Match	Unmatched

Combining the table 19 with the quantitative comparisons (tables 17 and 18) proves that case 1 is the best fit with the data as well as the conceptual model. Therefore, case 1 was chosen as the best scenario for further discussion.

## 8. Discussion

The results from all cases validated the geological context mentioned in the conceptual model. The sediment transported through two canyons from the south and southeast area was able to reach the well locations, as well as accumulate sufficient thickness. The simulation results also provided more constraints for the base map. The lithological distribution at well B and the spectral decomposition time slices show that the deposition space of the reservoir was confined. However, based on the tests, a similar accommodation space could not be produced by GPM from the original paleo-bathymetry map by erosion of the turbidities.

Therefore, the original base map was adjusted. There are many different possible levels of confinement, but the two selected maps show a great influence of the topography on the turbidite geometry even though they show only small differences. Finally, the more confined base map delivered a turbidite outline similar to the observation from the well and seismic data.

### **8.1 System evolution**

The outcome of case 1 confirms that if canyons 1 and 3 (Figure 20) are linked to two different sources, they must have been active at different times in order to provide a clear distinction of the lithology between the lower and upper reservoir at well B. Considering this scenario, canyon 1 started first and filled the lower reservoir. The active sources shifted from canyon 1 to canyon 3, where the later filled the upper reservoir. There was a short and gradual transition period between the two canyons corresponding to the conglomerate interval in well B. The conglomerates only emerged within the canyons, and have different origins to the reservoir coarse sands and silts.

The thick sandstones intervals in both reservoir units are the result of several stacks of turbidity events. The quiet period between two events must had been very short compared to the time of the whole system, because there is no pelagic shale lamination detected among the blocky sandstones. Both lower and upper reservoirs follow a similar fining upward stacking pattern, starting with the conglomerates at the base, to a clean sandstone in the middle and a transitional sandstone layer at the top. Since the turbidite system was formed at a large water depth (about 1500 m TVDSS) during constant sea level (Albian stage) (figure 5), the occurrence of the transitional sandstones is the direct result of the weakening turbidity flow processes. The role of sea level in triggering the source is small.

### **8.2 Geometry distribution**

Figure 48A shows the distribution of the thickness of the lower reservoir as the result of case 1. Well A and B are located at the channel axis, where the thickness is maximum (around 45 – 55 m). The width of the lower reservoir increases from 1000 m at the canyon feet, to 1500 m at well B, and 2000 m at well A. However, the lower reservoir becomes thinner in the NW direction, and its limit matches the boundary polygon interpreted from seismic (light green line in Figure 48).

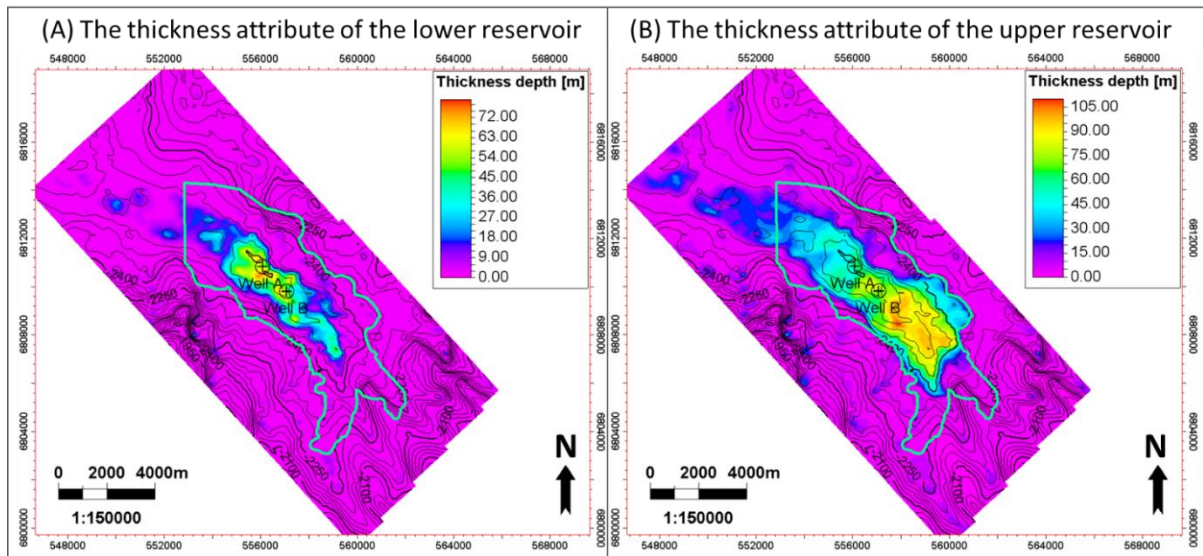
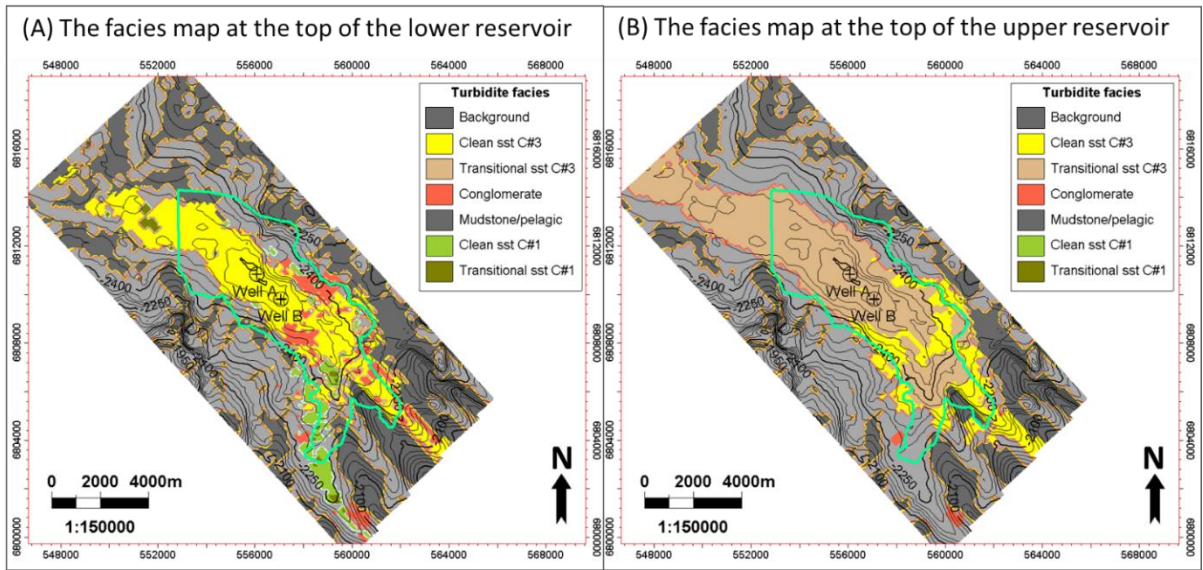


Figure 48. The thickness attribute of the reservoir units of case 1: (A) the thickness of the lower reservoir, (B) the thickness of the upper reservoir. The green polygon represents the reservoir boundary derived from seismic

Figure 48B shows the extension of the upper reservoir. In the proximal area, the upper reservoir has thick accumulation, around 90 – 100m, and is well constrained within the boundary polygon. This reservoir unit also has a large width (4000m) in the area at the canyon feet. The upper reservoir becomes thinner and narrower to the NW. Its thickness reduces to 30 – 45m in the distal part and shows a width of almost 3000m. The most distal part is outside of the seismically derived boundary, however its thickness is less than 20m, which is at the edge of seismic resolution.

Figure 49 shows the facies map at two reservoir levels of case 1. At the top of the lower reservoir, the turbidity flows from canyon 3 blocked the turbidites from canyon 1. This is indicated by the domination of the clean sands coming from canyon 3 (yellow) over the clean sands from canyon 1 (green). The conglomerates originated from the canyons and scattered laterally within the transitional interval (Figure 49A). In the top of the upper reservoir, the transitional sands occupied a large part of the reservoir, with the exception of the proximal and canyon areas.

The discrepancy between the simulation results and the outline of the present day reservoir from the seismic interpretation could be attributed to (1) uncertainty on the topography (Top Åsgard Palaeobathymetry) and (2) uncertainty on seismic picking (seismic resolution).

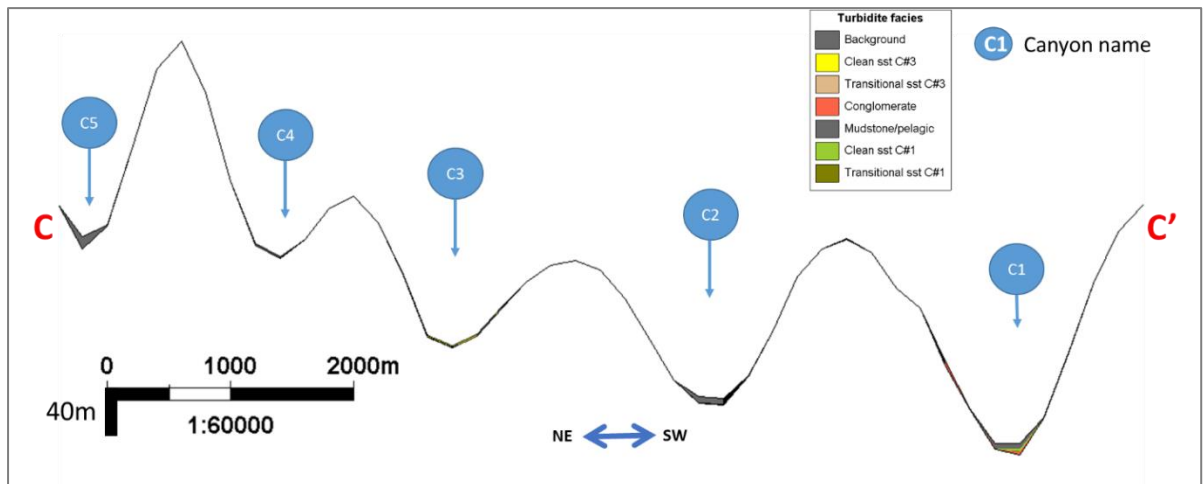


**Figure 49.** The facies map at different reservoir intervals: (A) the facies map at the top of the lower reservoir; (B) the facies map at the top of the upper reservoir. The green polygon represent the reservoir boundary derived from seismic

### 8.3 Reservoir architecture

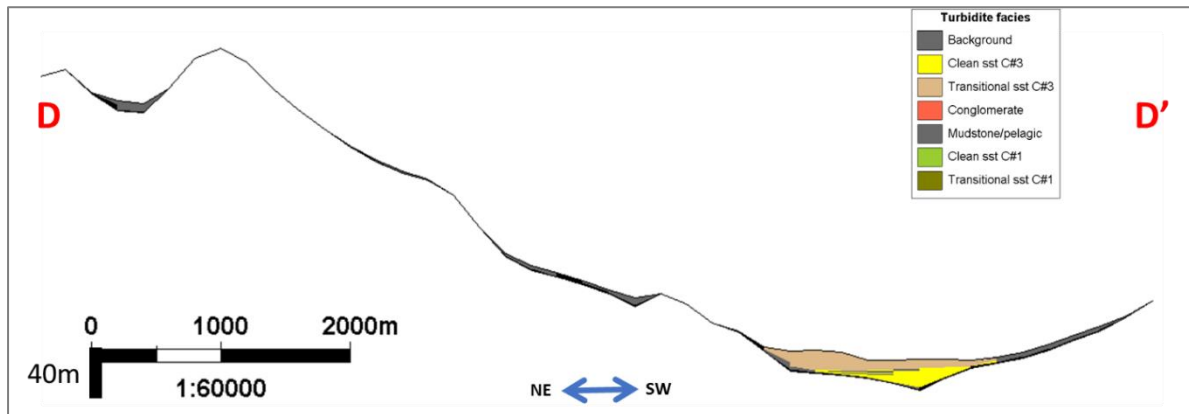
Four cross sections: C-C', D-D', E-E', and F-F' (figure 27) are used to illustrate lithology distribution resulting from case 1 at the edges of the reservoir.

The cross section C-C' along the canyon feet (Figure 50) shows that the reservoir pinches out in this area. Canyon 2, 4, 5 are totally filled by the pelagic shale. In canyon 1, a pelagic shale layer overlays a thin clean sand and conglomerate layer. In canyon 3, clean sand layers are too thin to be observed in the cross section.



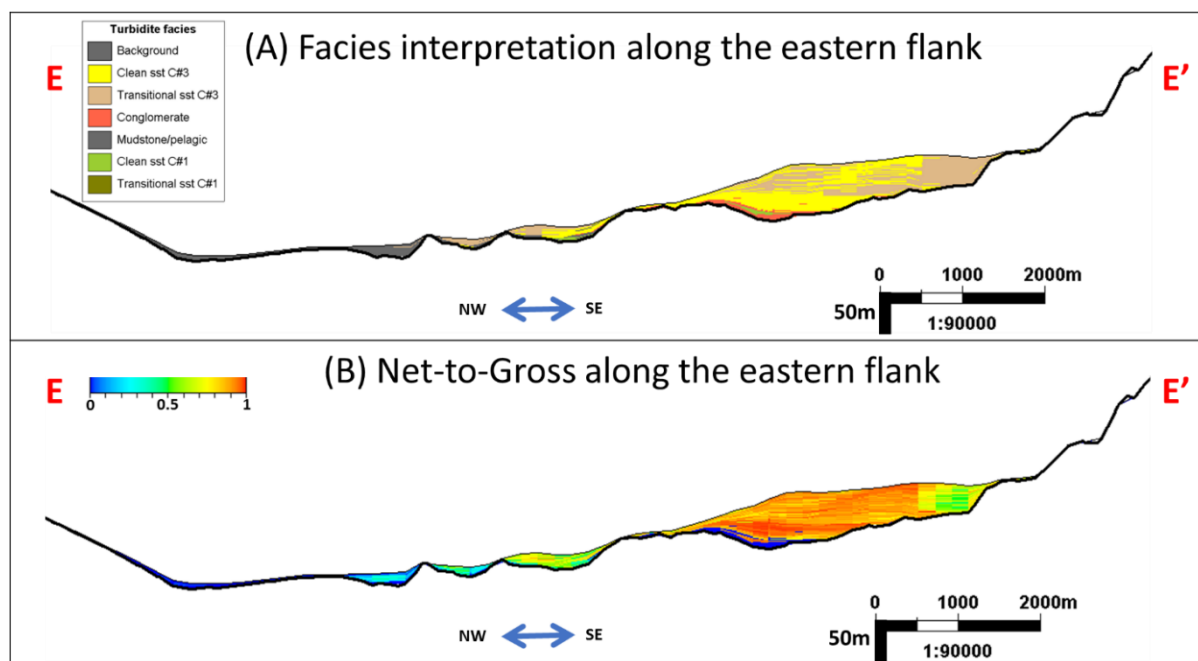
**Figure 50.** Cross section C-C' at the canyon feet of case 1. Navigation of cross section C-C' displayed in figure 27.

In the section at the most distal area (D-D'), the reservoir is flattened out, with a total thickness of around 20m, and a width of ca 2km. The transitional sandstones dominate a large part of this area, due to the decreased amount of clean sand and increased silt fraction (Figure 51).



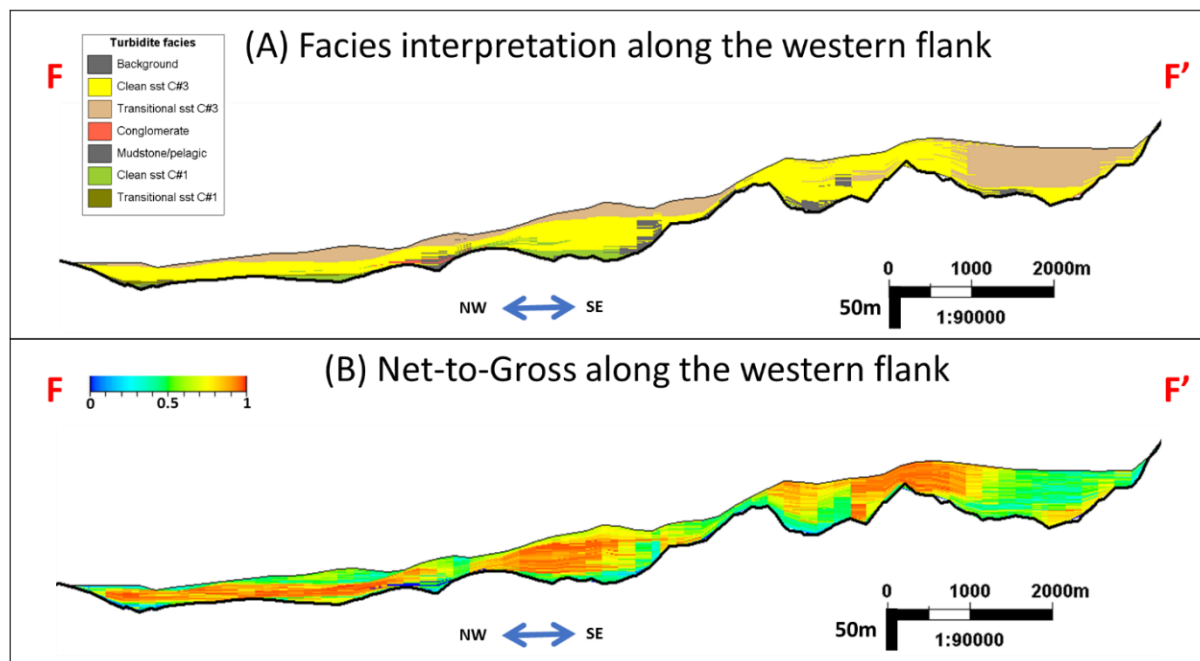
**Figure 51.** Cross section D-D' thru the most distal area of the reservoir of case 1. Navigation of cross section D-D' displayed in figure 27.

In the section along the eastern flank (E-E') (Figure 52), the reservoir becomes thinner and more shaly distally. The clean sand layers are laminated with the transitional sands in the proximal area. The conglomerates deposited in small layers at the bottom of the model (Figure 52A). The Net-to-Gross is generally high in the proximal part (around 0.9 – 1), except in the area closest to the canyon where silt dominates (Figure 52B).



**Figure 52.** Section E-E' along the eastern flank with reservoir properties: (A) the facies property; (B) the Net-to-Gross property. Navigation of cross section E-E' displayed in figure 27.

In the section along the western flank (F-F') (Figure 53), the reservoir becomes thinner distally. The clean sand layers extend from the proximal to the distal part. The transitional sand layers overlap the clean sand layers. The transitional sand dominates in the area closest to the canyon foot. The conglomerates can be seen in small cells in the distal part. There are a few pelagic shale cells scattering within the clean sand, which could be the result of diffusion (Figure 53A). The Net-to-Gross is high in the clean sand layers (around 0.9 – 1), and low in the transitional sand layers (0.5 – 0.6) (Figure 53B).



**Figure 53.** Section F-F' along the western flank with reservoir properties: (A) the facies property; (B) the Net-to-Gross property. Navigation of cross section F-F' displayed in figure 27.

## 9. Conclusion

With the mechanism based on the laws of physics, stratigraphic forward modelling techniques such as GPM have the big advantage of predictive power, which cannot be offered by classic modelling techniques such as Object Modelling, Sequential Indicator Simulation or Multiple Point Statistics.

This thesis has established a workflow applying GPM technology to check the physical consistency of the conceptual models. Its result helps selecting the most likely geological concept and increasing significantly the confidence in the initial interpretation. Moreover, the thesis developed a new quantitative approach to calibrate the modelling output with the hard

data (well logs and seismic interpretation). The final model is a valuable source of information predicting a realistic architecture, geometry and connectivity of the reservoir.

Additionally, the master thesis addresses some limitations of the GPM techniques. Since this approach is simulating geological processes as a function of time, the CPU and model size can increase significantly. Therefore, GPM requires a powerful machine configuration to perform optimally. Other parameters that have a major impact on the CPU are the modelling area and its resolution. Consequently, in order to address hardware limitations compromises need to be made in terms of grid resolution and simulation time.

A major challenge of GPM remains the handling of uncertainty. This thesis shows a good example of GPM's sensitivity with respect to the basement topography. Besides, the confirmation of a conceptual model does not mean that this model is correct. Other scenarios based on different parameters could honor the hard data in a similar good way. The different cases are not necessarily easy to define and to validate against the hard data.

Furthermore, although the facies, Net-to-Gross and Vshale properties generated from the modelling output help to understand the reservoir characteristics, they are created from fixed cutoff values that probably are subject to uncertainty. In fact, only general ideas exist about the values of most of the geological parameters, which are based on recent analogue data. This uncertainty is partly controlled by the matching of the GPM output with the measured data. However, lack of hard data does result in uncertainty of the model that should be addressed thru setting up alternative cases.

In summary, this thesis confirms the superiority of stratigraphic forward modeling techniques to the classic approaches. The workflow and parameter setting developed in the thesis can be applied easily to other cases of similar geological scenario to deliver highly accurate reservoir model..



# Appendix

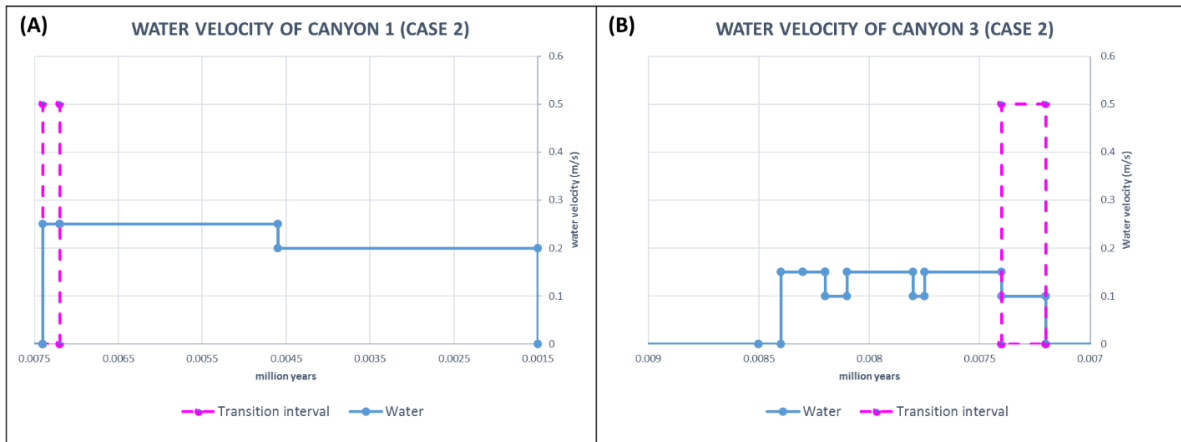


Figure 54. The variation of water velocity at canyon 1 (A) and canyon 3 (B) (Case 2).

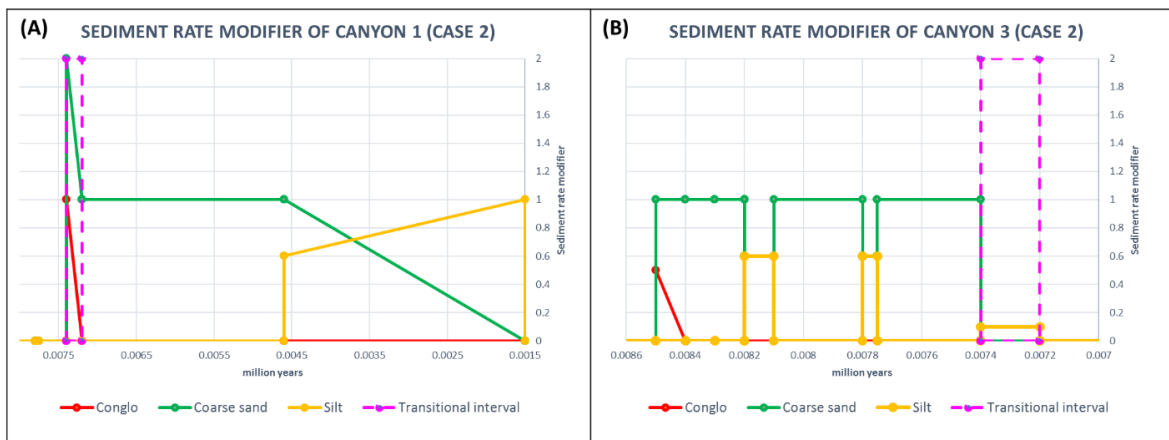
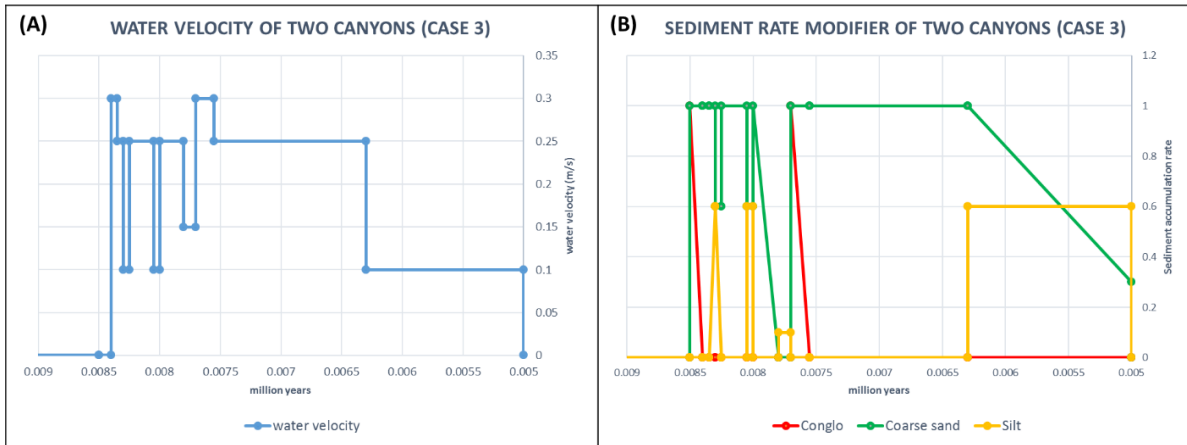


Figure 55. The variation of sediment rate modifier at canyon 1 (A) and canyon 3 (B) (Case 2).



**Figure 56.** The variation of water velocity and sediment rate modifier at two canyons (Case 3).

## Reference

- BUGGE, T., TVEITEN, B. & BÄCKSTRÖM, S. 2001. The depositional history of the Cretaceous in the northeastern North Sea. *Norwegian Petroleum Society Special Publications*. Elsevier.
- BURGESS, P. M. 2012. *A brief review of developments in stratigraphic forward modelling, 2000–2009-14*, Elsevier B.V.
- CLERC, S., DU FORNEL, E. & LAGEAT, G. 2018. PL636 Sedimentological review report – wells 36/7-4 and 35/9-3 ST2. *Neptune Energy Internal Report*.
- DOTT, R. H. J. 1963. Dynamics of subaqueous gravity depositional processes. Tulsa, Okla. .:
- GLENNIE, K. W. 2009. *Petroleum Geology of the North Sea: Basic Concepts and Recent Advances*, Oxford, UK, Oxford, UK: Blackwell Science Ltd.
- HAQ, B. U. 2014. Cretaceous eustasy revisited. *Global and Planetary Change*, 113, 44-58.
- HAUGHTON, P., DAVIS, C., MCCAFFREY, W. & BARKER, S. 2009. Hybrid sediment gravity flow deposits – Classification, origin and significance. Guildford.
- HAUGHTON, P. D. W., BARKER, S. P. & MCCAFFREY, W. D. 2003. ‘Linked’ debrites in sand-rich turbidite systems - origin and significance. Oxford.
- ISAKSEN, D. & TONSTAD, K. 1989. *A revised Cretaceous and Tertiary lithostratigraphic nomenclature for the Norwegian North Sea*, Norwegian Petroleum Directorate.
- JACKSON, C. A. L., BARBER, G. P. & MARTINSEN, O. J. 2008. Submarine slope morphology as a control on the development of sand-rich turbidite depositional systems: 3D seismic analysis of the Kyrre Fm (Upper Cretaceous), Måløy Slope, offshore Norway. Guildford.
- KUENEN, P. H. 1966. Matrix of turbidites: experimental approach. *Sedimentology*, 7, 267-297.
- LAI, S. Y. J., GERBER, T. P. & AMBLAS, D. 2016. An experimental approach to submarine canyon evolution. Washington, D.C. .:

- LOWE, D. R. 1979. Sediment gravity flows: their classification and some problems of application to natural flows and deposits.
- LOWE, D. R. 1982. Sediment gravity flows; II, Depositional models with special reference to the deposits of high-density turbidity currents. *Journal of sedimentary research*, 52, 279-297.
- MIDDLETON, G. V. 1967. Experiments on density and turbidity currents: III. Deposition of sediment. *Canadian Journal of Earth Sciences*, 4, 475-505.
- MIDDLETON, G. V. 1993. Sediment deposition from turbidity currents. *Annual review of earth and planetary sciences*, 21, 89-114.
- MIDDLETON, G. V. & HAMPTON, M. A. 1973. Part I. Sediment gravity flows: mechanics of flow and deposition.
- NARDIN, T. R., HEIN, F., GORSLINE, D. S. & EDWARDS, B. 1979. A review of mass movement processes sediment and acoustic characteristics, and contrasts in slope and base-of-slope systems versus canyon-fan-basin floor systems.
- NOTTVEDT, A., GABRIELSEN, R. H. & STEEL, R. J. 1995. Tectonostratigraphy and sedimentary architecture of rift basins, with reference to the northern North Sea. *Marine and Petroleum Geology*, 12, 881-901.
- PAOLA, C. 2000. Quantitative models of sedimentary basin filling. *Sedimentology*, 47, 121-178.
- PICKERING, K. T., HISCOTT, R. N. & HEIN, F. J. 1989. *Deep-marine environments: clastic sedimentation and tectonics*, Allen & Unwin Australia.
- POSTMA, G., NEMEC, W. & KLEINSPEHN, K. L. 1988. Large floating clasts in turbidites: a mechanism for their emplacement. *Sedimentary geology*, 58, 47-61.
- REEVE, M. T., BELL, R. E., DUFFY, O. B., JACKSON, C. A. L. & SANSOM, E. 2015. The growth of non-colinear normal fault systems; What can we learn from 3D seismic reflection data? *Journal of Structural Geology*, 70, 141-155.
- ROBERTS, A. M., KUSZNIR, N. J., YIELDING, G. & BEELEY, H. 2019. Mapping the bathymetric evolution of the Northern North Sea: from Jurassic synrift archipelago through Cretaceous–Tertiary post-rift subsidence. Bath, UK .:

- SHANMUGAM, G. 1996. High-density turbidity currents; are they sandy debris flows? *Journal of Sedimentary Research*, 66, 2-10.
- SHANMUGAM, G. 2000. 50 years of the turbidite paradigm (1950s—1990s): deep-water processes and facies models—a critical perspective. Guildford.
- SHANMUGAM, G. 2018. Slides, Slumps, Debris Flows, Turbidity Currents, and Bottom Currents: Implications. *Earth Systems and Environmental Sciences, Elsevier Online Module*.
- SHIELDS, A. 1936. Anwendung der Aehnlichkeitsmechanik und der Turbulenzforschung auf die Geschiebebewegung. *PhD Thesis Technical University Berlin*.
- TALLING, P. J. 2013. Hybrid submarine flows comprising turbidity current and cohesive debris flow: Deposits, theoretical and experimental analyses, and generalized models. Boulder, Colo. :.
- TETZLAFF, D. & PRIDY, G. 2001. Sedimentary process modeling: from academia to industry. *Geologic modeling and simulation*. Springer.
- TETZLAFF, D. M. & HARBAUGH, J. W. 1989. Simulating clastic sedimentation.
- TETZLAFF, D. M., SCHAFMEISTER, M.-T., HARFF, J., HAY, W. & TETZLAFF, D. M. 2007. Interaction among sedimentation, compaction, and groundwater flow in coastal settings. Boulder, CO: Boulder, CO, United States: Geological Society of America (GSA).
- VAN BUCHEM, F. S. P., SMIT, F. W. H., BUIJS, G. J. A., TRUDGILL, B., LARSEN, P. H., BOWMAN, M. & LEVELL, B. 2018. Tectonostratigraphic framework and depositional history of the Cretaceous-Danian succession of the Danish Central Graben (North Sea); new light on a mature area. London: London, United Kingdom: Geological Society of London.
- ZANELLA, E. & COWARD, M. P. 2003. Structural framework. *Millennium Atlas: Petroleum Geology of the Central and Northern North Sea*. Geological Society of London.